

UC Berkeley
SEMM Reports Series

Title

Microstructure of Concrete and Its Influence on the Mechanical Properties

Permalink

<https://escholarship.org/uc/item/2pr4t946>

Author

Monteiro, Paulo

Publication Date

1985-07-01

802

THESIS NO.
UCB/SESM -85/14

**STRUCTURAL ENGINEERING AND
STRUCTURAL MECHANICS**

**MICROSTRUCTURE OF CONCRETE
AND ITS INFLUENCE ON
THE MECHANICAL PROPERTIES**

by

PAULO J.M. MONTEIRO

JUNE 1985

**DEPARTMENT OF CIVIL ENGINEERING
UNIVERSITY OF CALIFORNIA
BERKELEY, CALIFORNIA**

Table of Contents

Abstract	i
Acknowledgements	ii
Table of Contents	iii
Nomenclature	iv
List of Tables	v
List of Figures	vi
1. Introduction	1
1.1 Summary of the Chapters	1
2. Cement Paste Early Hydration	1
2.1 Brief Review of Hydration	1
2.1.1 Hydration of Calcium Silicates	1
2.1.2 Hydration of Calcium Aluminates	1
2.2 Low-Temperature Scanning Electron Microscope Analysis of the Portland Cement Paste Early Hydration	1
2.2.1 Materials and Methods	1
2.2.2 Results and Discussion	1
2.3 References	1
3. Morphology of the Aggregate-Cement Paste Interface	1
3.1 Introduction	1
3.2 Experimental Methods	1
3.2.1 Materials	1

	2
3.2.2 Specimens and Test Procedure	1
3.2.3 Equipment	1
3.3 The Quartz-Cement Paste Interface	1
3.3.1 Formation of Calcium Hydroxide over the Interface	1
3.3.2 Ettringite Formation on the Interface	1
3.3.3 Effect of Silica Fume on the Transition Zone	1
3.3.4 The Expansive Cement Paste-Quartz Interface	1
3.4 The Carbonate-Cement Paste Interface	1
3.5 The Mortar-Aggregate Interface	1
3.6 References	1
4. Mechanical Properties of the Aggregate-Cement Paste Interface	1
4.1 Introduction	1
4.2 Microhardness Tests on the Interfacial Film	1
4.3 A Note on Elastic Mismatch for Composite Materials	1
4.4 A Analysis of the Aggregate-Cement Paste Bond Using Probabilistic Treatment of Brittle Strength	1
4.4.1 Weibull's Statistical Theory for Brittle Materials	1
4.4.2 Materials	1
4.4.3 Test Methods	1
4.4.4 Test Results	1
4.5 Overall Conclusions	1
4.6 References	1
5. A Generalized Continuum Theory for Concrete	1
5.1 Introduction	1

	3
5.2 Brief Literature Review	1
5.3 Generalized Continuous Media	1
5.4 Continuum Theory for Porous and Granular Media	1
5.4.1 Kinematics	1
5.4.2 Thermodynamic Processes	1
5.5 Continuum Theory for Concrete	1
5.5.1 Laws of Motion and Thermodynamic Processes for Fully Saturated Concrete	1
5.5.2 Constitutive Equations	1
5.5.3 Linear Theory	1
5.6 References	1
6. Steel-Concrete Bond	1
6.1 Introduction	1
6.2 Microstructure Characterization of the Interface	1
6.2.1 Morphology of the Interface	1
6.2.2 XRD Analysis of the Interfacial Zone	1
6.3 Effect of Chloride on the Interface	1
6.3.1 Experimental	1
6.3.2 Results and Discussion	1
6.3.3 Conclusions	1
6.4 Mechanical Behavior of the Concrete-Steel Bond	1
6.4.1 Reinforcing Steel-Concrete Bond Mechanism	1
6.4.2 Test Program	1
6.4.3 Test Procedure	1

6.4.4 Test Results and Analysis	1
6.5 References	1

Nomenclature

a_i : acceleration

B_t : configuration of the distributed body at time t

b_i : body force per unit mass

C_3A : $3CaO \cdot Al_2O_3$

C_4AF : $4CaO \cdot Al_2O_3 \cdot Fe_2O_3$

CH : $Ca(OH)_2$

C_2S : $2CaO \cdot SiO_2$

C_3S : $3CaO \cdot SiO_2$

CSH : calcium silicate hydrate

e : internal energy density per unit mass

F_i : individual failure probability

F_{iA} : deformation gradient

G : failure probability

g' : internal equilibrated force

h_i : equilibrated stress vector

j : rank position

k : ratio of shear moduli between two materials (chapter 4)

k : equilibrated inertia (chapter 5)

L_{ij} : velocity gradient

l : equilibrated force per unit mass

m : Weibull or flaw density parameter

m : parameter equal to $4(1-\nu)$ for plane strain and to $\frac{4}{1+\nu}$ for generalized plane stress

N : number of tests

p' : internal body force

q_k : heat flux

r : internal heat source per unit mass

S : survival probability

t_{ij} : stress tensor

u_i : velocity vector

α : parameter defined by $\frac{\mu'm - m\mu m'}{\mu'm + m\mu m'}$

β : parameter defined by $\frac{\mu'(m-2) - m\mu(m'-2)}{\mu'm + m\mu m'}$

δ_{ij} : Kronecker delta

δ_v : material-independent constant for Vickers-produced radial cracks

γ : distributed mass function

ν : Poisson's Ratio (chapter 4)

ν : Volume Distribution Function

μ : shear modulus

ρ : classical mass density

Θ : temperature

List of Tables

2.1 Chemical Properties of the Cement 1

3.1 Type of Rock Used in the Interface Study 1

3.2 Chemical Properties of the A lite 1

3.3 Particle Size Analysis of the Sand 1

4.1 Properties of the Cement 1

4.2 Summary of the Rock Properties 1

4.3 Summary of the Strength Results 1

6.1 Thickness of the Transition Zone 1

6.2 Orientation of the CH Film 1

6.3 Sieve A nalysis 1

6.4 Concrete M ix D esign (0% Silica Fume) 1

6.5 Concrete M ix D esign (8% Silica Fume) 1

6.6 Concrete M ix D esign (16% Silica Fume) 1

6.7 Concrete Strength 1

6.8 Pull-Out Strength (0% Silica Fume) 1

6.9 Pull-Out Strength (8% Silica Fume) 1

6.10 Pull-Out Strength (16% Silica Fume) 1

List of Figures

1.1 Typical Volumetric Element of Concrete	1
2.1 Diagram of the Bio-Chamber Freeze-Fracture System	1
2.2 Uncoated Sample of Cement Paste Inside the Microscope at 110K	1
2.3 Stereo Pair Showing the Topology of the Cement Paste. Small Rods of Ettringite on the Surface of the Cement Particles can be Seen. Picture Width: 27 microns.	1
2.4 Detail of the Cement Particle Surrounded by Small Rod Crystals, 1-hour hydration. Uncoated Specimen Exhibits Charging. Picture Width: 14 microns.	1
2.5 Useful Fracture of the Cement Paste.	1
2.6 Concentration of Material on the Top of the Fracture Plane.	1
3.1 Calcite Grains (39X, Crossed Nicols)	1
3.2 Clivage Plane in the Calcite Grains (39X, Crossed Nicols)	1
3.3 General View of Limestone (156X, Crossed Nicols)	1
3.4 General View of Chert (39X, Crossed Nicols)	1
3.5 Amorphous Nature of Opal (390X, Crossed Nicols)	1
3.6 Particle Size Distribution of Microsilica by X-Ray Sedimentation	1
3.7 Test Procedure	1
3.8-3.9 Shows the Difference of the Granite Surface Before and After the Polishing Process (down to 0.25 microns). The White Box Zone is Amplified to 5000X.	1
3.10 Shows a Typical Morphology of the Hydration Products over the Aggregate (Dark Zone)	1
3.11 Shows the Interface Morphology on the Cement Paste Side	1
3.12 Shows a Micrograph Amplified 20,000 X of the CSH over the Interfacial Film. The Cement Paste Had 0.35 w/c Ratio and Was Cast Against a Granite. The Specimen was 19-days old When It Was Cast	1
3.13 Hadley's grain	1
3.14 Shows the Interface Morphology over the Aggregate (Quartz) Side. The Specimen was 1-day Old	1
3.15 Measurement of the Peaks Intensity	1
3.16 CH Preferential Orientation over the Transition Zone	1
3.17 Variation of the Ettringite Concentration in the Interfacial Zone; 1 day	1
3.18 Variation of the Ettringite Concentration in the Interfacial Zone; 60 days	1
3.19 Shows the Distribution of Silica Furne Near the Aggregate	1
3.19A Shows the White Box Amplified in 3.19 and the Particles Partially Dissolved Can Be Seen. The Specimen Was 30-Days Old and a Replacement of 16% of Microsilica Was Used	1
3.20 General View of the Transition Zone When Expansive Cement IS Used	1
3.21 Detail of Fig. 3.20	1
3.22 Transition Zone When Portland Cement is Used	1
3.23 Transition Zone When Expansive Cement is Used	1

3.24 CH Crystal on the Transition Zone	1
3.25 General View of the Transition Zone (Cement Paste Side)	1
3.26 Detail of Fig 3.25 Showing Ettringite on Top of the CH Film	1
3.27 General View of the Transition Zone (Aggregate Side)	1
3.28 Detail of Fig. 3.27	1
3.29 Detail of Fig. 3.27	1
3.30 Variation of Calcium Hydroxide Preferential Orientation Index in the Transition Zone when Expansive Cement is Used	1
3.31 Variation of Ettringite Concentration in the Transition Zone When Expansive Cement is Used	1
3.32 Detail of the Marble Crystal Structure	1
3.33 General View of the Transition Zone	1
3.34 Calcite Grain Adhering to the CH Film	1
3.35 Evidence of a Better Bond When Carbonate Rock is Used. The Dark Zone is the CH Film	1
3.36 Removal of the Contact Film During Fracture. The Dark Zone is the CH Film	1
3.37 Etching of the Calcite	1
3.38 Imprint of the Calcite Etching on the CH Film	1
3.39 Detail of Fig. 3.38	1
3.40 XRD Analysis of the Interface	1
3.41 Etching of Calcite Casted Against Alite Paste	1
3.42 General View of the Transition Zone When Alite is Used	1
3.43 Detail of Fig 3.42 Showing the Precipitation of Crystals on the Transition Zone	1
3.44 General View of the Transition Zone	1
3.44a Detail of Fig. 3.44 Showing the Imprint of Calcite Etching	1
3.44b Detail of Fig 3.44 Showing the Reprecipitation of Crystals	1
3.45 General View of the Transition Zone Showing the Reaction in the CH Film. EDAX shows no trace of Al.	1
3.46 EDAX Analysis	1
3.47 XRD Analysis of the Interface When Alite Paste is Cast Against a Marble	1
3.48 Analysis of the Interface	1
3.49 Calcium Hydroxide Film and CSH Formed on the Mortar Side of the Interface. The age of this specimen was 30 days	1
3.50 Formation of Well-Defined Hexagonal Crystal of Calcium Hydroxide on the Interface. Compare this Crystal with the Calcium Hydroxide Film Shown in Fig. 3.49, Where no Distinct Crystal Morphology Can be Seen	1
3.51 Detail of the Hexagonal Crystal of Calcium Hydroxide Shown in Fig. 3.50. The Development of Platelets With a Preferential Plane (00.1) Can be Seen	1
3.52 Sand Particle Surrounded by Calcium Hydroxide Film (Dark Zone) at the Interface. The age of this Specimen Was 30 days	1
3.53 Detail of the outlined Area (Magnified 5 Times) Shown in Fig. 3.52.	

The Sand Grains Creates Surface Effects Similar to Those Produced by Large Aggregate. There is Precipitation of Calcium Hydroxide with a Preferential Orientation around the Sand Grain Surface	1
3.54 Variation of Calcium Hydroxide Preferential Orientation Index (I) in the Transition Zone	1
4.1 Testing Machine Used in Measuring Bond	1
4.2 Effect of Sand Content on the Adhesive Properties of Mortar	1
4.3 Bond Specimen	1
4.4 Effect of Type of Rock on the Bond Strength	1
4.5 Variation in the Micro-hardness Across the Transition Zone	1
4.6 Schematic of Vickers-produced Indentation-Fracture System	1
4.7 Impression of the Vickers Pyramid on the CH Film (30-Days Old Specimen)	1
4.8 Microhardness of the CH Film	1
4.9 Displaced Material Pilling Up on the Corners at Higher Loads	1
4.10 Development of a System of Cracks (1-year old specimen)	1
4.11 Crack Arrested at a Void	1
4.12 Complex System of Cracks	1
4.13 k-polygon	1
4.14 Bond Test	1
4.15 Process of Molding the Bond Specimens	1
4.16 Aggregate-Cement Paste Bond Strength	1
4.17 Plot to Obtain Weibull Parameter	1
4.18 Unloaded Concrete Specimen	1
4.19 Aggregate-Cement Paste Interface	1
4.20 Loaded Concrete Specimen	1
4.21 Fracture Path	1
4.22 Fracture Path	1
6.1 Test Procedure	1
6.2 Calcium Hydroxide Film on the Cement Paste Side (30 days old, 16% silica fume)	1
6.3 Calcium Hydroxide Film on the Cement Paste Side (30 days old, no silica fume)	1
6.4 Pozzolanic Reaction on the Top of Calcium Hydroxide Film (30 days old, 16% silica fume)	1
6.5 Densification of the Structure Behind the Calcium Hydroxide Film (30 days old, 16% silica fume)	1
6.6 Another View of the Good Bond Between the Calcium Hydroxide Film and the Matrix when Silica Fume is Used	1
6.7 Calcium Hydroxide Film Surrounded by a Dense Matrix (16% silica fume)	1
6.8 Distribution of Silica Fume Particles on the Steel Surface	1
6.9 Detail of the Partially Dissolved Particles of Silica Fume on the Interface	1
6.10 Pozzolanic Reaction on the Calcium Hydroxide Film	1

6.11 Detail of the Pozzolanic Reaction	1
6.12 Silica Fume Particles Embedded on the Calcium Hydroxide Film	1
6.13 Silica Fume Bridging a Crack in the Calcium Hydroxide Film	1
6.14 General Aspect of the Silica Fume Particles Dispersed in the Calcium Hydroxide Film	1
6.14a Detail of the Zone Delimited by the White Rectangle in Fig. 6.14	1
6.15 Calcium Hydroxide Preferential Orientation in the Transition Zone	1
6.16 Ettringite Distribution in the Transition Zone	1
6.17 Scanning Electron Micrograph of the Steel-Cement Paste Interface in the Presence of Condensed Silica Fume	1
6.18 Pozzolanic Reactions Product	1
6.19 Scanning Electron Micrograph of the Bulk Corrosion Products on the Interfacial Film	1
6.20 Dendritic Growth of Corrosion Products on the Interfacial Film	1
6.21 Scanning Electron Micrograph Showing the General Features of Corrosion products on the Interfacial Film	1
6.22 Scanning Electron Micrograph of Corrosion Products at Advanced Age Showing Spalling of the Interfacial Film	1
6.23 The Geometry of a Deformed Bar and the Mechanical Interaction Between the Bar and the Concrete	1
6.24 Schematic Representation of How the Radial Components of the Bond Forces Are Balanced Against Tensile Stress Rings in the Concrete in an Anchorage Zone	1
6.25 Failure Mode of the Pull-Out Specimen With Deformed Bar	1
6.26 Detail of the Failure Mode	1
6.27 Pull-Out Strength Versus the Concrete Compressive Strength	1
6.28 Pull-Out Strength in Function of the Concrete Compressive Strength and the Amount of Silica Fume	1
6.29 Pull-Out Strength in Function of the Tensile and Compressive Strength of Concrete	1

Chapter 1

INTRODUCTION

The purpose of this Thesis is to study some aspects of the microstructure of concrete and its effect on the behavior of concrete. The author is fully aware of his limitations and no attempt for completeness will be made. Rather, the main trust of this study is to construct a basic framework of some selected topics that the author feels relevant to characterize concrete as a multi-phased material.

Consider a piece of concrete (Fig. 1.1). The matrix that involves the aggregates is made of hydration products from the reaction between the cement and water. Many concrete properties are associated with the hydration at early stages, therefore chapter 2 analyzes the portland cement hydration using a new technique that permits the study of a fractured surface of cement paste in a fully hydrated state under a low temperature scanning electron microscope. It is important to compare the structure of the cement paste in the frozen-hydrated and frozen-dried state since water, an important component of the cement paste, is almost completely removed during freeze drying. This removal may alter the structures that can be seen in the scanning microscope. It should be mentioned that at 110 K, the paste has a substantial increase in mechanical strength, because water is converted from a liquid to a solid state and this permits the use of bulk specimens at very early hydration.

In concrete, the importance and usefulness of a hydraulic cement is given by its ability of producing hydration products that can bind discrete particles of rock forming a continuous and stable structural material. However, as it happens in many composite materials, the interface between the two phases has unique properties and quite often is a weak zone. This is an unfortunate fact, because the interfacial zone will be subjected to stress concentrations due to the elastic and thermal mismatch between the two phases (aggregate and matrix). Therefore, returning to the piece of concrete, it is

essential that the matrix should bond the aggregates to maintain the concrete integrity under load and aggressive environment. Chapter 2 discusses the mechanism of the interface formation using scanning electron microscope (SEM) and X-ray diffraction (XRD). Five types of rock and over 250 rock specimens were polished down to $0.25 \mu m$ to characterize the rock-cement paste interface as influenced by the age, mineralogical properties of the rock, cement type and levels of silica fume replacement.

Chapter 4, also, deals with the aggregate-cement paste interface, now trying to determine the mechanical properties of this bond both at a microstructural and engineering levels. The strength results of the aggregate-cement paste bond are subjected to a great variability, so an analysis of the bond strength using a probabilistic treatment of brittle strength was performed. The Weibull's statistical theory was used to analyze over 150 results of the aggregate-cement paste bond strength results.

So far, a fair amount of experimental analysis has been performed and it can characterize the original piece of concrete fairly well. However, the available mathematical descriptions of concrete are lacking the introduction of the microstructure in its formulation. Chapter 5 deals with this topic, deriving a generalized continuum theory for concrete, in which two extra variables that are not included in the traditional continuum mechanics: porosity of the matrix and aggregate content. Besides the basic usefulness of considering the matrix a porous medium, the formulation allows for variation of porosity, which may model localized higher porosity zones like the transition zone. The introduction of the aggregate content characterizes the composite nature of concrete.

The interaction of reinforcing steel and concrete is studied both in a microscopic and macroscopic level in chapter 6. One hundred steel specimens were polished down to one micron in order to study the steel-cement paste morphology as affected by age and level of silica fume. Also, the effects of chlorides were investigated in relation to

the corrosion of the reinforcing steel. The mechanical properties of the steel-concrete bond was determined by pull-out tests using 16 concrete mix design and two types of reinforcing bar. The correlation between the microstructure and the mechanical behavior was discussed.

Therefore, in summary, the study of the concrete microstructure was done step-wise: starting with the hydration of the cement paste (chapter 2) followed by how and how much it bonds with the aggregates (chapters 3 and 4), which gives bases for discussing cracking of concrete. Chapter 5 presents a generalized continuum theory for concrete as a porous and composite material. Finally with this information gathered, it is possible to discuss the mechanism of the steel-concrete bond as influenced by the existing microstructure, in chapter 6.

1.1 Summary of the Chapters

The chapters describing the work performed in this Thesis were divided in a form to make them as self-contained as possible. In order to help the reader to have an overall picture of the topics covered, a summary of the chapters is presented:

Chapter 2

The use of the frozen hydrated scanning electron microscopy (FHSEM) in the study of cement paste is described. This technique permits analysis of the fractured surface of cement paste in a fully hydrated state with water present as ice in a low temperature scanning electron microscope. At 110 K the paste has a substantial increase in mechanical strength, because water is converted from liquid to a solid state, and this permits the use of bulk specimens at very early hydration. Some results for 1 hour hydration are presented and future applications of this technique are discussed.

Chapter 3

The mechanism of the aggregate-cement paste formation is described for different types of rocks and cementitious materials. For portland cement, the formation of a film of calcium hydroxide crystals with a preferential orientation, c-axis perpendicular to the aggregate surface is described. The concentration of ettringite on the interface suggests a through-solution mechanism of cement hydration.

The expansive cement paste-aggregate interface is studied by scanning electron microscope and X-ray diffraction. Ettringite is the first crystal formed and it is precipitated in direct contact to the aggregate surface. This prevents

the formation of a continuous film of calcium hydroxide with a preferential orientation on the interface, instead large crystals of calcium hydroxide with a random orientation are precipitated there. These characteristics may explain the increase of mechanical strength when expansive cement is used instead of portland cement Type I.

The carbonate-cement paste transition zone is analyzed in detail. The results show that the formation of carboaluminates on the interface is questionable. Rather it seems that a reaction between the calcite and the calcium hydroxide film forming a basic calcium carbonate hydrated occurs.

The aggregate-mortar interface is studied by scanning electron microscope and X-ray diffraction. The thickness of the transition phase depends on the size and shape of the sand particles. These originate their own surface effects which interfere with those caused by the large aggregate.

Chapter 4

The aggregate-cement paste research performed by scientists of the last century which is not included in most state-of-the art reports is reviewed and many interesting results are analyzed in perspective.

Microhardness measurements were performed on the interfacial film and a comprehensive test program on the mechanical properties of the bond was conducted. The program included four types of rocks (basalt, amphibole-gneiss, granite and limestone) with three surface conditions (smooth, sand-blasted and rough) were tested at different ages. Since over 150 tests were conducted, it was possible to perform an analysis of the aggregate-cement paste bond using a probabilistic treatment of brittle strength. The Weibull's statistical theory was used with great success.

Chapter 5

A generalized continuum theory for concrete that includes the porosity of the matrix and the composite nature of concrete is developed. The fundamentals concepts for this theory are reviewed in some details and the balance equations for concrete are, then, developed. The laws of motion and the thermodynamic processes for fully saturated concrete are also studied. A general formulation of the constitutive postulates is discussed and the linear theory is analyzed as a particular case.

Chapter 6

The morphology of the steel-cement paste as affected by age and by the amount of silica fume is analyzed. The use of silica fume produces a remarkable densifying of the transition zone, which is responsible for the improved mechanical properties.

The interface between corroding steel and cement paste containing chloride, with and without condensed silica fume, was studied. For specimens containing only portland cement an interfacial film of large crystals of lime (CH) covered most of the steel surface. Even a 16% replacement of the portland cement with silica fume did not change this feature very much. However, only the specimens with silica fume developed corrosion. This indicates that the pore solution probably contained a higher Cl^-/OH^- ratio for a given total chloride content.

The mechanical properties of the steel-concrete bond as influenced by position of the bar, the type of bar (plain and deformed), concrete strength (4 levels) and amount of silica fume (3 levels) are analyzed in detail.

UNLOADED CONCRETE SPECIMEN

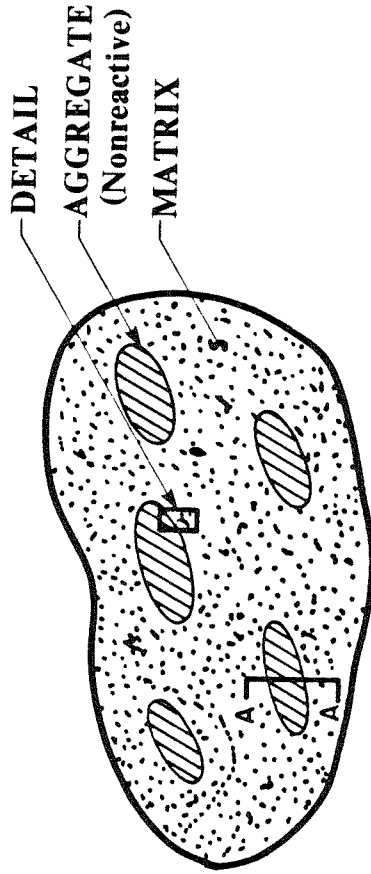


*Fig 1.1
Typical Volumetric Element of Concrete*

Chapter 2

CEMENT PASTE EARLY HYDRATION

2.1 Brief Review of the Portland Cement Hydration

The anhydrous compounds of portland cement when in contact with water decompose to form hydration products. There is a transitory period in which supersaturated solutions develop, however, the hydration products deposit thereafter. Le Chatellier (2.1) was the first to scientifically describe the hydration mechanism of the portland cement paste. He proposed the following sequence:

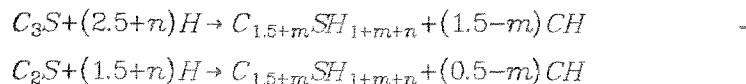
1. Chemical phenomena of dissolution of anhydrous cement compounds
2. Physical phenomena of crystalization of hydrates
3. Mechanical phenomena of hardening (interlacement of fibrous crystals and their adhesion to each other)

This mechanism, by which the cement compounds dissolve to produce ions in solution that will recombine to form precipitated hydrated products is thus believed to be "through-solution". Hansen (2.2) suggested that the reactions take place without the cement compounds going into solution by a "topochemical" or "solid-state" reaction. His arguments were based on the fact that alumina and silica have very low concentrations in the liquid phase, therefore the through-solution mechanism could not explain the observed fast rates of reaction.

Lea (2.3) suggested that both through-solution and solid-state type reactions probably occur, the former predominating in the early stages of hydration and the latter during the later stages when the diffusion has become more difficult. However, the debate is not by all means over.

2.1.1 Hydration of the calcium silicates (C_3S, C_2S)*

The hydration of the calcium silicates can be shown by the reactions:



The product CSH is a poorly crystalline calcium silicate gel whose composition changes during the period of hydration. The CSH is almost amorphous, therefore X-ray diffraction gives little information as to the structural composition. Diamond (2.4) reported a diffuse X-ray powder pattern at 2.6 - 3.1 Å and a somewhat sharper one at 18 Å . The CSH has a variable composition and a C/S mole ratio ranging between 2 and 3, also the gel can incorporate Al , \bar{S} , and Fe ions. The gel has a very high surface area around 900 m^2/g .

There are two basic assumptions about the CSH structure (2.5) :

1. It is a layer structure.
2. When the silicate ions polymerize, they do so in a way that produces chains.

According to Diamond (2.4) the CSH may be classified in four morphological types:

CSH (I): poorly crystallized foils and C/S ratio between 0.8 and 1.5

CSH (II): reticular network with C/S ratio between 1.5 and 2.

CSH (III): small irregular equant or flattened particles no more than 0.3 μm across (2.6).

CSH (IV): inner product.

Hexagonal plates of calcium hydroxide appear at early stages, and as hydration continues more CH crystals are deposited and may encapsulate other regions of the paste containing gel, and some of the precise hexagonal outline is lost.

* See nomenclature for notation.

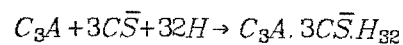
Skalny et al. (2.7) proposed the following sequence for C_3S hydration.

- Stage I C_3S has a rapid initial hydration, and Ca^{2+} is quickly released into solution.
- Stage II Induction (or dormant) period develops. Slow increase of Ca^{2+} concentration occurs in this period.
- Stage III $Ca(OH)_2$ crystallizes from solution, and C_3S hydrates generating heat.
- Stage IV Intermediate stage approaches a diffusion controlled rate of C_3S hydration.
- Stage V Hydration is diffusion controlled.

2.1.2 Hydration of the Calcium Aluminates (C_3A, C_4AF)

The diffusion through the "hexagonal hydrates" (C_4AH_{13} and C_2AH_8) layer that forms at the surface of the C_3A grain controls its hydration. However, since these hydrates convert rapidly to C_3AH_6 the barrier does not persist and the C_3A grain hydrates completely.

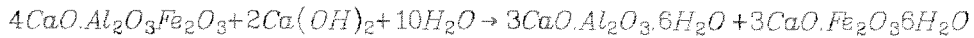
To retard the C_3A hydration, gypsum is normally added to the portland cement. The gypsum ($CaSO_4 \cdot 2H_2O$) reacts with the C_3A to form calcium sulphoaluminates, the trisulfoaluminate is often referred to as ettringite.



Moore and Taylor (2.8) reported that ettringite has a crystal structure based on columns of empirical composition, $Ca_3[Al(OH)_6] \cdot 12H_2O^{3+}$, which run parallel to the c-axis. The sulfate ions and the remaining $17H_2O$ molecules lie between the channels.

Mehta (2.9,2.10) studied the formation of ettringite using SEM. He proposed that the needle-like morphology of ettringite could only be explained by a through-solution reaction mechanism. The precise details of the ettringite formation will be discussed in Chapter 3 for expansive cement.

The hydration of the C_4AF is not so well understood; the following reaction has been suggested (2.11):



2.2 Low-Temperature Scanning Electron Microscope Analysis of the Portland Cement Paste Early Hydration

The morphology and composition of cement paste hydration products have been determined by a number of researchers using the scanning electron microscope (SEM), and a great amount of information was gathered. Chatterji and Jeffery (2.12), Mills (2.13), Williamson (2.14) were pioneers in this technique, and their results contributed to the understanding of the hydration. Diamond's studies (2.15) with a scanning electron microscope-energy dispersive X-ray spectrometer combination eliminated much of the guesswork in interpreting the various crystal morphologies existing in the hardened cement paste. Recently intensive research is being carried out by Dalglish and Ible (2.16), Dalglish et al. (2.17) using a thin-foil of hardened cement paste for examination in an analytical scanning transmission electron microscope (STEM) to study hydration.

Unfortunately, with the use of the scanning electron microscope the cement paste is exposed to a vacuum so that most of the water is lost, and there is no information on how this affects the morphology of the hydration products. Also there is an intrinsic difficulty in preparing samples for the early hydration analysis because the cement paste has very little cohesion in the first hours of hydration, and it has been reported (2.17) that samples hydrated for less than 10 hours collapsed to powder during freeze-drying, necessitating mounting these particles on double-sided adhesive tape.

In order to overcome these problems and to study the hydration products at the early ages without the damage caused by water removal, research with the frozen hydration process was conducted. This technique uses low temperatures to prepare the sample in such a way that the water freezes without damaging the structure of the sample which is then examined and analyzed on a cold stage inside the low temperature scanning electron microscope. This method is used for biological research;

Kynaster and Paden (2.18), Echlin et al. (2.19), Pawley and Norton (2.20) reported devices for maintaining samples at low temperatures while they were being analyzed in the SEM.

The use of low temperatures to prepare the sample produces a substantial increase in the strength of the paste as the water is converted from liquid to a solid state. A similar increase of strength has already been reported for mortar and concrete exposed to cryogenic temperatures by Monfore and Lentz (2.21), Tognon (2.22), Rostasy et al. (2.23). This makes it possible to study the very early hydration of bulk specimens, and it also permits the examination of large areas of the sample at low temperatures, reducing the contamination (2.24) and the rate of thermal damage to the specimen (2.25).

The quenching of the sample at low temperatures (-196°C) arrests the cement hydration, immobilizes the liquid water, and stops the movement of dissolved substances. Special care was taken to minimize the size of ice crystals in the frozen sample because of the potential damage they may produce to the sample structure during expansion. It was also important to assure that the sample was really in the frozen-hydrate state. For biological materials a number of criteria have been proposed by Moreton et al. (2.26), Saubermann and Echlin (2.27), Gupta et al. (2.28) and Varriano-Marston et al. (2.29). One simple approach is to be certain that the temperature of the specimen throughout preparation and examination is below that at which appreciable sublimation and melting occur. The recrystallization temperature of the water is 143 K, and it is usually suggested (2.30) that 123 K is a safe temperature to prevent significant ice crystal growth, sublimation, or even melting in the frozen samples.

The purpose of this research is to present the use of FHSEM to analyze cement paste hydration and to show some results on early hydration.

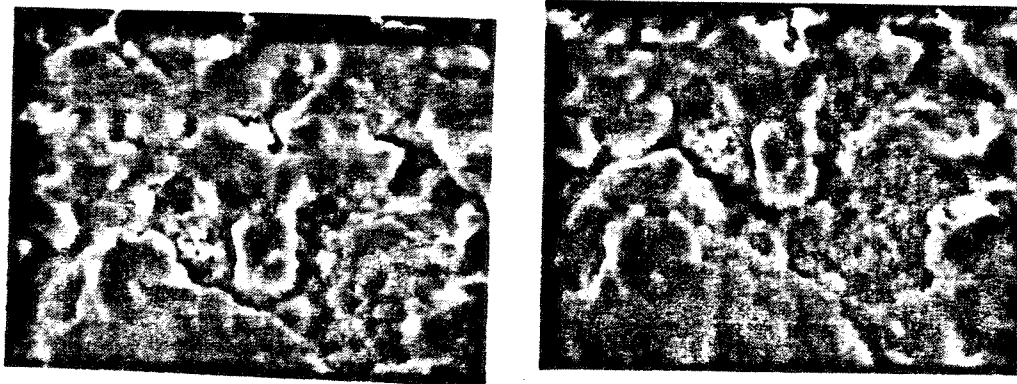


FIG. 2.3
STEREO PAIR SHOWING THE TOPOLOGY OF THE CEMENT PASTE. SMALL RODS OF ETTRINGITE ON THE SURFACE OF THE CEMENT PARTICLES CAN BE SEEN. PICTURE WIDTH = $27\mu\text{m}$.



FIG. 2.2
UNCOATED SAMPLE OF CEMENT PASTE INSIDE THE MICROSCOPE AT 110K.



FIG 24
DETAIL OF A CEMENT PARTICLE
SURROUNDED BY SMALL ROD CRY-
STALS 1 HOUR HYDRATION.
UNCOATED SPECIMEN EXHIBITS
CHANGING. PICTURE WIDTH = 14 μ m.

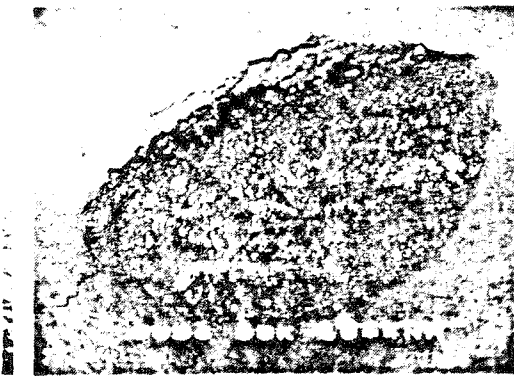


FIG 25
USEFUL FRACTURE OF THE
CEMENT PASTE.

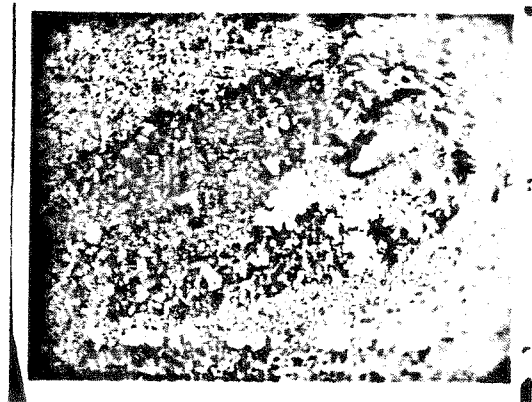


FIG 26
CONCENTRATION OF MATERIAL ON
THE TOP OF THE FRACTURE PLANE.

this magnification is the upper limit before the sample starts to charge. Charging can be reduced by coating with a thin layer of gold, which allowed magnifications of up to 15,000X to be achieved.

After the test of the 1-hour cement paste was performed, the sample was freeze-dried in order to compare the results using a Hitachi SEM at normal temperatures. Fig. 2.5 shows the surface of the fracture produced by the cold knife, a clean and non-contaminated surface. The same cannot be said for the surface shown in Fig. 2.6, however, where on the top of the surface there is a concentration of extraneous materials due to charging effects. This has been observed during scanning electron microscopy of a variety of materials, where particles from outside the viewing field are attracted to the charged surface of the sample. It should be mentioned that the freeze-dried sample had to be coated, because even using an acceleration voltage of 5 kV the charging was so intense that the sample could not be imaged, while at low temperature magnification of 5000 X was obtained with little charging. The original intent of checking the difference between the two processes was not successful because of the difficulty of locating the same position, therefore in future work the sample will be freeze-dried inside the microscope and reanalyzed without being removed. It is important to compare the structure of the cement paste in the frozen-hydrated and frozen-dried state since water, an important component of the cement paste, is almost completely removed during freeze-drying. This removal may alter the structures that can be seen in the scanning microscope.

The use of low-temperature methods allows morphological and analytical studies of the cement paste, and some new light may be cast on the following:

1. Verification of hydration products morphology in a frozen hydrated state compared to the dried state. Of special interest would be checking the existence of the CSH morphologies proposed by Diamond (2.4) and the presence of Hadley's grain (2.32, 2.33) in the frozen hydrated cement paste.

2. A analysis of the expansion mechanism associated with the ettringite formation in the cement paste. There are two main models to explain this mechanism: crystal growth theory (2.34,2.35,2.36,2.37) and the swelling theory (2.9,2.38). Since the latter is based on the fact that the colloidal ettringite is able to attract a large number of water molecules which cause interparticle repulsion, the study of the frozen hydrated sample which keeps the water within the system may give some extra information on the validity of this model.

3. Understanding the mechanism of the cement paste early hydration by the performance of elemental analysis with cryofixation of the paste in combination with other techniques.

4. Study of the ice formation in the hardened cement paste by cooling the sample at a slow rate and then analyzing the damage produced by the ice formation.

2.3 References

- 2.1 Le Chatellier, *The Constitution of Hydraulic Mortars*. McGraw Hill, New York, 1905.
- 2.2 Hansen W.C., Mat. Res. Stand. 2, 490, 1962, cited in Lea, (2.3) pp. 179.
- 2.3 Lea F.M., *The Chemistry of Cement and Concrete*. Chemical Publishing CO.,INC, New York N.Y., 1971.
- 2.4 Diamond S., "Cement Paste Microstructure- An Overview at Several Levels in Hydraulic Cement Pastes: Their Structure and Properties". Cement and Concrete Assoc., Slough, pp. 2-30, 1976.
- 2.5 Taylor H.F.W., "Cement Hydration Reactions: the Silicate Phases". Cement Production & Use, Proc. Eng. Found. Conf., 1979.
- 2.6 Diamond S. and Lachowski E.E., "On the Morphology of Type III CSH Gel". Cement and Concrete Research, 10, 703, 1980.

- 2.7 Skalny J., Jawed I. and Taylor H.F.W., *World Cement Technology*, 183, 1978.
- 2.8 Moore A.E. and Taylor H.F.W., "Crystal Structure of Ettringite". *Acta Cryst.*, B36, 386, 1970.
- 2.9 Mehta P.K., "Scanning Electron Micrographic Studies of Ettringite Formation". *Cement and Concrete Research* 3, 1, 1976.
- 2.10 Mehta P.K., "A Reply to W.C. Hansen", Discussion of the paper above, *Cement and Concrete Research*, 6, 597, 1976.
- 2.11 Illston J.M., Dinwoodie J.M., Smith A.A. *Concrete, Timber and Metals*. Van Nostrand Reinhold Company, New York, 1979.
- 2.12 Chatterji S. and Jeffery J.W., "Three Dimensional Arrangement of Hydration Product in Set Cement Pastes". *Nature*, 209, 1233-1234, 1967.
- 2.13 Mills R.H., "Collapse of Structure and Creep in Concrete". Proceedings of an International Conference on Structures, Solid Mechanics and Engineering Design of Civil Engineering Materials, Southampton, 1969.
- 2.14 Williamson R.B., "Portland Cement: Pseudomorphs of Original Cement Grains Observed in Hardened Pastes". *Science*, 164, 549, 1969.
- 2.15 Diamond S., "Identification of Hydrated Cement Constituents Using a Scanning Electron-Microscope-Energy Dispersive X-Ray Spectrometer Combination". *Cement and Concrete Research*, 2, 617, 1972.
- 2.16 Dalglish B.J. and Ibe K., "Thin-Foil Studies of Hydrated Portland Cement". *Cement and Concrete Research*, 11, 729, 1981.
- 2.17 Dalglish B.J., Pratt P.L. and Moss R.I., "Preparation Techniques and Microscopical Examination of Portland Cement Paste and C_3S ". *Cement and Concrete Research*, 10, 665, 1980.
- 2.18 Kynaster P. and Paden R.S., Advances in techniques and instrumentation for the stereoscan. *Cambridge Stereoscan Colloquium*, 109, 1970.

- 2.19 Echlin P., Paden R., Donzek B., Wayte R., "Scanning Electron Microscope of Labile Biological Material under Controlled Conditions". In Scanning Electron Microscope, Proceedings of the 3rd. Annual Scanning Electron Microscopy Symposium, Ed. by O. Johari pp. 51, IIT Research Institute, Chicago, Illinois, 1970.
- 2.20 Pawley J.B. and Norton J.T., "A Chamber Attached to the SEM for Fracturing and Coating Frozen Biological Samples". *J. Microsc.*, 112, 169, 1978.
- 2.21 Monfore and Lentz, "Physical Properties of Concrete at Very Low Temperatures". *Journal of the PCA Research and Development Laboratories*, 1962.
- 2.22 Tognon G., "Behavior of Mortar and Concrete in the Temperature Range from 20 C to -196 C". *Proceedings of the 5th International Symposium on the Chemistry of Cement*, Tokyo, 1968.
- 2.23 Rostasy F.S., Schneider V. and Wiedemann G., "Behavior of Mortar and Concrete at Extremely Low Temperatures" *Cement and Concrete Research*, 9, 365, 1979.
- 2.24 Echlin P., Saubermann A.J. and Taylor P., "Contamination in the Scanning Electron Microscope". *Proc. 8th Ann. IITRI-SEM Symp.* 679, 1975
- 2.25 Hall T.A. and Gupta B.L., "Beam-Induced Loss of Organic Mass Under Electron Microprobe Conditions". *J. Microsc.* 100, 177, 1974
- 2.26 Moreton R.B., P. Echlin P., Gupta B.L., Hall T.A. and Weis-Fogh T., "Preparation of Frozen Hydrated Tissue Sections for X-ray Microanalysis in the Scanning Electron Microscope". *Nature*, 247, 113, 1974.
- 2.27 Saubermann A.J. and Echlin P., "The Preparation, Examination and Analysis of Frozen Hydrated Tissue Sections by Scanning Transmission Electron Microscopy and X-ray Microanalysis". *J. Microsc.*, 105, 155, 1975.
- 2.28 Gupta B.L., Hall T.A., Maddrell S.M.P. and Moreton R.P., "Distribution of

- Ions in a Fluid Transporting Epithelium Determined by Electron-Probe X-ray Microanalysis'. *Nature*, 264, 284, 1976.
- 2.29 Varriano-Marston E., Gordon J., Davis E.A. and Hutchinson T.E., "Cryomicrotomy Applied to the Preparation of Frozen-Hydrated Muscle Tissue for Transmission Electron Microscopy". *J. Microsc.* 109, 195, 1977.
- 2.30 Echlin P., "Cryofracturing and Low Temperature Microscopy of Plant Material". *J. Microsc.* 112, 47, 1977.
- 2.31 Hayes T.L., "Biophysical Aspects of Scanning Electron Microscopy". *Scanning Electron Microsc.* I. 1, 1980.
- 2.32 Pratt D.L. and Ghose A., "Electron Microscope Studies of Portland Cement Microstructures During Setting and Hardening". *Phil. Trans. R. Soc. Lond.* A310, 93, 1933.
- 2.33 Barnes B.P., Diamond S. and Dolch W.L., "The Contact Zone Between Portland Cement Paste and Glass "Aggregate" Surfaces". *Cement and Concrete Research*, 8, 263, 1978.
- 2.34 Hansen W.C., *Proc. ASTM* 63, 932, 1963.
- 2.35 Ish-Shalom M. and Bentur A., "Properties of Type K Expansive Cement of Pure Components; I. Hydration of Unrestrained Paste of Expansive Components. Results". *Cement and Concrete Research*, 4, 519, 1974.
- 2.36 Bentur A. and Ish-Shalom M., "Properties of Type K Expansive Cement of Pure Components; II. Proposed Mechanism of Ettringite Formation and Expansion in Unrestrained Paste of Pure Expansive Component". *Cement and Concrete Research*, 4, 709, 1974.
- 2.37 Ish-Shalom M. and Bentour A. "Properties of Type K Expansive Cement of Pure Components; III. Hydration of Pure Component Under Varying Restraining Conditions". *Cement and Concrete Research*, 5, 139, 1975.

- 2.38 Mehta P.K., 'Effect of Lime on Hydration of Pastes Containing Gypsum and Calcium Aluminates or Calcium Sulfoaluminates'. J. Am. Ceram. Soc. 56, 315, 1973.

CHAPTER 3

MICROSTRUCTURE OF THE AGGREGATE- CEMENT PASTE TRANSITION ZONE

3.1 Introduction

The transition zone between the aggregate and the cement paste has been analyzed by many researchers. Farran (3.1,3.2) observed that calcium hydroxide crystals would grow preferentially in the contact zone between the cement paste and the aggregate. Subsequently, Maso (3.3) set forth the hypothesis that there is a transition zone due to the different diffusion of ions in the cement paste near the aggregate. Interest in the interface increased after Hadley (3.4), using a scanning electron microscope and X-ray spectrometer combination, was able to describe many interesting processes that occur at the interface. His experimental results made it possible to describe the interface formation by the following mechanisms: A layer of CH film is precipitated with the c-axis perpendicular to the aggregate surface and over this film a CSH layer is formed, creating a composite or "duplex" film. This film will be bound to the bulk paste by the growth of large impure CH crystals as hydration continues. Barnes (3.5) studied the morphology of the paste-aggregate interface using four different portland cements (including a portland blast furnace slag) and confirmed most of Hadley's conclusions. However, Struble and Mindess (3.6) reported that the layer of well-oriented calcium hydroxide crystals on the interface did not constitute a duplex-film.

Iwasaki and Tomiyama (3.7) suggested the three following stages during the interface formation: precipitation of ettringite needles over the aggregate, precipitation of calcium hydroxide plates, densification of the contact film.

Parallel work done by French researchers showed the existence of an "auréole de transition" (3.8) around the aggregate. Perrin (3.9), using a transmission electron microscope showed that, in the auréole, the hydration crystals were different from the ones formed in the bulk cement paste. Grandet and Ollivier (3.10) were able to analyze the change of hydration products from the very interface to the bulk cement paste by using X-ray diffraction and a process of successive abrasion of the interface.

This chapter describes an investigation on the the morphology of interface between the cement paste and different types of rock (marble, limestone, quartz, granite, chert, opal, quartzite, agate, smoky quartz). The study includes the analysis of the interface when different cementitious materials are used (portland cement, silica fume, alite, expansive cement). The mechanical properties of the interface will be discussed in chapter 4. The experimental analysis and the materials used are reported in section 3.2. The quartz-cement paste is studied first (section 3.3) because quartz is an inert aggregate and therefore it enables the analysis of the interface without worrying with the effect of the aggregate mineralogy. The formation of calcium hydroxide and ettringite on the transition zone is described. The effect of the aggregate mineralogy is researched in detail (section 3.4) for marble and limestone because it is a well known fact that carbonate rocks have a beneficial reaction with the cement paste hydration products increasing the mechanical strength of the concrete, however the precise reaction mechanism is not fully understood. Finally, the mortar-aggregate transition zone in which the sand particles are introduced as another parameter is discussed in section 3.5.

3.2 Experimental Methods

3.2.1 Materials

The type and number of rock specimens are shown in Table 3.1 Some of their basic characteristics are given below:

Table 3.1
Type of Rock Used for the Interface Study

Aggregate Type	Number of Polished Specimens
Quartz	91
Marble	65
Limestone	10
Granite	25
Opal	9
Quartzite	20
Agate	10
Smoky Quartz	15
Chert	22

Marble: Consisted mainly of recrystallized calcite with some detrital quartz and possibly pyroxene (See Figs. 3.1 and 3.2).

Limestone: Consisted mainly of very fine grained calcite (a calcite mud, micrite), Fig.3.3. Poorly solidified sediments were cemented by recrystallized calcite. Recrystallized calcite are also present in voids. Minor detrital quartz grains are present and a trace of microcrystalline quartz also fills the voids.

Quartz: Single crystal of SiO_2 .

Chert: Consists almost entirely of microcrystalline quartz with some voids filled with chalcedony or secondary quartz, Fig.3.4. Minor amount of secondary dolomite crystals were present and a trace amount of clay.

Opal: Almost completely amorphous as shown in Fig. 3.5

ASTM type II portland cement was used; its composition is shown in Table 2.1. Also alite and expansive cement type K were employed. The chemical analysis for the alite is shown in Table 3.2.

Silica fume with a particle size distribution as shown in Fig. 3.6 was also used as a pozzolanic admixture. About 82% of this material was finer than $1\mu m$ and 36% finer than $0.2\mu m$, with $2.2g/cm^3$ density. The densities of the portland cement pastes (0.35 w/c) with 0%, 5% and 16% are 2.11, 1.98 and $1.79 g/cm^3$ respectively.

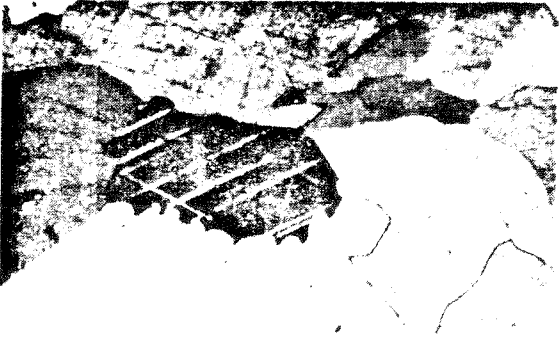


Fig 3.1
Calcite Grains (39X, Bruzed Niob.)

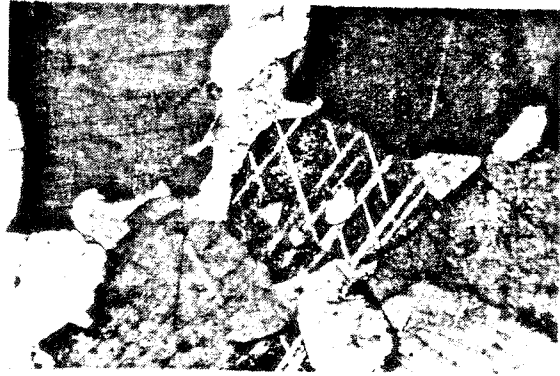


Fig 3.2
Cleavage Planes in the Calcite Grains
(39X, Bruzed Niob.)

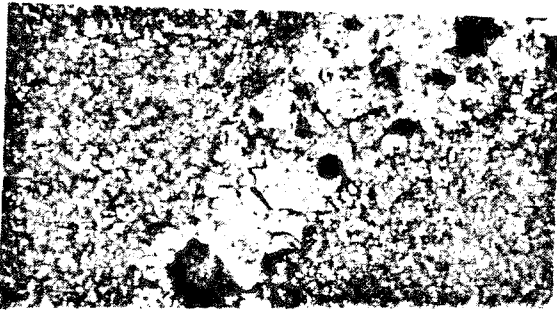


Fig 3.3
General View of Limestone (156X, Bruzed Niob.)

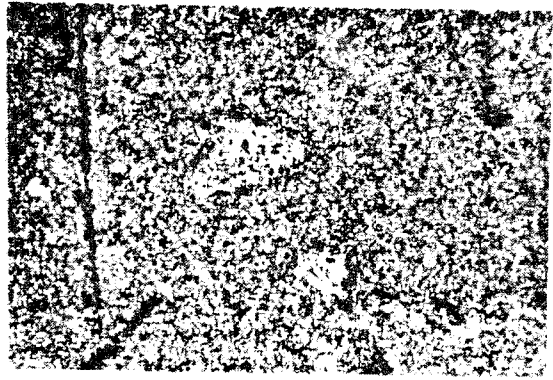


Fig 3.4
General View of Chert (39X, Bruzed Niob.)

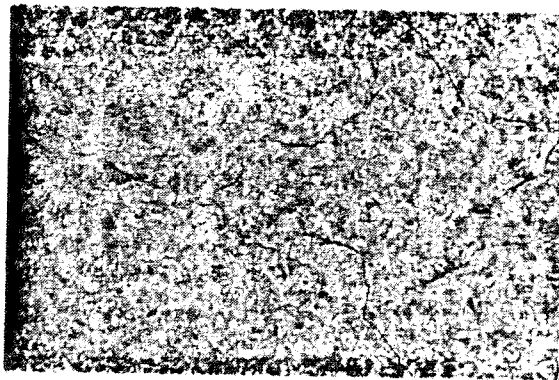


Fig 3.5
Amorphous Nature of Opal (390X, Bruzed Niob.)

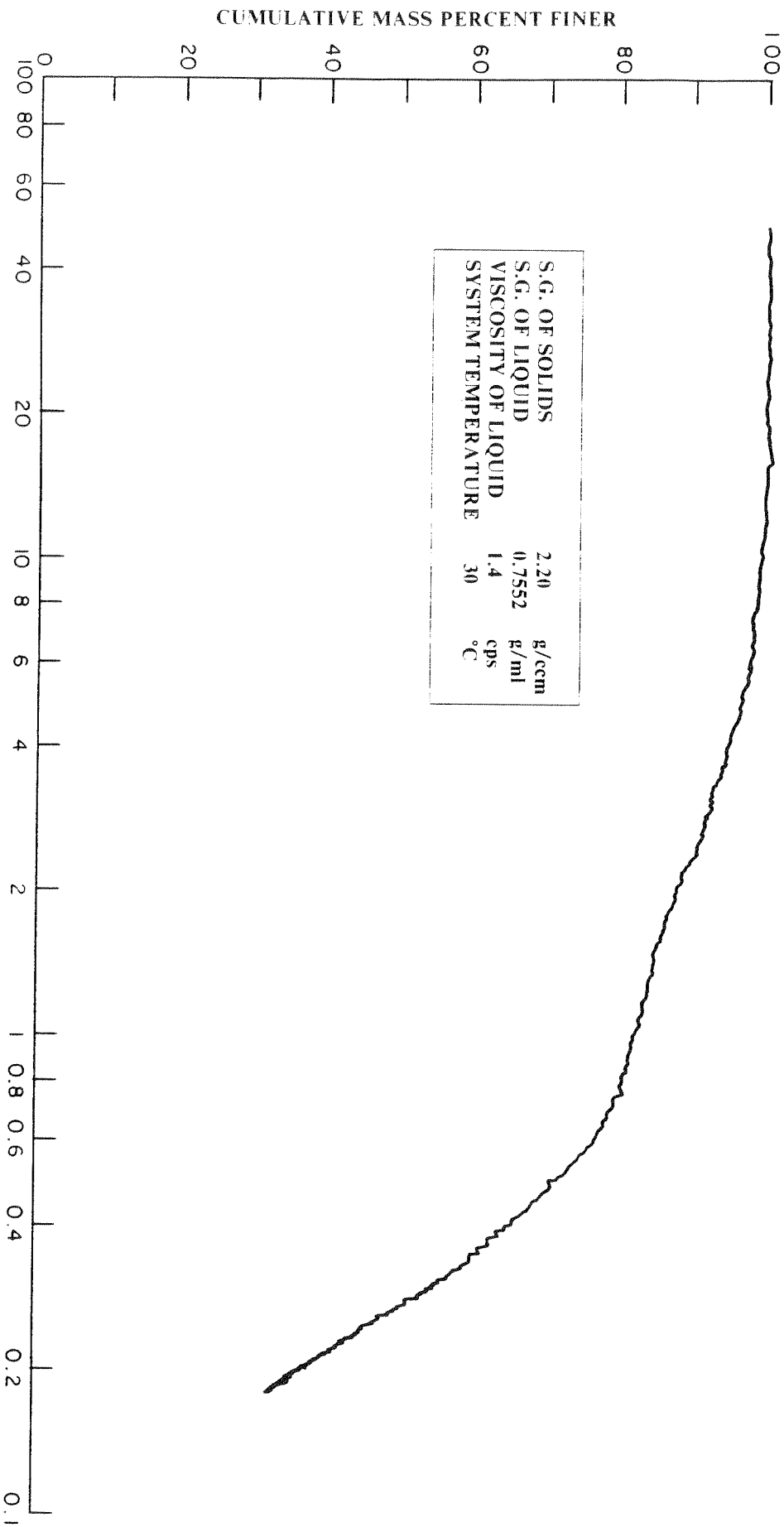


FIG. 3, 6
Particle Size Distribution Of Microsilica By X-Ray Sedimentation

Table 3.2

Chemical Properties of the Alite	
Chemical Analysis	
Compound	Percent
Silicon dioxide, SiO_2	23.33
Aluminum oxide, Al_2O_3	0.44
Ferric oxide, Fe_2O_3	0.87
Calcium oxide, CaO	67.92
Magnesium oxide, MgO	2.14
Sulfur trioxide, SO_3	0.07
Sodium oxide, Na_2O	0.02
Potassium oxide, K_2O	0.03
Free Lime, CaO	1.89
Loss on Ignition	5.02

3.2.2 Specimens and Test Procedure

The study of the interface microstructure was performed using a composite specimen, consisted of cement paste cast against a polished surface of aggregate. For the purposes of measuring accurately the thickness of the hydration products formed at the interface it was essential that the surface of the rock was polished down to 0.25 microns. At some specified ages, the specimen was broken at the very interface of the two distinct materials (Fig. 3.7). The two halves obtained from the composite specimen were analyzed by a scanning electron microscope (SEM) attached to an energy dispersive analysis (EDAX) and by X-Ray diffraction (XRD).

The aggregate surface was polished according to the following sequence:

1. The rock was cut by a slow speed saw to minimize the formation of microcracks.
2. Next, the rock was polished sequentially to 90 μm and 15 μm in a Planopal machine.
3. The rock was then mounted in an epoxy frame and placed in a Syntron machine with diamond paste to polish progressively down to 6, 1, 0.25 μm .

The micrographs in Figs. 3.8 and 3.9 show the difference of a granite just after being sawed (Fig. 3.8) and after the polishing process (Fig. 3.9). As expected, the polishing process could not eliminate the natural flaws of the rock.

TESTING OF INTERFACE

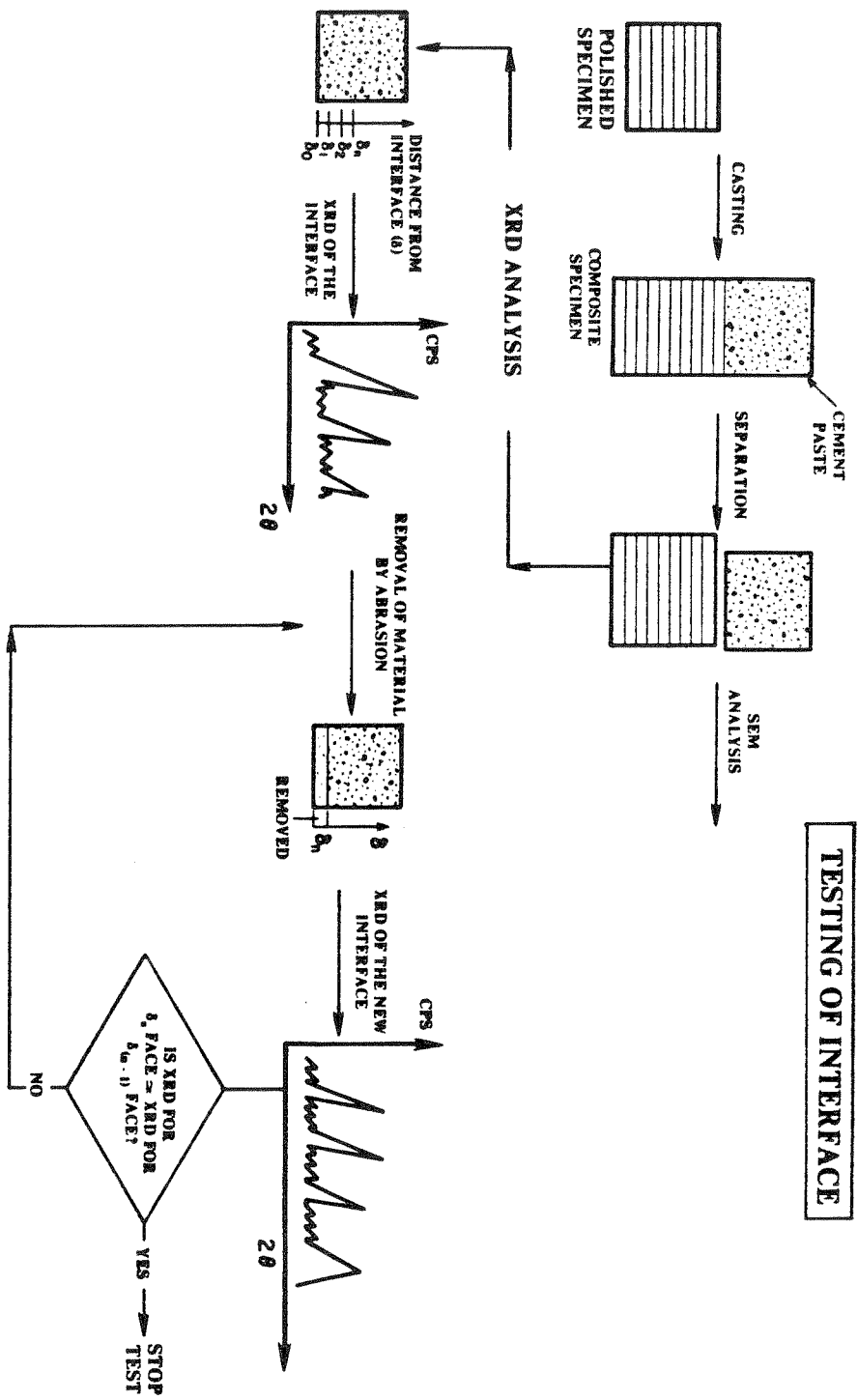


Fig 3.17
Test Procedure

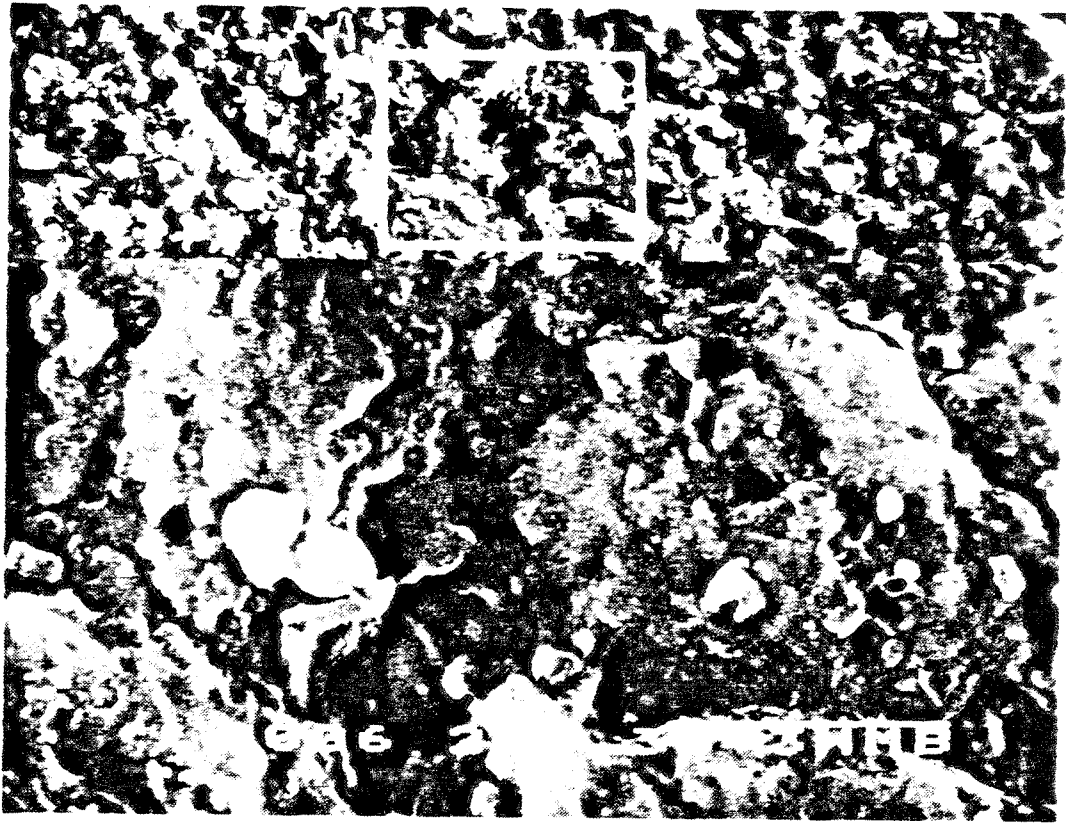


Fig. ^{3.8} 6 (above) and ^{3.9} 7 shows the difference of the granite surface before and after the polishing process (down to 0.25 microns). The white box zone is amplified to 5000 X.

The aggregate had a cylindrical form and a diameter of 3/4". A PVC tube with the same diameter was mounted on top of the polished face of the of the aggregate. RTV 108 Silicone Rubber was used as a cement and sealant device.

Cement paste was cast (with 0.35 w/c) and the composite specimen was covered with Saran wrap and stored in a fog room. At specified ages the specimens were removed from the fog room and placed on a dessicator with drierite for drying. Due to the drying shrinkage the cement paste and the aggregate separated at the very interface.

Acetone was used to stop hydration. The specimens were then stored in a dessicator containing silica gel (55 % R.H.) and A scarite (to avoid carbonation).

The specimens for the SEM analysis were coated with a layer of gold and stored in the dessicator containing silica gel and A scarite.

In some of the specimens, the interface on the cement matrix side was analyzed by XRD, and then this surface was removed by abrasion and the new surface was reanalyzed. This iteration would stop when the results of XRD on consecutive surfaces was practically the same (Fig. 3.7). Silicon Carbide paper (400 and 600 grit) was used as the abrasive medium to successive removal of material from the interface. This material was weighed in a balance with 0.1 mg precision, so by knowing its density the distance from the interface could be determined. It was assumed, however, that the density of the interface layers was the same as that of the bulk cement paste. This is not true since the density of the interface should be smaller. The lack of accurate density data for the interface layers does represent an inherent flaw of this process, which prevent it from being fully quantitative; however it does show important features when used for comparative purposes.

3.2.3 Equipment

The morphology study was performed using a Hitachi Scanning Electron Microscope, model S-415 A, which had a magnification power up to 150,000 X. An X-ray

detector was attached and that allowed various scanning modes needed for elemental analysis.

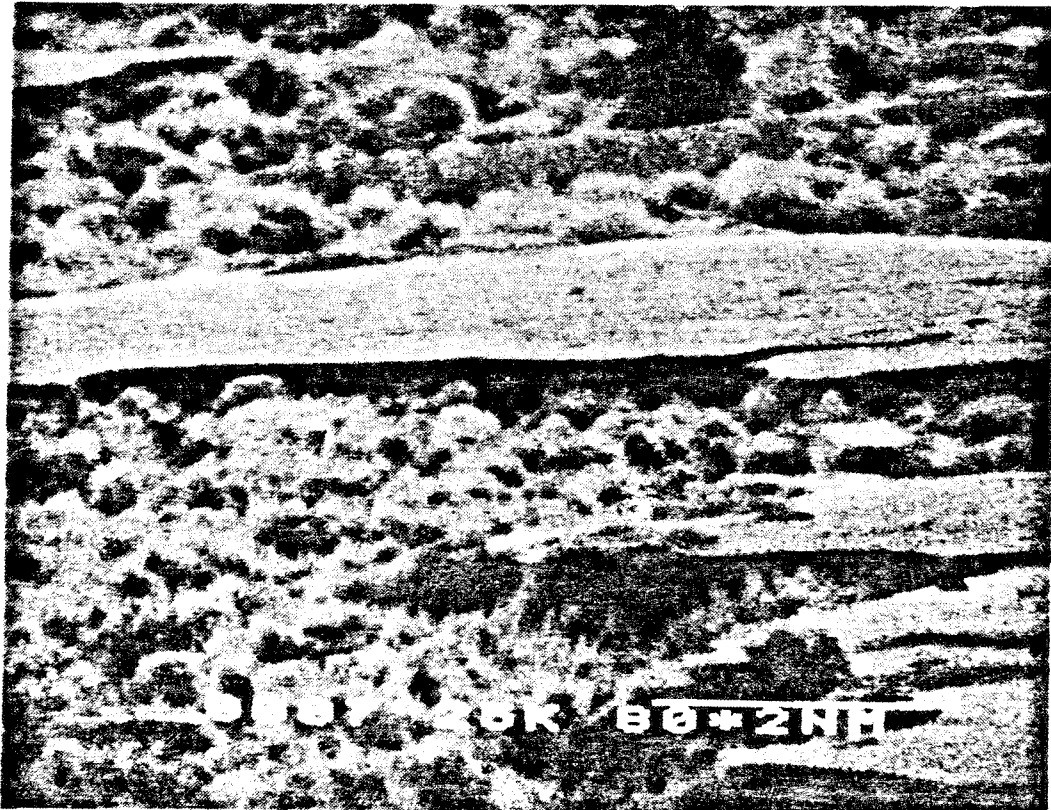
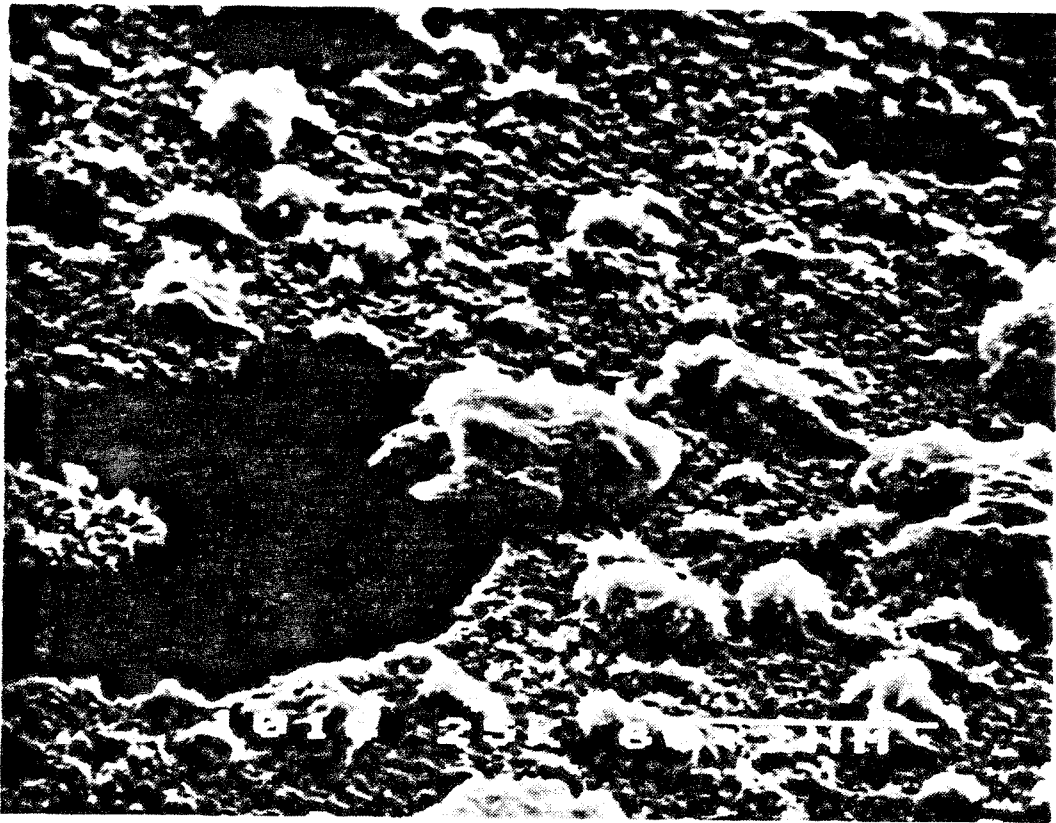
The mineralogical composition of the interface was analyzed with a Rigaku X-ray diffraction equipment attached to a computer terminal.

3.3 Quartz-Cement Paste Interface

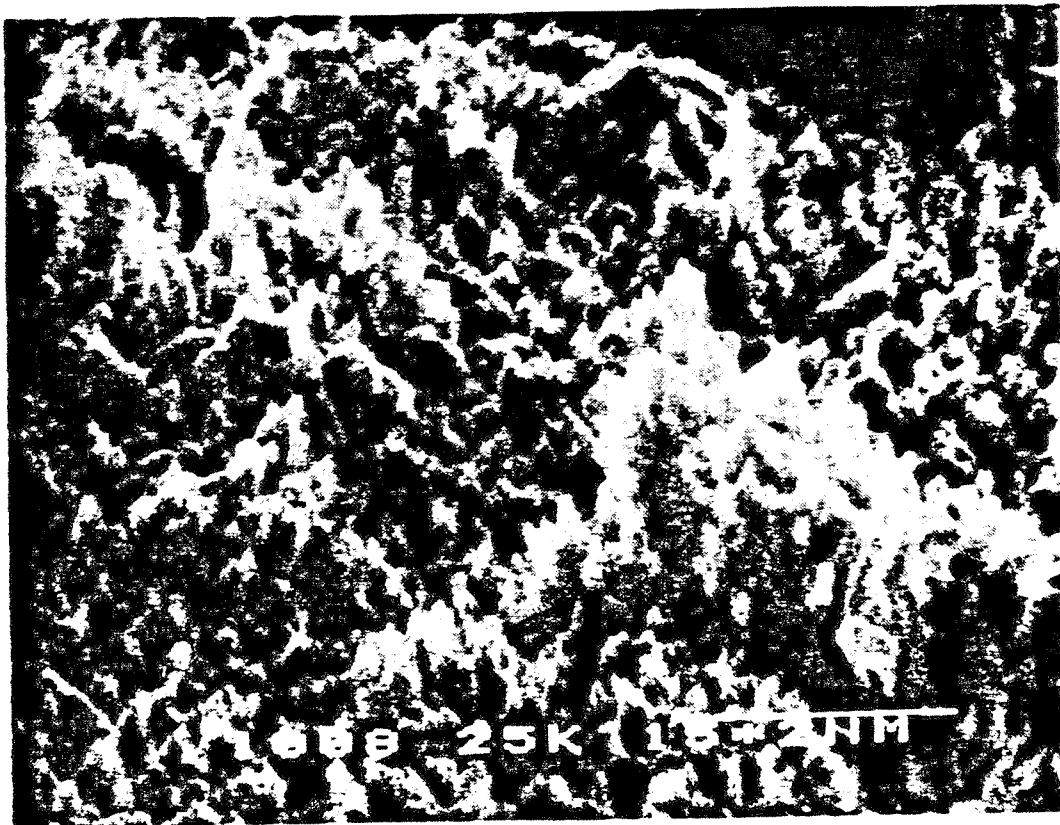
The surface effects produced by the aggregate face create a film of water or zones of paste with a higher w/c ratio at the interface. This extra water permits the ions to diffuse more easily and at the same time eliminates some of the geometrical constraints that exists in the bulk cement paste, causing higher porosity and the formation of larger crystals in the interfacial zone.

Fig. 3.10 shows the typical morphology of the hydration products over the aggregate face. The flat dark zone is the polished aggregate; the reticular products can be easily identified as CSH and we can see that the outer products of the cement grain interlock with the CSH layer. The topology resembles a lake (aggregate), a valley (CSH) and hills (hydrated cement grain). This picture is reversed on the cement paste side, producing a plateau, a valley and a depression respectively. The plateau, as shown in Fig.3.11, is formed by a film of CH oriented with the c-axis normal to the aggregate face. The valley is again constituted by CSH and the depression is the empty zone produced either by the natural porosity or the cement grains that remained on the aggregate side. Fig. 3.12 shows the reticular morphology of the CSH, that grows on the CH film deposited over the interface.

One of the most interesting phenomena in the transition phase is the presence of many the 'Hadley grains', which are cement particles that during hydration deposits a shell around themselves and dissolve away partly or completely. This is seen in Fig. 3.13. The completely hollow shell on the bottom left consists of CSH gel. This type of morphology suggests that the cement grains hydrated by a "through-solution"



³¹⁰
 Fig. 8 (above) shows a typical morphology of the hydration products over the aggregate (dark zones). Fig. 9 shows the interface morphology on the cement paste side.
³¹¹



³¹²
Fig. 16 Shows a micrograph amplified 20,000 X of the CSH over the interfacial film. The cement paste had 0.35 w/c ratio and was cast against a granite. The specimen was 19 days old when it was broken.

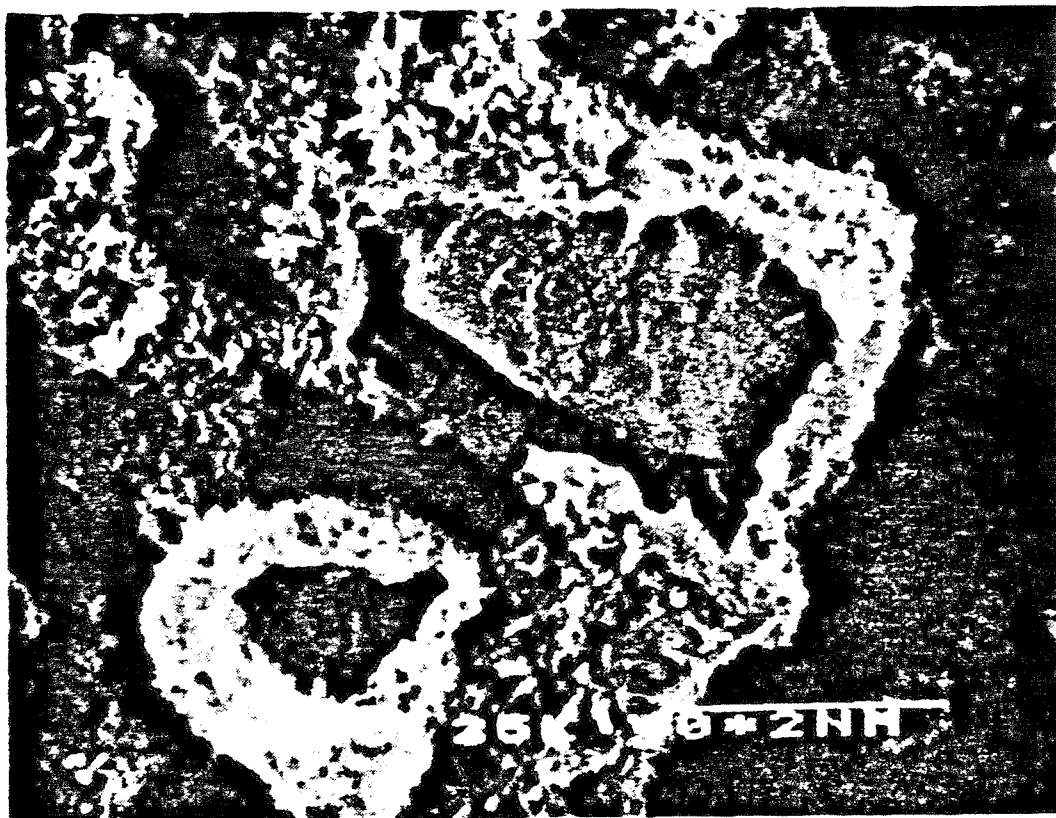


Fig. 17 Hadley's grain.
313

mechanism. These grains were originally reported by Hadley (3.4) while describing the morphology of the interface; later on Barnes et al (3.11) showed that the presence of such grains in the bulk paste. One may argue that the fracture and the subsequent drying of the matrix for SEM analysis can be responsible for originating the morphology of these grains. So far this is an open question and research using the low-temperature electron microscope (Chapter 2) which avoid drying the paste may provide useful information.

The morphological features are the same as described by Hadley (3.4) and Barnes (3.5) who based most of their studies on the glass slide-cement paste interface, since quartz is an inert aggregate and therefore the morphology of the interface is mainly controlled by the geometrical constraints that the aggregate face produce on the kinetics of the hydrating cement paste.

3.3.1 Formation of Calcium Hydroxide over the Interface

Being in direct contact with the aggregate face, the calcium hydroxide form almost a continuous film with c-axes normal to the interface. This phenomenon was observed by many researchers, among them: Schwiete et al. (3.12), Bertacchi (3.13), Buck and Dolch (3.14), Hadley (3.4), Barnes (3.5), Ollivier (3.15). However, there is no agreement on how this film will affect the mechanical properties of the interface. In this section, only the morphology of the CH film will be discussed; the research and analysis of the mechanical properties of the film will be delayed to chapter 4.

Fig 3.14 shows a secondary calcium hydroxide crystal parallel to the aggregate face. the crystal seems to be in contact with the CSH film. In the same micrograph many hydrating cement grains that attached to the CSH layer can be observed.

Ollivier (3.15) developed a procedure to determine the distance from the interface where the calcium hydroxide starts to grow in a random manner. This distance can give some information on the extension of the transition phase. In this study it is

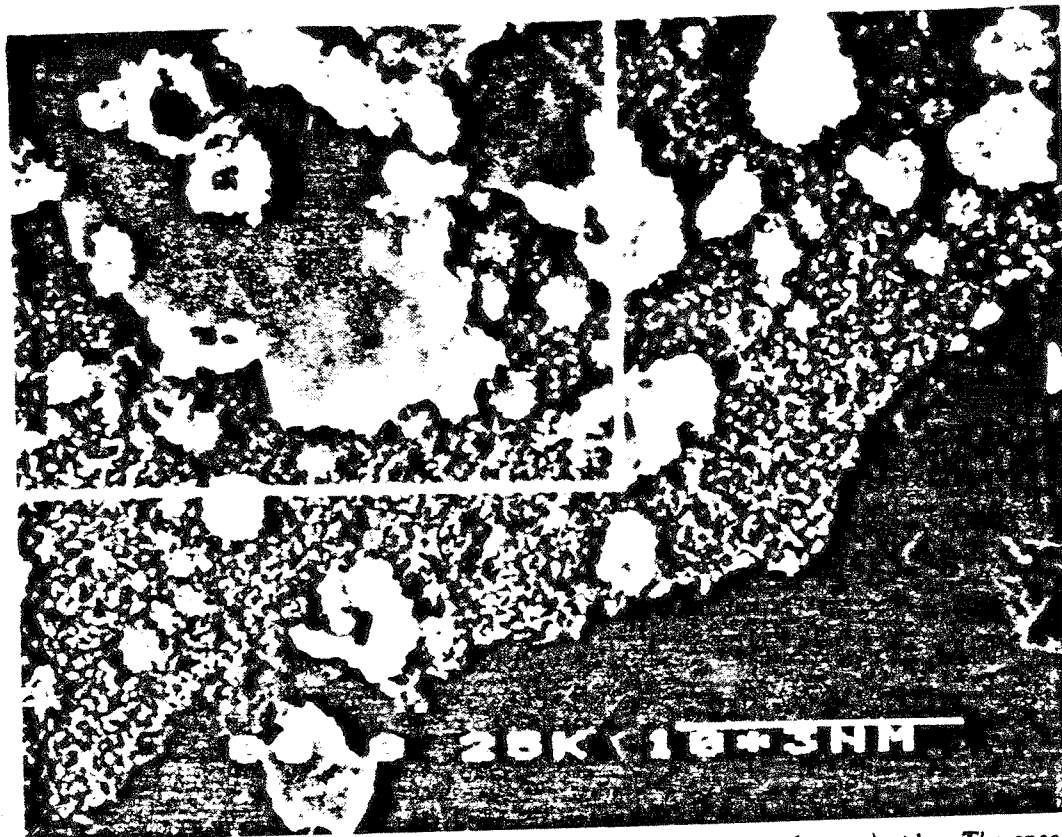
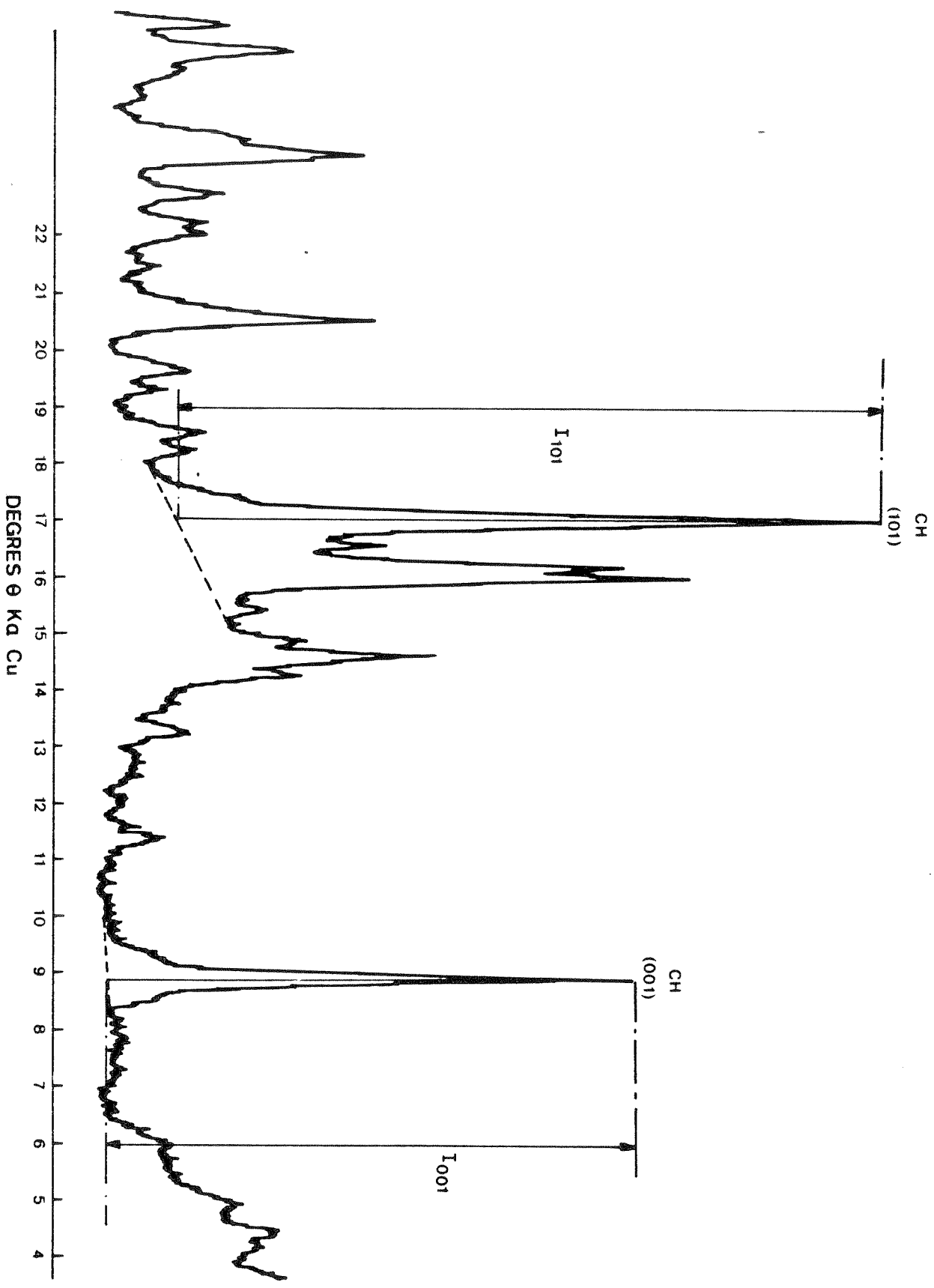


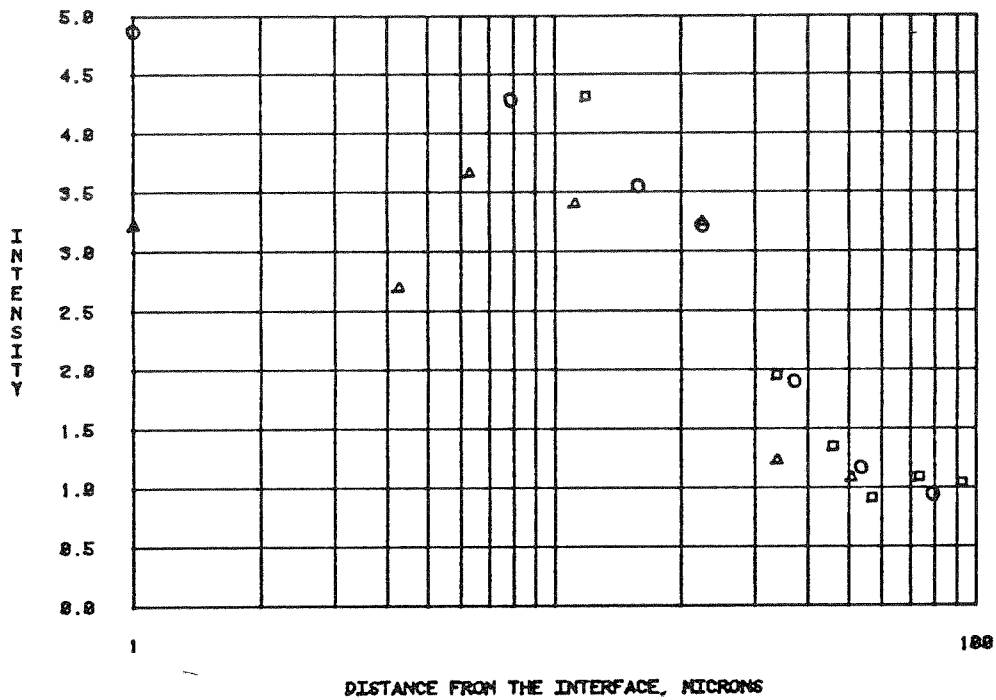
Fig. 1 Shows the interface morphology over the aggregate (quartz) side. The specimen was 1 day old. 3.94

Fig. 3. 15

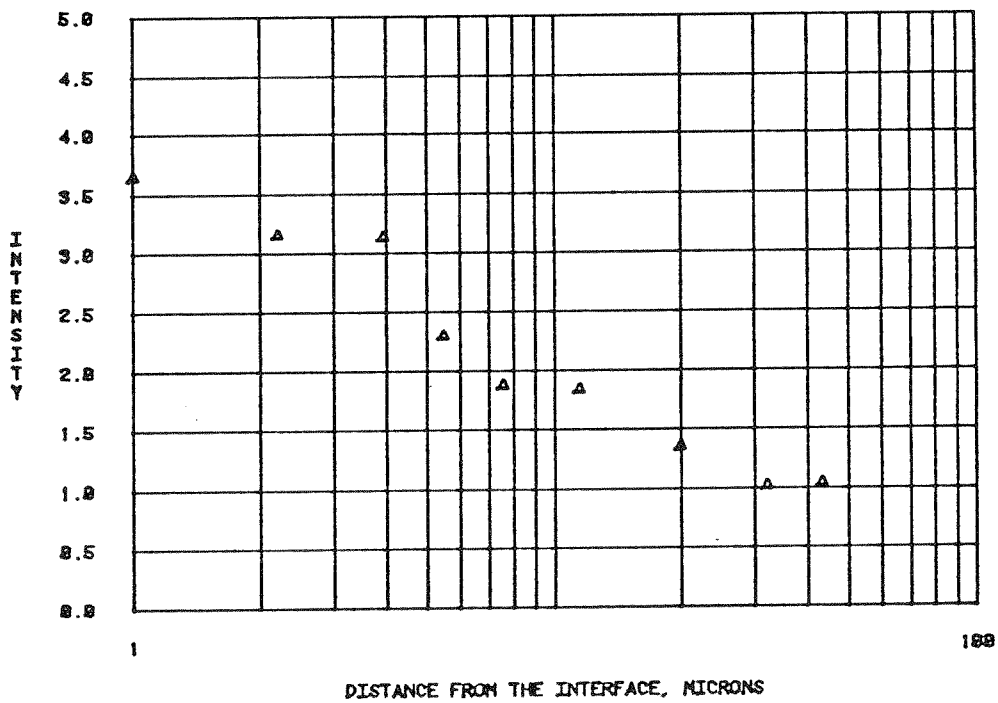
Fig. 3 Measure of the Peaks Intensity



CH Preferential Orientation ^{3.16} **Fig. 12A** *Reaction Zone*
CALCIUM HYDROXIDE PREFERENTIAL ORIENTATION -1 DAY

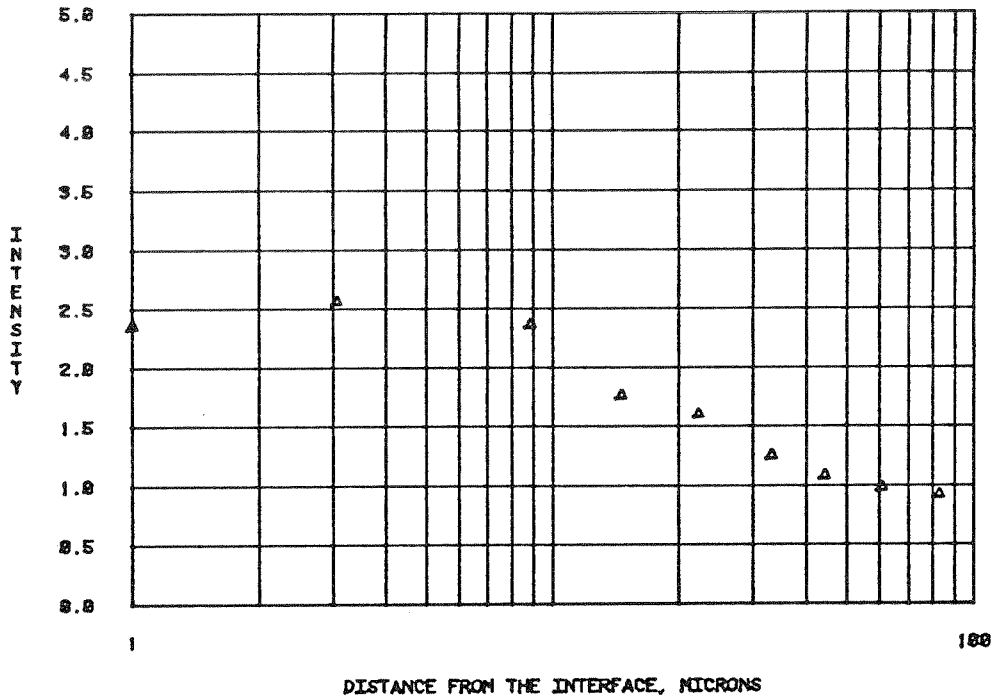


CALCIUM HYDROXIDE PREFERENTIAL ORIENTATION -3 DAYS

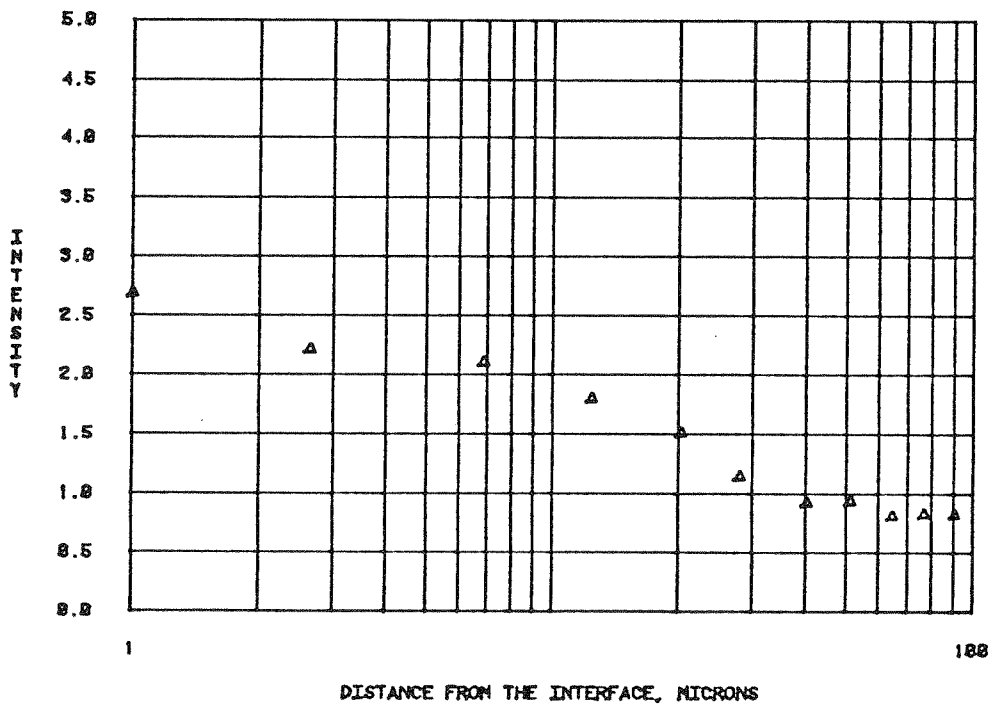


16
Fig. 12B

CALCIUM HYDROXIDE PREFERENTIAL ORIENTATION -30 DAYS



CALCIUM HYDROXIDE PREFERENTIAL ORIENTATION -60 DAYS



convenient to define an index of preferential orientation. Since the crystals tend to grow parallel to the aggregate face the (001) is a natural plane to select. The other plane chosen is (101) because there is not much interference with peaks of other hydration products.

$$R = \frac{I(001)}{I(101)}$$

The ratio R is 0.74 for random orientation of the calcium hydroxide. Therefore if we want to know how much the orientation deviates from the random one, the ratio I is defined as:

$$I = \frac{R}{0.74}$$

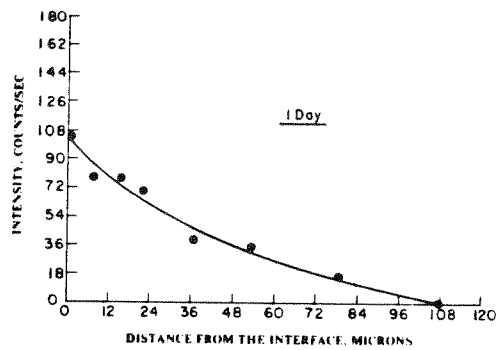
In this case I is 1 for a random orientation and approaches infinity for a perfect orientation (c-axis).

This is shown on the XRD chart of Fig. 3.15. As demonstrated in Fig 3.16, with increasing distance from the aggregate face the degree of preferential orientation decreases up to a point where random orientation of the crystals is achieved. In this figure the change in preferential orientation for various ages is also shown.

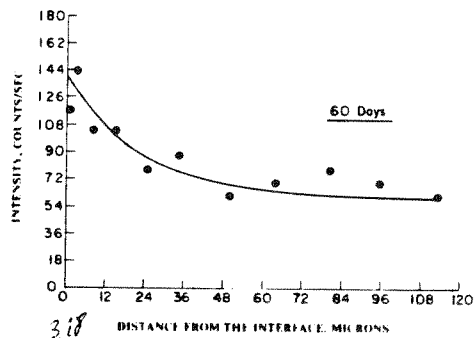
3.3.2 Etringite Formation on the Interface

As discussed in section 2.1, two theories are generally advanced to explain the mechanism of cement hydration. According to the "through-solution" theory the cement compounds dissolve to produce ions in solution that will recombine to form hydration products which subsequently precipitate out from supersaturated solutions. On the other hand, the "topochemical" or "solid-state" theory suggests that the reactions take place without the cement compounds going into solution.

Schwiete et al. (3.16) studied the $C_3A - \bar{C}\bar{S} - CH$ system by transmission electron microscopy and concluded that ettringite is formed topochemically on the C_3A surface. The topochemical theory is also supported by Bentur and Ish-Shalon (3.17-3.19), and



317
 FIG 7 VARIATION IN THE ETTRINGITE
 CONCENTRATION IN THE INTERFACIAL ZONE



318
 FIG 8 VARIATION IN THE ETTRINGITE
 CONCENTRATION IN THE INTERFACIAL ZONE

Hansen (3.20). On the other hand, Chatterji (3.21,3.22), and Mehta (3.23), after studying the morphology of ettringite by scanning electron microscopy concluded that ettringite is formed by a through-solution mechanism.

The investigations cited above were carried out with pastes; this section reports of the ettringite distribution over the interface. Concentrations of different hydration products with respect to their distance from the aggregate surface were determined at regular intervals from 1-day to over a year. Here, the results for ettringite concentration alone are shown for 1 and 60-days age (Figs. 3.17 and 3.18). It should be noted that the ettringite peak at $9.1^\circ 2\theta$ ($Cu-K\alpha$) is not subject to preferred orientation, therefore the intensity of this peak is directly proportional to ettringite concentration.

From the distribution of ettringite in the interfacial zone at both ages, it is evident that much larger quantities of ettringite are present immediately next to the aggregate surface than farther away from it. This can only be explained by the "through-solution" mechanism according to which the calcium, sulfate, and aluminate ions quickly migrate to the water film at the aggregate surface and, therefore, more ettringite gets precipitated there.

3.3.3 Effect of Silica Fume

The use of silica fume in fresh concrete introduces a series of beneficial effects: increases cohesion, reduces bleeding and segregation. Some of these parameters have a major influence in the development of the transition zone microstructure. In this section, two levels of silica fume are used, 5% and 16%. The first level was used because it was the maximum amount of silica fume that could be replaced and produce a workable paste of 0.35 w/c. The second level was selected because it represents a common amount used in high-strength concrete and in order to produce a workable mix, 1% of lignosulfonate was used.

It should be remembered that silica fume has an average particle size of less than

1/100 of that the cement paste so its introduction in the matrix will affect the physical arrangement of the system and in particular near the aggregate surface where a higher porosity exists. Also the pozzolanic nature of the silica fume is well reported and it will influence the microstructure of the transition zone, specially when one considers that in this region there is a concentration of calcium hydroxide near the aggregate surface.

It is an interesting fact that the formation of large crystals of calcium hydroxide with a preferential orientation on the interface happened for both levels of silica fume and for all ages. Fig. 3.19 shows some particles of silica fume over the aggregate surface. It is surprising to find them after 1 month of casting, because they were supposed to have been dissolved at early ages. One possible explanation is that because of the high amount of microsilica replacement (16%), the equilibrium solution would require that some of the particles to be only partially dissolved. The white box zone is amplified five times in Fig. 3.20 and we can see that the silica fume particles with approximately $0.4 \mu\text{m}$ of diameter are partially dissolved on the aggregate face.

The observed effect of silica on the transition zone may be explained by the following mechanism:

1. Less accumulation of free water at the interface.
2. Nucleation sites preventing a preferential orientation.
3. Pozzolanic reaction reducing the CH on the interface.

It should be also mentioned that for the cement paste with 5% silica fume no superplasticizers or retarders were used and there was some premature stiffening, because, as Grutzeck et al. (3.24) pointed out, a gels forms during the first minutes of mixing and it can take up water and stiffen the mix. This process also decreases the easy diffusion of Ca^{2+} ions towards the aggregate surface.

In section 6.2, a complete series of CH preferential orientation and ettringite dis-

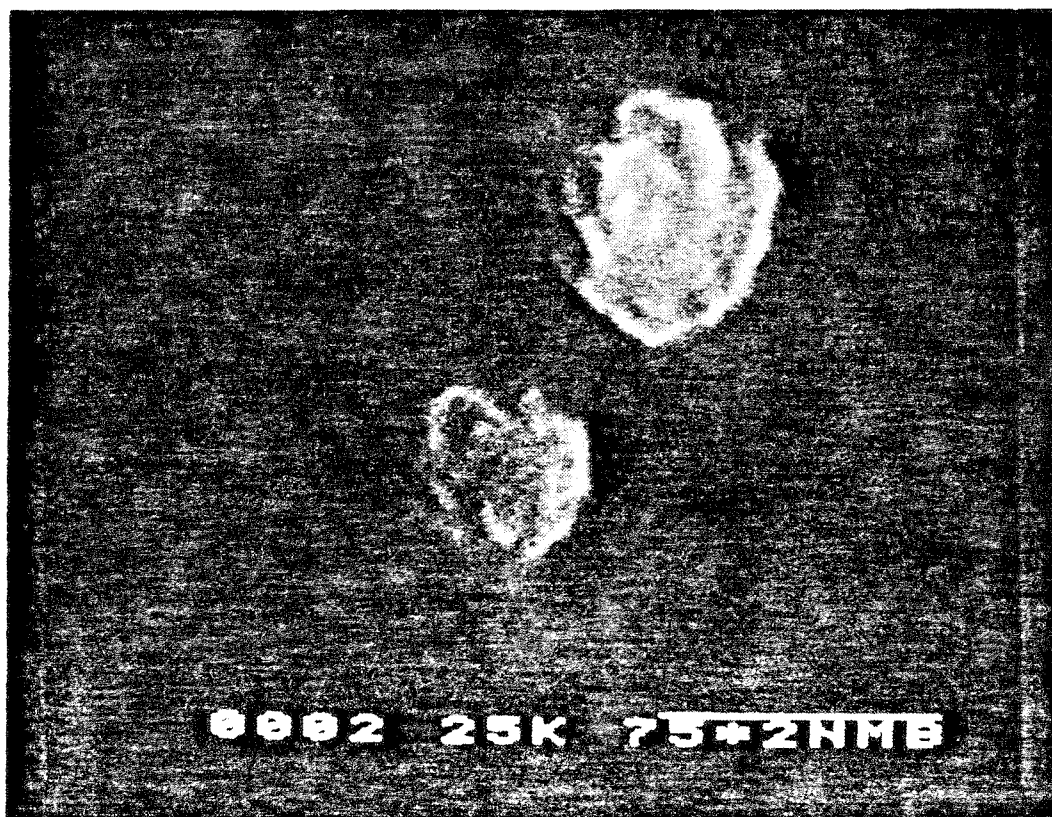
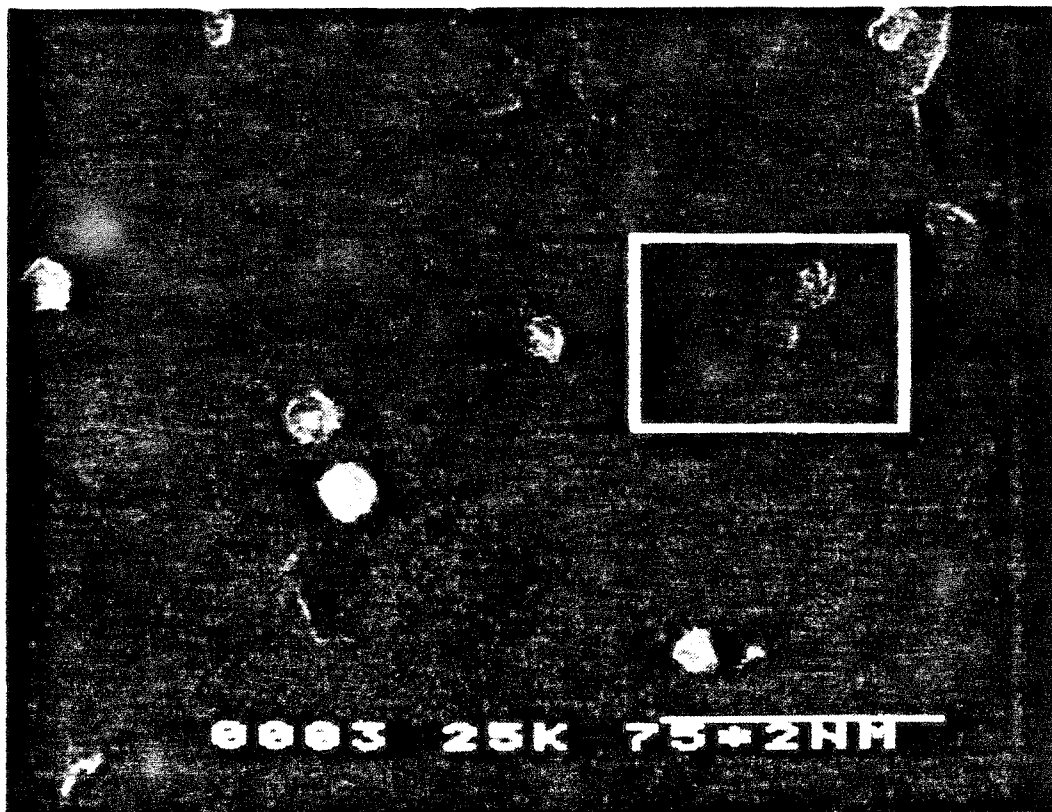


Fig. 17³¹⁹ Shows the distribution of silica fume near the aggregate. The white box is amplified in Fig. 18³¹⁹ (20,000 X) and we can see that the particles are partially dissolved. The specimen was 30 days old and a replacement of 16% of microsilica was used.

tribution in the transition zone over a period of one year is reported for various level of silica fume replacement. So the complete discussion of the effect of silica fume will be delayed to that section.

3.3.4 The Expansive Cement Paste-Quartz Interface

Expansive cement has the attractive potential of putting concrete in compression if adequate restraint is provided and therefore this may compensate the the tensile stresses produced by shrinkage or may leave the concrete in a self-stressing state, depending on the magnitude of the expansion.

Even though many reactions can produce expansion of the hardened cement paste, three reactions have received most of the attention: hydration of CaO to $Ca(OH)_2$, hydration of MgO to brucite and the development of calcium sulfoaluminates hydrates. This research was focused on the later reaction and more particularly to the one produced by the use of the type K-cement.

Many theories have been proposed to explain the expansion. Chatterji and Jeffery (3.25) suggested that it was due to the formation of the monosulfate hydrate, however the new tendency is to attribute the expansion to the ettringite formation. Nevertheless, the precise mechanism is not yet fully understood. Two main theories are available: swelling theory and the crystal growth theory. The first theory suggests that due to the high surface area and negative surface charge the ettringite imbibe large amount of oriented water and swell by interparticle repulsion. This view is supported by Mehta (3.26,3.27), Mehta and Hu (3.28) and by Sivertzev as quoted by Mikhailow (3.29). The crystal growth theory proposes that expansion is due to the ettringite crystal growth which originates crystallization pressure and consequently expansive force (3.17,3.18).

The size of ettringite crystals depend on the composition of the liquid phase. In the presence of high concentrations of calcium sulfate and calcium hydroxide, the crystals are submicroscopic. When the concentrations of the two compounds decrease

needle-like crystals are formed. For the hydrated expansive cement composition, Mehta (3.30) reported short prismatic ettringite crystals of about $1/4\mu m$ and 1μ length.

It is a documented fact that compressive strengths of shrinkage-compensating concretes are often higher than those of portland cement concretes. Polivka and Willson (3.31) reported that concretes with a w/c ratio lower than 0.65 the strength was higher when a Type K expansive cement was used instead of Type I portland cement. Hoff and Mather (3.32) confirmed this tendency by comparing the results of expansive cement (Type K) concrete with those of Type II portland concrete. Once the aggregate-cement paste is the weak zone in concrete, this strength improvement may be due to a modification of the interface when expansive cement is used. To clarify this matter, this research will analyze the interface between an expansive cement and quartz aggregate.

An expansive cement, type K, obtained from a mixture of alite (5600 g), $C_4A_3\bar{S}$ (400 g), $C\bar{S}$ (720 g) and CH (280 g) was used. The cement paste (0.40 w/c) was cast on top of a polished surface of a rock, forming a composite specimen. The vertical expansion of the cement paste (for the expansive cement) was restrained by applying a force on top of the specimen. The specimens were stored in a fog room at 20 C. At specified ages, the composite specimen was broken at the rock-cement paste interface. Both the cement paste and the rock were analyzed by scanning electron microscope (SEM) and X-ray diffraction analysis (XRD). When expansive cement is used, the formation of a continuous film is eliminated by the precipitation of CH crystals with a random orientation on the interface. This phenomenon is demonstrated in the low magnification micrographs of the interface (cement paste side) shown in Figs. 3.20 and 3.21.

The differences between the interface using expansive and portland cement are shown in Figs. 3.22 and 3.23. For portland cement, large CH crystals with a preferential orientation and no indication of individual crystal boundary form a continuous film

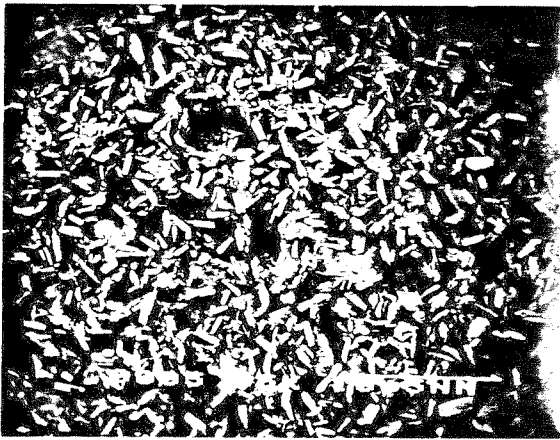


Fig 3 20
General view of the Transition
Zone when Eapenac cement is
Used

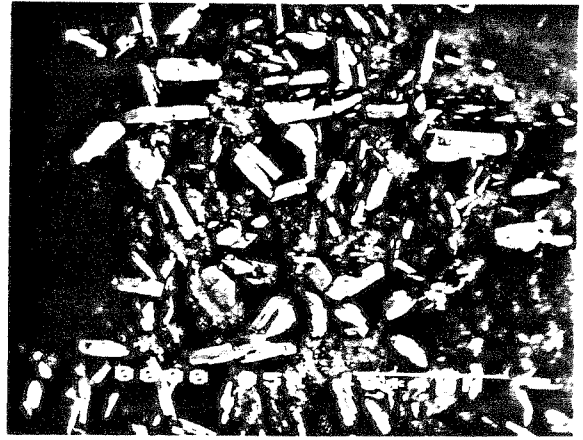


Fig 3 21
Detail of Fig 3 20



Fig 3 22
Transition zone when Portland cement
is used



Fig 3 23
Transition zone when Eapenac
Cement is used.



Fig 3 24
C4 crystals on the Transition Zone

in direct contact with the aggregate surface; while for expansive cement large CH crystals ($100\mu m$) are precipitated with a random orientation on the top of the CH film. A detail of the interface with expansive cement is shown in Fig. 3.24, where the dense formation of CH crystals on top of the CH film can be seen.

Some unique points should be discussed at this stage. First, it seems that the calcium hydroxide film was not in direct contact with the aggregate and second that the ettringite formation is able to cause CH crystals to be formed in a random way in the interface. For this to happen, it is reasonable to expect that ettringite was the first hydration product to be formed and that it is precipitated directly on the aggregate surface. These assumptions are confirmed with the micrographs shown in Figs. 3.25 and 3.26 where a bunch of ettringite is formed on top of the CH film and the ettringite crystals are surrounded by CH crystals with a random orientation.

An analysis of the aggregate side can be made to verify the above assumptions. A general view of the interface on the aggregate side shown in Fig. 3.27, where ettringite crystals either in distinct crystals or together in bunches are in direct contact with the aggregate surface. Figs. 3.28^a and 3.29^b show details of the ettringite formed in direct contact with the interface.

Even though the formation of a continuous CH film was avoided with expansive cement, some smaller CH crystals are still formed in a preferential way as shown in Figs. 3.20, 3.21 and 3.24. To study the preferential orientation of the CH crystal by XRD over the interfacial zone, let us use again the index of preferential orientation as the ratio of the $I_{(00.1)}$ and the $I_{(10.1)}$ intensity peaks. This ratio is normalized by dividing by 0.74 to give the value 1 for random orientation and infinity for perfect orientation (c-axis). Fig. 3.30 shows the distribution of the CH preferential orientation over the interfacial zone for the expansive cement.

The determination of the ettringite concentration over the interfacial zone was done by selecting the peak at $9.1^\circ 2\theta$ ($Cu-K\alpha$) because it is not subjected to

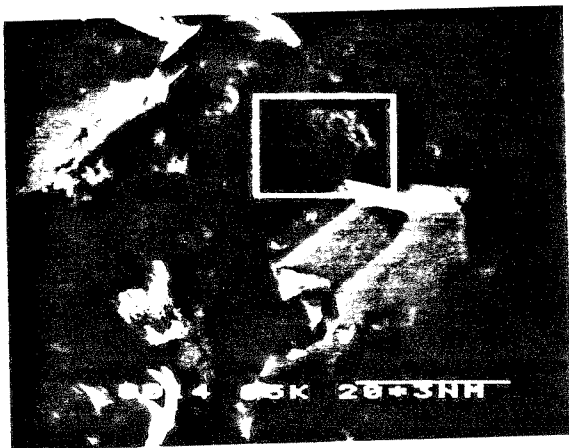


Fig 3.25
 General View of the Transition zone
 (Cement Paste Side)



Fig 3.26
 Detail of Fig 3.25 Showing Elongate
 on Top of the CH Film



Fig 3.27
 General View of the Transition zone
 (Aggregate Side)

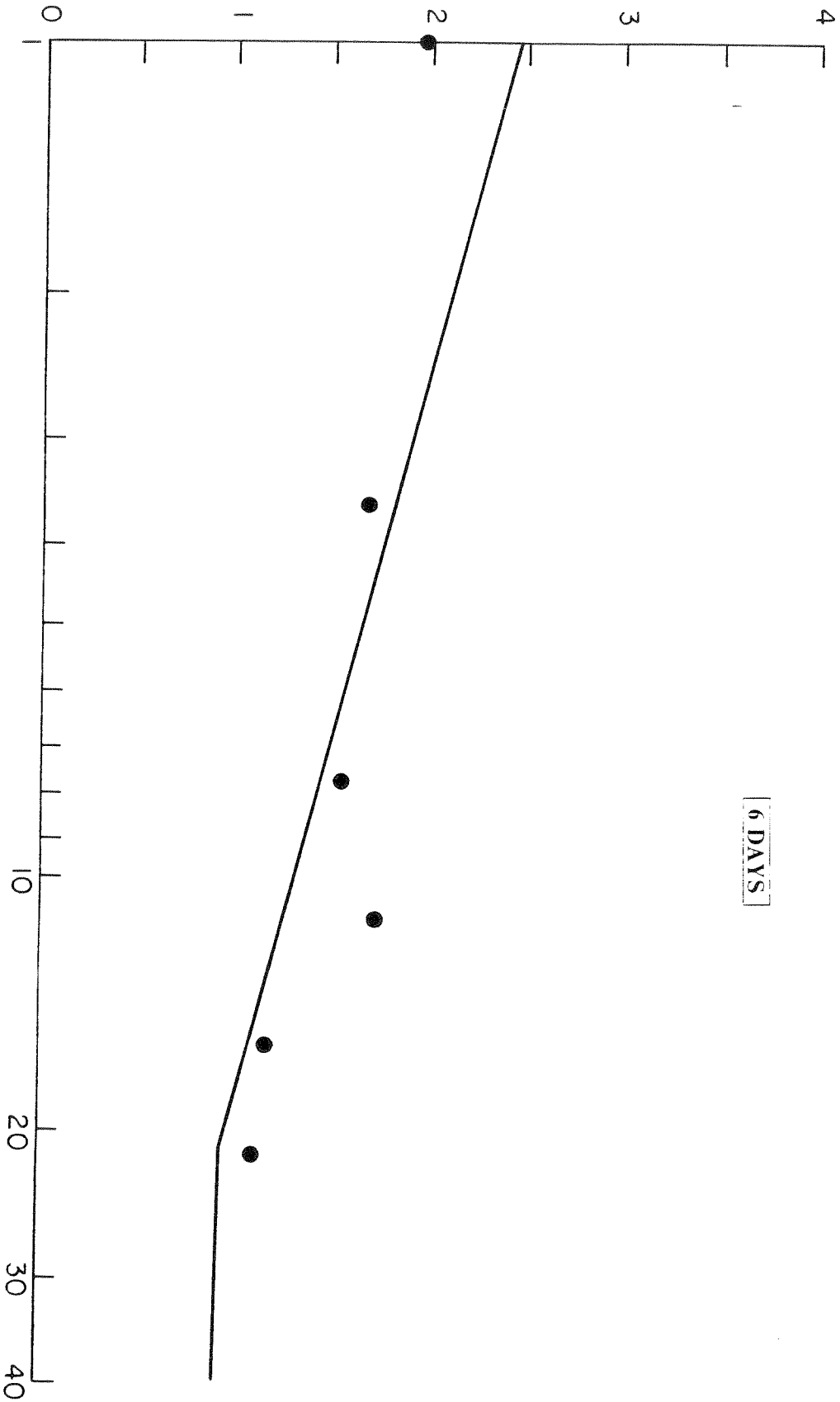


Fig 3.28A
 Detail of Fig 3.27



Fig 3.29
 Detail of Fig 3.27

INTENSITY OF THE ORIENTATION



Variation In The Calcium Hydroxide Preferential Orientation Index In The Transition Zone
When Expansive Cement Is Used.

Fig 3 30

preferential orientation and is not interfered by other peaks. Fig. 3.31 shows that there is a great concentration of ettringite near the aggregate surface; this observation supports the through-solution mechanism of cement hydration as discussed in section 3.3.2.

In summary, for the expansive cement, the precipitation of ettringite either in individual crystals or in bunches over the aggregate surface prevents the formation of a continuous CH film there. Smaller CH crystals still are precipitated with a preferential orientation, however the deposition of CH crystals with a random orientation on top of them probably reduces the facility of crack to propagate in this zone. Both the concentration of ettringite and the CH crystal refinement on the interface may explain the reported higher mechanical strength when expansive cement is used instead of portland cement Type I.

3.4 Carbonate-Cement Paste Interface

The carbonate-cement paste interface has been fascinating researchers ever since Farran (3.1) in 1956 pointed out a reaction between this aggregate and the cement paste. He reported an extensive aggregate-cement paste interface research and concerning the carbonate rocks, some of his findings were:

1. The bond of calcite or dolomite to cement paste was better than that of other minerals.
2. A "corrosion" of calcite surfaces in contact with cement paste was observed.
3. No epitactic bond between CH precipitated from the paste and aggregates other than calcite was observed.

Buck and Dolch (3.14) reported that limestone aggregates reacted with concrete, and these aggregates had thin, dark bands just within the surface. The limestone had low absorption, low acid-insoluble residue and contained little or no dolomite; therefore, a dedolomitization was ruled out. In their tests, the reaction occurred both with

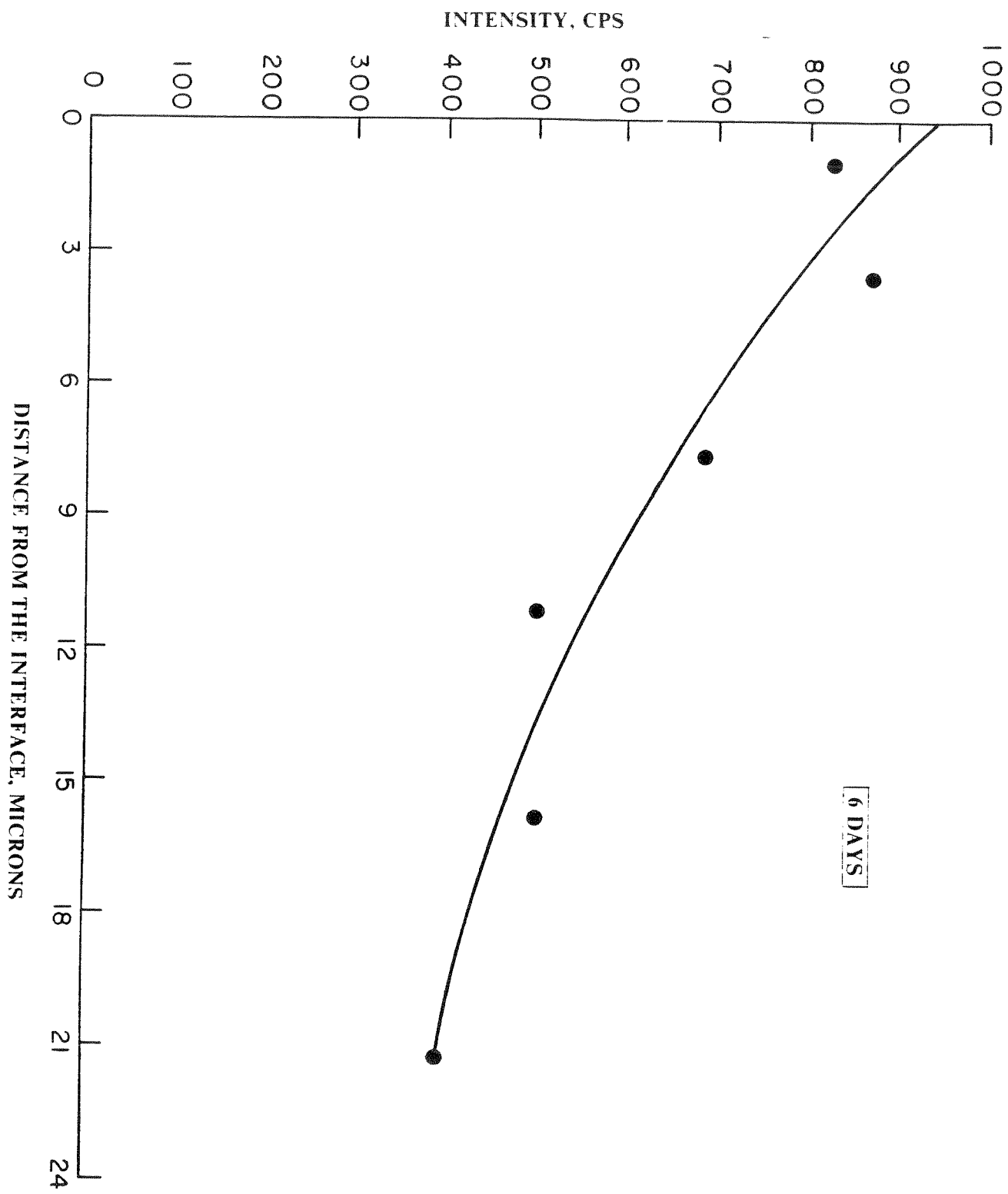


FIG. 2. 31

Variation Of Etringite Concentration In The Transition Zone When Expansive Cement Is Used

high or low-alkali cement, however the reaction was more apparent in mixtures made with low-alkali cement at 30-40 days; also no acid-insoluble material was formed in the rock by the reaction. They suggested that alkalis are probably required for the reaction to occur because there was no reaction in a paste of tricalcium silicate. The intensity of the 3.04 Å calcite peak was always less at the surface of the reacted rock after the reaction had occurred. The conclusion of their work was that a reaction between the limestone and the alkaline solutions of the portland cement takes place at the interface with some calcite reacting and small amount of highly oriented calcium hydroxide is formed in its place.

Chatterji and Jeffery (3.33) reported similar etching of grains of limestone in their aggregate-cement paste interface research.

The other possibility of reaction on the concrete cement-paste interface when calcite is present is the formation of a carboaluminate. Lyubimova and Pinus (3.34) Schwiete et al. originally postulated this reaction. Later on Cussino and Pintor (3.35) Cussino et al. showed a reaction between calcite, C_3A , or C_4AF and water to produce $C_3A.CaCO_3.11H_2O$. More recently, Grandet and Ollivier (3.37) reported the formation of $C_3A.CaCO_3.11H_2O$ by the reaction between $C_3A.1/2CO_2.12H_2O$ and carbonate ions produced by dissolution of calcium carbonate. They also showed the "corrosion" of the calcite surface in contact with cement paste.

Hadley (3.4) did not attribute any special strong bond between the calcite and the paste. He suggested that the tendency of calcite to fracture through the mineral rather at the interface was due to the well developed planes of the calcite and he reported the same behavior for other minerals such as dolomite, siderite, muscovite, biotite, phlogopite, fluorite and galena.

In summary, most researchers agree that the carbonate aggregates are not inert once they react with the hydration products in the transition zone. This chemical interaction produces a better bond that improves the mechanical properties of

concrete. From this point on, the theories depart and none of them can fully describe the mechanism. In this section, two carbonate rocks, a marble and a limestone with the properties presented in section 3.2 were polished down to 0.25 microns. Most of the work, however, was concentrated in the marble and Fig 3.32 shows a micrograph of its crystal structure.

The early development of the transition zone follows the results presented in section 3.3, and a typical interfacial zone is shown in Fig. 3.33, where the CH film with a preferential orientation can be seen. At later ages manifestations of the development of a chemical bond between the aggregate and the matrix can be felt. For instance, in many portions of the CH film, calcite crystals that adhere to the film can be observed as shown in Fig. 3.34. That may be attributed either to a better bond or to the weak calcite cleavage planes. However, Figs. 3.35 and 3.36 show that during fracture, the first layer of the CH film adhered to the calcite, a fact not seen by the author for any of the rock type studied in this Thesis. This strongly suggests that the contact between the CH film and the calcite developed a better bond.

On the aggregate side, the etching of the calcite can be observed as shown in Fig. 3.37. The imprint of this etching can be seen on top of the CH film in Figs. 3.38 and 3.39.

These micrographs show without question that there is a chemical reaction between the carbonate rock and the matrix. Now, concerning the mechanism, the micrographs tend to show that the reaction is particularly intense in the direct contact between the aggregate and the CH film and no particular reaction between the calcite and the aluminates was observed by SEM. However to avoid making hasty conclusions, particularly due to the rather localized nature of the SEM analysis, a detailed XRD analysis of the transition zone from 1 day to over a year was performed. A typical XRD analysis of the interface is presented in Fig. 3.40. It should be noted the peak at $11.2^\circ 2\theta$ ($Cu-K\alpha$) Grandet and Ollivier (3.37) obtained a peak at $11.6^\circ 2\theta$ (

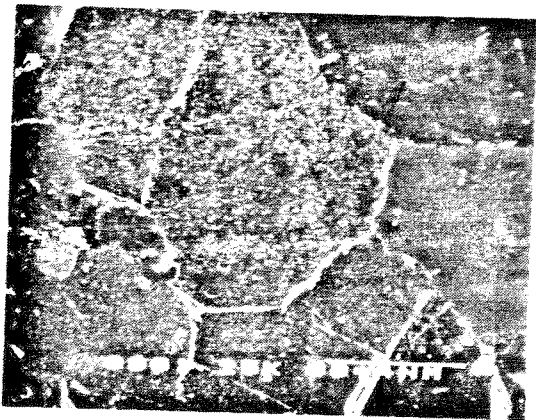


Fig 3.32
Detail of the marble crystal structure

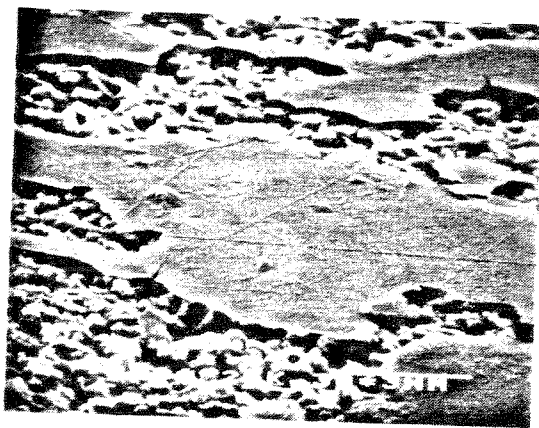


Fig 3.33
General view of the transition zone

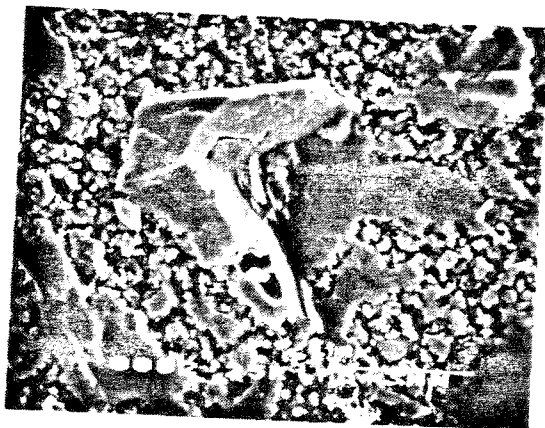


Fig 3.34
Calcite grain adhering to the CH film

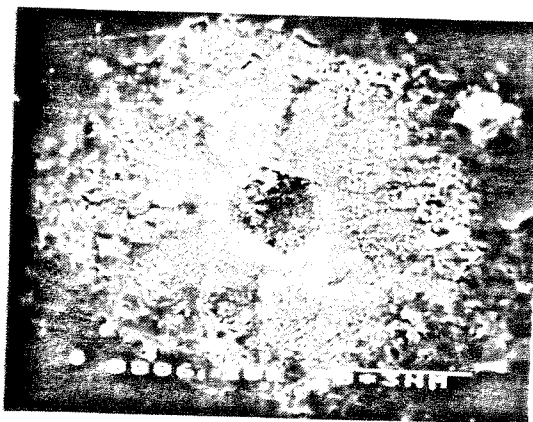


Fig 3.35
Evidence of a Bath Band when carbonate rock is used. The dark zone is the CH film



Fig 3.36
Removal of the contact film during extraction. The dark zone is the CH film

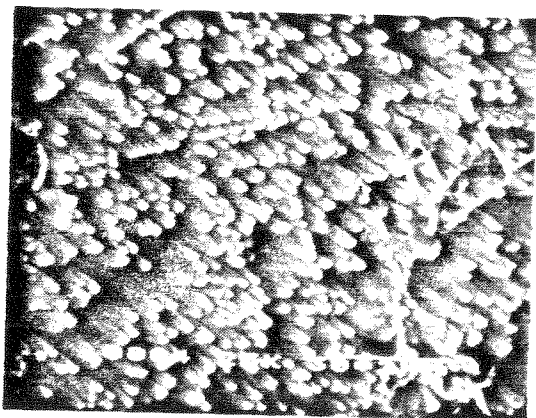


Fig 3.37
Etching of the calcite

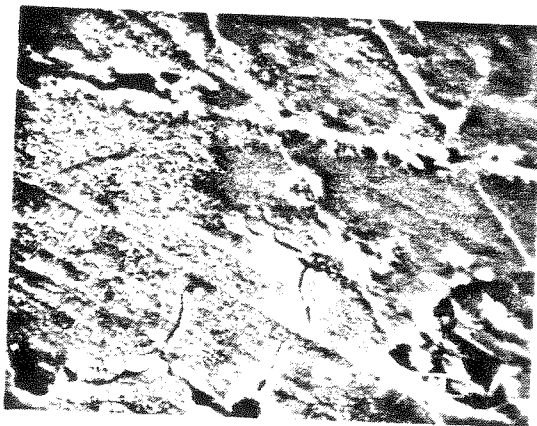


Fig 3.38
Imprint of the calcite Etching on
the CH Film

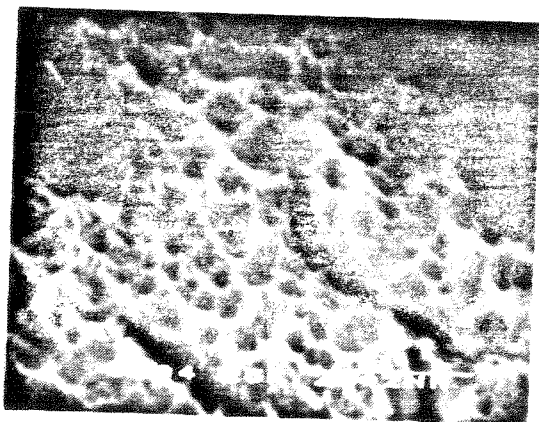
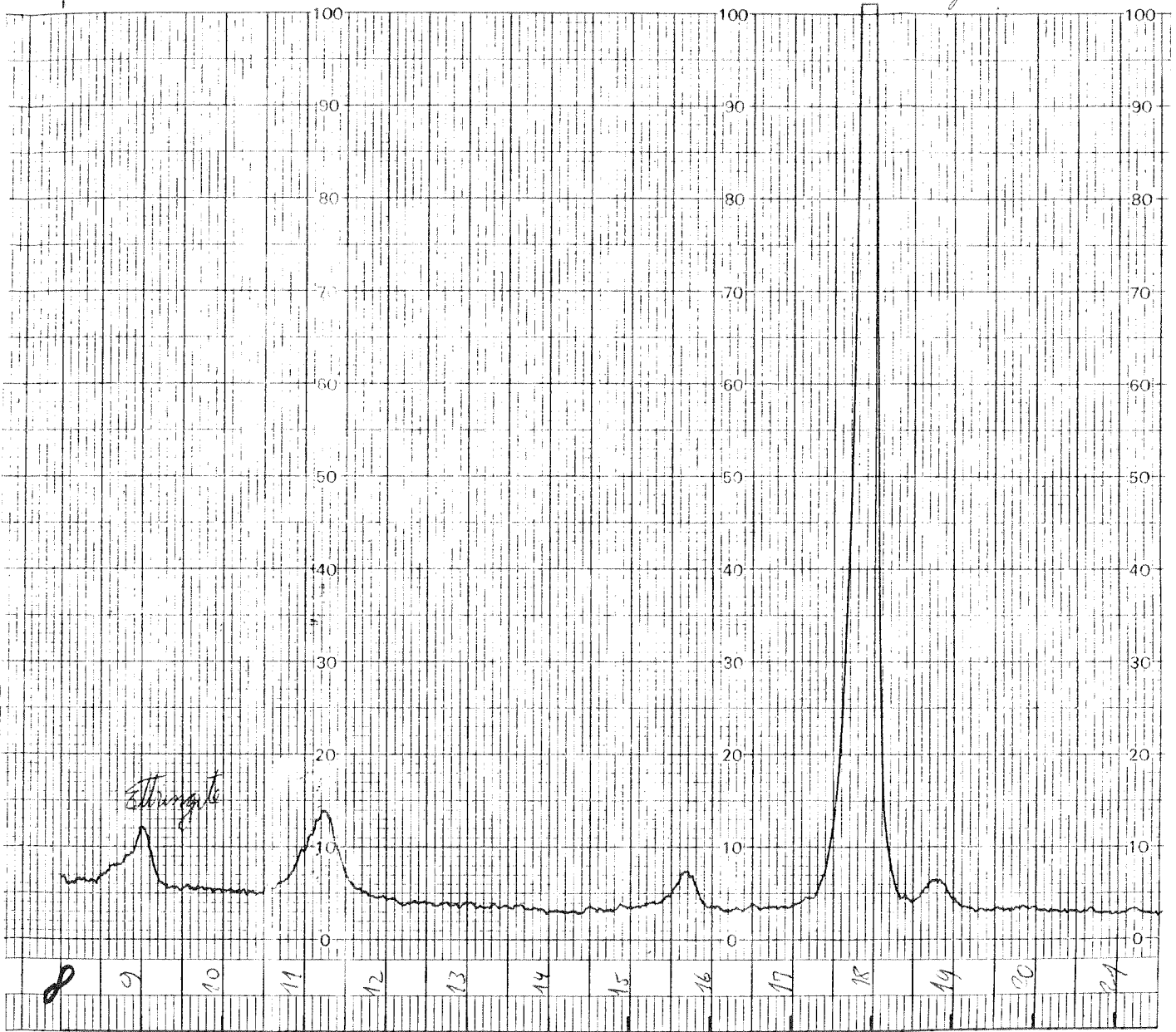


Fig 3.39
Detail of Fig 3.38

Whium Hydrate



XRD Analysis of the ^{Fig 3.40} Interface, showing a peak at 17.8° 2θ (Cu-Kα)

$Cu-K\alpha$) and proposed that was due the formation of calcium hydrocarboaluminate. In this work, however, this peak was around $11.1^\circ 2\theta$ ($Cu-K\alpha$) for all ages, also it should be mentioned that in no case the peak referred to the $C_4A \cdot \frac{1}{2}CO_2 \cdot 12H_2O$ was obtained.

Since now the major issue is related to the effect (or the lack of it) of aluminates specially C_3A , it was decided to study the transition zone between alite and marble. The chemical analysis of the alite is shown in table 3.2, the aluminates are present as a minor compound and XRD analysis showed no trace of C_3A or C_4AF .

The first question to address is to check if the same reaction reported for portland cement develops when alite is used. The micrograph shown in Fig. 3.41 demonstrates that the calcite etches in the same way when alite is used. On the CH film the imprint of a reaction with a calcite crystal can be seen on Fig. 3.42 and a magnification of this zone showing the presence of smaller crystals precipitated on top of the film is shown in Fig. 3.43.

Of particular interest are the series of micrographs presented in Fig. 3.44. The lower magnification micrograph (Fig. 3.44) shows in the left hand side the imprint of the calcite decomposition and on the right hand side the precipitation of smaller crystals which were formed after a reaction with the film. EDAX analysis was performed on the site of the calcite decomposition and crystal precipitation of the micrograph in Fig. 3.45 and no trace of Al was found. Likewise, EDAX analysis was performed on the zones shown in Fig. 3.46.

This analysis seems to rule out the importance of carboaluminates in the transition zone. Nevertheless, an extensive XRD analysis was performed on the transition zone from 1 day to 220 days. A typical XRD diagram is shown in Fig. 3.47. It is important to note the presence of the same peak at $11.1^\circ 2\theta$ ($Cu-K\alpha$) as when portland cement is used; therefore the traditional explanation of being a calcium hydrocarboaluminate is not satisfactory since there was no C_3A and so the peak obtained by



Fig 3.45
 General view of the transition zone
 showing the Reaction in the CH Elm.
 EDAX shows no trace of Al.

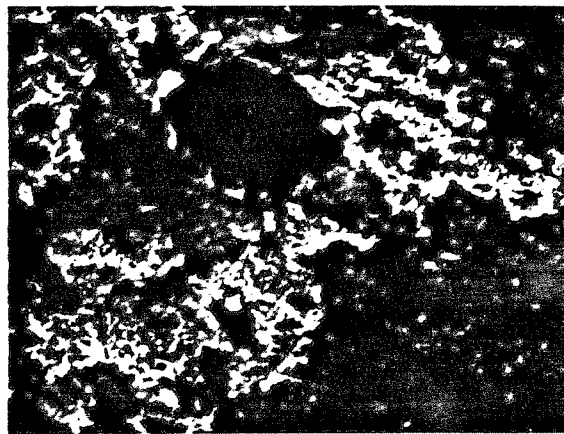


Fig 3.46
 EDAX Analysis

Element & Line	Area A Weight Percent	Atomic Percent	Precision 2 Sigma	K-Ratio
Mg KA	9.14	12.68	2.07	0.0468
Al KA	3.23	4.04	1.35	0.0175
Si KA	26.55	31.88	1.91	0.1720
CA KA	61.09	51.39	2.20	0.5516

Element & Line	Area B Weight Percent	Atomic Percent	Precision 2 Sigma	K-Ratio
Mg KA	7.27	10.29	0.63	0.0364
Al KA	2.08	2.65	0.09	0.0114
Si KA	25.41	31.10	0.56	0.1693
CA KA	65.24	55.96	0.65	0.5945

Cussino and Pintor (3.35) using a mixture of calcite and C_3A does not apply. Now it is necessary to identify the precipitated crystals on the CH film. From what was discussed it is natural to expect that the reaction involves the calcite and the CH film. It is a well known fact that Mg forms the compounds $Mg_4(OH)_2CO_3 \cdot 3H_2O$ and $Mg_2(OH)_2CO_2 \cdot 3H_2O$ but the corresponding Ca compounds were difficult to find because of experimental difficulties until Schimmel (3.38,3.39) was able to prove the existence of a basic calcium carbonate with 1.5 molecules of crystallized water, $Ca_3(OH)_2(CO_3)_2 \cdot 1.5H_2O$. His work showed that the X-ray pattern is extremely sensitive to the amount of crystallized water. It should be mentioned however that when the crystallized water is evaporated the second highest peak is $11.4^\circ 2\theta$ ($Cu-K\alpha$) which is very close to the one obtained in this research. The differences in XRD diffraction can be attributed to different amounts of crystallized water. Therefore it is proposed that the crystal development from the dissolution of calcite and reprecipitated in the interfacial film is a basic calcium carbonate with a variable content of crystallized water, $Ca_3(OH)_2(CO_3)_2 \cdot xH_2O$.

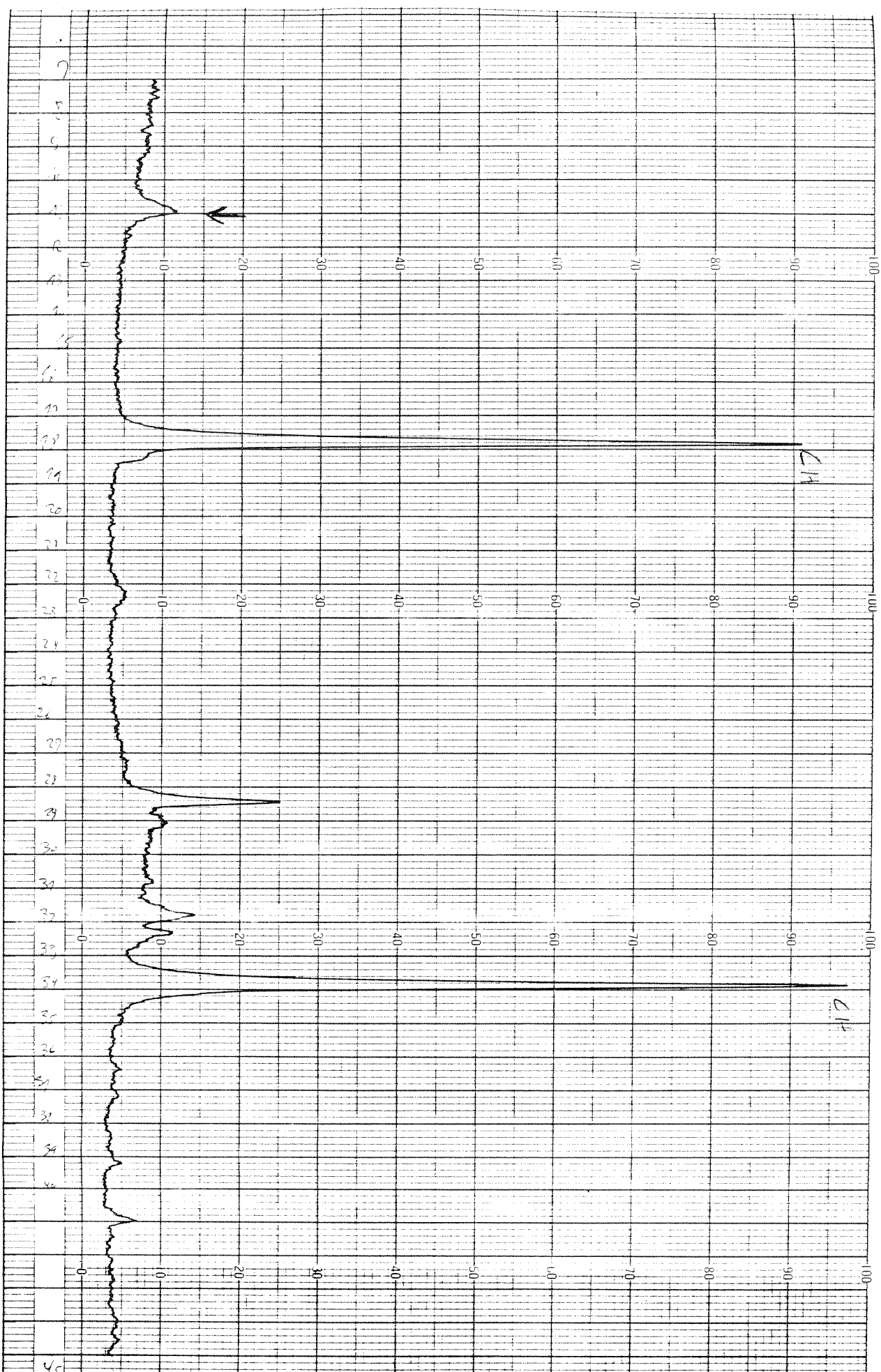
It is interesting to determine how far this reaction extends from the aggregate surface. This can be determined by the method of successive abrasion of the interface. Fig 3.48^{*} shows the distribution of $Ca_3(OH)_2(CO_3)_2 \cdot xH_2O$ over the transition zone.

3.5 The Mortar-Aggregate Interface

In the previous sections, the transition zone was studied for pure cement paste. In concrete, sand is an essential element and it is relevant to analyze how the sand particles will affect the microstructure of the interface between the large aggregate and the matrix. For mortars, Diamond et al. (3.40,3.41,3.42) they showed that the minimum distance of separation between grains is, on average, less than $100\mu m$. Since the aggregate-cement paste interface is around $50\mu m$, one would expect that most of

* Not ready. (It is with the draft present)

XRD Analysis of the Intergrow when Alite Paste is Cast Against A Marble
 (4/11)



the concrete is affected by the interfacial zone, leaving very little room for the "bulk" cement paste to develop. In order to study this topic further, the mortar-aggregate interface was analyzed both by scanning electron microscope (SEM) and by X-ray diffraction analysis (XRD).

3.6.1 Materials and Methods

The study of the interface was performed by casting mortar against rock forming a composite specimen. The reason for using a polished surface was to establish a reference plane in order to determine the thickness of the interfacial zone. At some specified ages, the specimen was broken at the interface of the two distinct materials. The two halves obtained from the composite specimen were analyzed by SEM and XRD.

ASTM Type II portland cement was used (table 1.1), and the mortar was cast with 0.5 w/c and a sand to cement ratio of 2.25. The sand had a fineness modulus of 2.93 and the gradation is given in the table below.

Table 3.3
Particle Size Analysis of the Sand

Sieve Size	Cumulative % Retained
# 4	0
# 8	13
# 16	40
# 30	64
# 50	83
# 100	93
# 200	97

3.6.2 Results and Discussion

Figure 3.49 shows the film of calcium hydroxide growing in contact to the aggregate surface, on the mortar side. Figure 3.50 shows the preferential growth of calcium hydroxide crystal influenced by the aggregate surface. It should be mentioned that well-defined hexagonal crystal is rare on the interface and it is probably due to the original existence of a void at the interface. Figure 3.51 shows a detail of the develop-

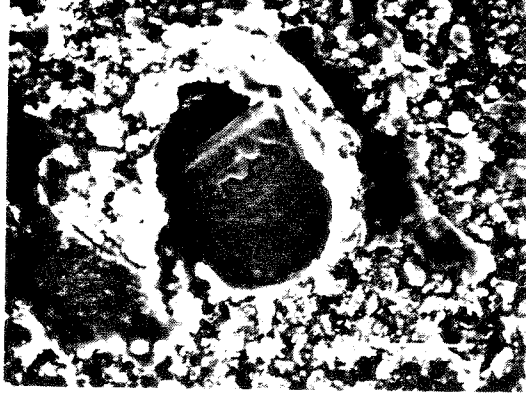


FIG. #350

Formation of well-defined hexagonal crystal of calcium hydroxide on the interface. Compare this crystal with the calcium hydroxide film shown in FIG. #349, where no distinct crystal morphology can be seen.

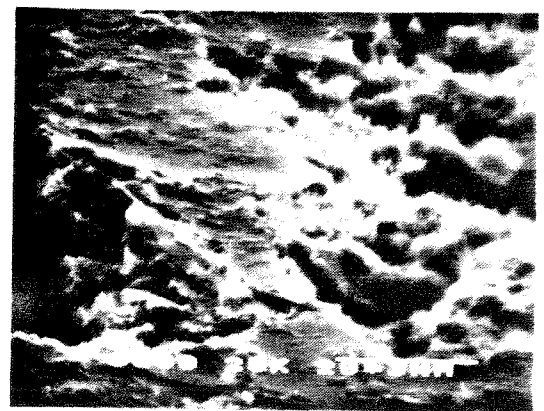


FIG. #349

Calcium hydroxide film and CSH formed on the mortar side of the interface. The age of this specimen was 30 days.

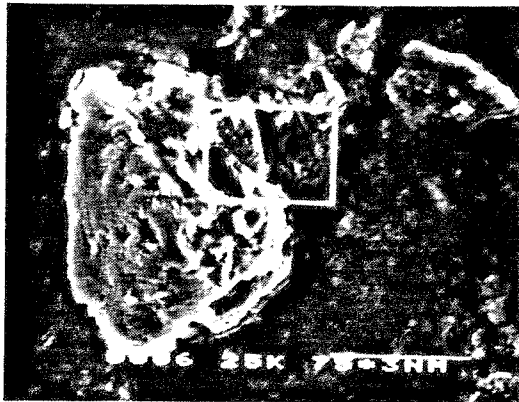


FIG. #352

Sand particle surrounded by the calcium hydroxide film (dark zone) at the interface. The age of this specimen was 30 days.



FIG. 3.51

Detail of the hexagonal crystal of calcium hydroxide shown in FIG. #352. The development of platelets with a preferential plane (00.1) can be seen.



FIG. #353

Detail of the outlined area (magnified 5 times) shown in FIG. #352. The sand grain creates surface effects similar to those produced by the large aggregate. There is precipitation of calcium hydroxide with a preferential orientation around the sand grain surface.

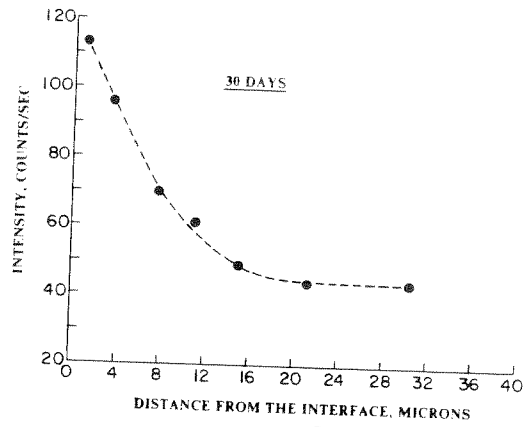


FIG. # 3.54
 VARIATION IN THE ETTRINGITE CONCENTRATION
 IN THE INTERFACIAL ZONE

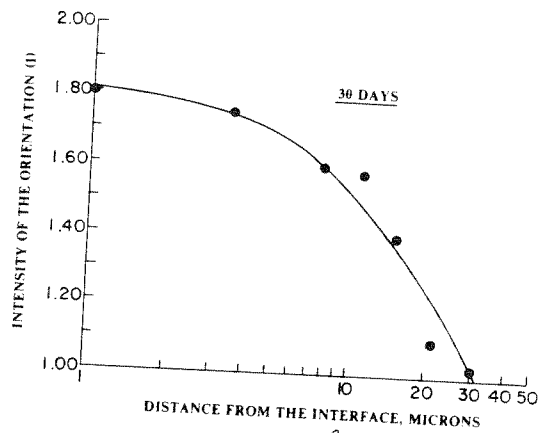


FIG. # 3.55
 VARIATION IN THE CALCIUM HYDROXIDE PREFERENTIAL
 ORIENTATION INDEX (I) IN THE INTERFACIAL ZONE

ment of the preferential plane (00.1) of these crystals.

Figure 3.52 shows a particle of sand that was in contact with the aggregate and is surrounded by the calcium hydroxide film with a preferential orientation. The sand particle also causes surface effects originating calcium hydroxide crystals growing in a preferential way as shown in Figure 5.3. This originates an interference between the original surface effects produced by the large aggregate and those produced by the sand.

As demonstrated in Fig 3.54, with increasing distance from the aggregate face the degree of preferential orientation decreases up to a point where random orientation of the crystals is achieved.

The technique of successive abrasion makes possible the determination of the distribution of ettringite concentration over the interfacial zone. Figure 3.55 shows that there is a great concentration of ettringite near the aggregate surface: This fact supports the through-solution mechanism by which the calcium, sulfate and aluminate ions can easily diffuse towards the aggregate surface so that more ettringite gets precipitated there. The same phenomenon has been reported for the aggregate-cement paste interface by Ollivier (3.11), Monteiro and Mehta (3.43).

In summary, the thickness of the "auréole de transition" is determined by the intensity of the surface effects produced by the aggregate. The thickness is larger for larger aggregates and it is also a function of the size and shape of the sand particles. The surface effects originated by the sand particles interfere with those caused by the large aggregate and the intensity of this interference determines the the final thickness of the transition zone.

3.5 References

- 3.1 Farran J., "Contribution Minéralogique a l'étude de l'adhérence entre les Constituants Hydrates des Ciments et les Matériaux Enrobés". Revue Mater.

- Constr. Trav. Publ. 490,491,492, 1956.
- 3.2 Farran J. and Maso J.C., *Revue Mater. Constr.* 587-588 , 1964.
- 3.3 Maso J.C., 'La Nature Minéralogique des Agrégats, Facteurs Essentiel de la Résistance des Bétons à la Rupture et à l'action du Gel', Thèse, Toulouse , 1967.
- 3.4 Hadley D.H., 'The Nature of the Paste-Aggregate Interface'. Ph.D Thesis. Purdue University, 1972.
- 3.5 Barnes B., 'Morphology of the Paste-Aggregate Interface'. Ph.D Thesis, Purdue University, 1975.
- 3.6 Struble L. and Mindess S., *The International Journal of Cement Composites and Lightweight Concrete*, 5, 2, 1983.
- 3.7 Iwasaki N. and Tomiyama, 'Bond Strength Between Cement Paste and Aggregate'. Rev. 28th. Gen. Mtg., Cem. Assoc. Japan, 122, 1974.
- 3.8 Farran J., Javelas R., Maso J.C. and Perrin B., 'Existence d'une Aureole de Transition entre les Granulats d'un Mortier, ou d'un Béton et la Masse de la Pâte de Ciment Hydraté'. *Comptes rendus* 275, 1467 , 1972.
- 3.9 Perrin B. 'Observation en Microscopie Electronique des Caractères Morphologiques de la Liaison Pâte de Ciment Durci-Matériaux Enrobés'. Ph.D Thesis, Toulouse, 1974.
- 3.10 Grandet J. and Ollivier J.P., 'Nouvelle Méthode d'étude des Interfaces Ciment-Granulats'. 7 International Congress on the Chemistry of Cement, Volume III, VII-85.
- 3.11 Barnes B.D., Diamond S., Dolch W.L., 'Micromorphology of the Interfacial Zone around Aggregates in Portland Cement Mortar'. *Journal of Am. Cer. Soc.* 62.21

- 3.12 Schwiete H.E., Ludwig U. and Albeck J., 'Die Bindung von Zuschlagstoffen and Zementstein'. W iss. Z. Tech. Univ. Dresden 17, 1587, 1968.
- 3.13 Bertacchi P., 'Adherence entre Aggregats et Ciment et son Influence sur les Caracteristiques des Betons'. Rev. Mater. Constr. Trav. Publics 659 , 243, 1970.
- 3.14 Buck A.D. and Dolch W.L. 'Investigation of the Reaction Involving Non-dolomitic Limestone Aggregate in Concrete'. J. Am. Concr. Inst. 63 , 755, 1966.
- 3.15 Ollivier J.P., 'Contribution a l'Etude de l'Hydratation de la Pate de Ciment Portland au Voisinage des Granulats'. Thesis Toulouse, 1981.
- 3.16 Schwiete H.E., Ludwig U. and Jaeger P., Symp. on Structure of Portland Cement Paste and Concrete, Highw. Res. Bd., Spec. Rep. 90, 353 , 1966.
- 3.17 Ish-Shalom M. and Bentur A., 'Properties of Type K Expansive Cement of Pure Components; I. Hydration of Unrestrained Paste of Expansive Components. Results'. Cement and Concrete Research, 4, 519 , 1974.
- 3.18 Bentur A. and Ish-Shalom M., 'Properties of Type K Expansive Cement of Pure Components; II. Proposed Mechanism of Ettringite Formation and Expansion in Unrestrained Paste of Pure Expansive Component'. Cement and Concrete Research, 4, 709 , 1974.
- 3.19 Ish-Shalom M. and Bentour A., 'Properties of Type K Expansive Cement of Pure Components; III. Hydration of Pure Component Under Varying Restraining Conditions', Cement and Concrete Research, 5, 139, 1975.
- 3.20 Hansen W.C., Proc ASTM 63, 932 , 1963.
- 3.21 Chatterji S., Proceedings of the Fifth Intl. Symposium on the Chemistry of Cements, 336, Tokyo, 1968.
- 3.22 Chatterji S., Trans. and J. British Ceram. Soc. 70, 195 , 1971.

- 3.23 Mehta P.K., 'Scanning Electron Micrographic Studies of Ettringite Formation'. Cement and Concrete Research, 6, 169, 1976.
- 3.24 Grutzeck M. W., Atkinson S. and Roy D.M., 'Mechanism of Hydration of Condensed Silica Fume in Calcium Hydroxide Solutions'. ACI Publication SP-79, 1983.
- 3.25 Chatterji S. and Jeffery J.W., 'A New Hypothesis of Sulfate Expansion'. Mag. Concrete Res., 15, No. 44, 83, 1963.
- 3.26 Mehta P.K., 'Effect of Lime on Hydration of Pastes Containing Gypsum and Calcium Aluminates or Calcium Sulfoaluminates'. J. Am. Ceram. Soc. 56, 315, 1973.
- 3.27 Mehta P.K., 'Mechanism of Expansion Associated with Ettringite Formation'. Cement and Concrete Research, 3, 1, 1973.
- 3.28 Mehta P.K. and Hu F., 'Further Evidence of Ettringite by Water Adsorption'. J. Am. Cer. Soc., 61, 1978.
- 3.29 Mikhailov V.V., 'Stressing Cement and Self-Stressed Structures in the USSR'. ACI Publication, No. SP-38, 415, 1973.
- 3.30 Mehta P.K., 'Expansive Characteristics of Calcium Sulfoaluminate Hydrats'. J. Am. Cer. Soc., 61, 1967.
- 3.31 Polivka M. and Willson C., 'Properties of Shrinkage-Compensating Concretes'. ACI Publication No. SP-38, 227, 1973.
- 3.32 Hoff G.C. and Mather K., 'A Look at Type K Shrinkage-Compensating Cement Production and Specifications'. ACI Symp. on Expansive Cement, New Orleans, 1977.
- 3.33 Chatterji S. and Jeffery J.W., 'The Nature of the Bond Between Different Types of Aggregate and Portland Cement'. Indian Concr. J. 45, 346, 1971.

- 3.34 Lyubimova T. Yu and Pinus E.R., "Crystallization Structure in the Contact Zone between Aggregate and Cement in Concrete". Colloid J. USSR. 24, 491, 1962.
- 3.35 Cussino L. and Pintor G., "An Investigation into the Different Behaviour of Silicic and Calcareous Aggregates in Mixes with Regard to the Mineralogical Composition of the Cement". Il Cemento, 4, 255, 1972.
- 3.36 Cussino L., Murat M. and Negro A., "Chemical and Physical Study about Bound between Cement and Calcareous Siliceous Aggregates in the Mortars". Il Cemento, 23, 77, 1976.
- 3.37 Grandet J. and Ollivier J.P., "Etude de la Formation du Monocarboaluminate de Calcium Hydrate au Contact d'un Granulat Calcaire dans une Pate de Ciment Portland" Cement and Concrete Research, 10, 759, 1980.
- 3.38 Schimmel G., "Basische Calciumcarbonate". Natur. 57, 38, 1970.
- 3.39 Schimmel G., "Elektronenmikroskopische Beobachtungen an basischen Calciumcarbonaten". Phys. Blätter, 5, 213, 1970.
- 3.40 Diamond S., Mindess S. and Lovell J., "On the Spacing between Aggregate Grains in Concrete and the Dimensions of the Aureole de Transition" Colloque International, Rilem, Toulouse, France, 1982.
- 3.41 Mindess S. and Diamond S., "A Device for Direct Observation of Cracking of Cement Paste or Mortar Under Compressive Loading Within a Scanning Electron Microscope". Cement and Concrete Research, 12, 569, 1982.
- 3.42 Diamond S., Mindess S. and Lovell J., "Use of a Robinson Backscatter Detector and "Wet Cell" for Examination of Wet Cement Paste and Mortar Specimens Under Load". Cement and Concrete Research, 13, 107, 1983.
- 3.43 Monteiro P.J.M. and Mehta P.K., "Ettringite Formation on the Aggregate-Cement Paste Interface". Cement and Concrete Research, 15, 378, 1985.

CHAPTER 4

MECHANICAL PROPERTIES OF THE AGGREGATE-CEMENT PASTE BOND

4.1. Introduction

In Chapter 3, the microstructure and morphology of the aggregate-cement paste interface was studied. In summary, the main characteristics of the interfacial zone for portland cement are the following:

1. Development of a higher porosity than in the bulk cement paste.
2. Formation of larger crystal structure of the hydration products.
3. Deposition of calcium hydroxide crystals with a preferential orientation on the interface.

While these facts are relevant, they do not provide quantitative information on how much they influence the bond strength. In this chapter the mechanical properties of the interface was studied both in a microscopic and macroscopic level.

The state of the art on the aggregate-cement paste interface up to 1965 was carefully reviewed by Alexander and al. (4.1) Struble et al. (4.2) completed the data up to 1980. Rather than repeating the information given in the above comprehensive works, it would be more fruitful to reanalyze and discuss some of the research performed before the 20 th century which was not presented in the mentioned state of the art reports. It should be remembered that in the middle of the nineteen century outstanding scientists intensively researched cement and mortar. The work of Le Chatellier, Vicat and Michaelis on the cement hydration served as an advanced starting

point for modern researchers. Bauschinger made major contributions to the science of the strength of materials and besides his well known research in metals ('Bauschinger effect') he performed extensive work on the strength of cements, mortars, artificial and natural stones. In the United States, Johnson (4.3) and Gillmore (4.4) performed detailed tests on the cements and mortar, the later researcher, a Brig. General of the Enginner Bureau of the War Department, combined research with a very prolific practical experience.

Another point that should be made is that during this time one of the main applications of mortar was for mansory work, therefore the adhesion between cement paste (or mortar) and brick or stone was of major concern.

One way of testing the adhesion was to cement bricks and blocks of stone together in cruciform shape and afterwards drawing them apart by a force applied at right angles to the plane of the joint. The blocks would be kept together under a pressure of 500 lbs. until the mortar had set. The testing device, shown in Fig 4.1, consisted of a bed piece and two upright posts, one foot apart, connected by a cross-piece at the top. A scale beam was suspended at the center of the cross-piece. The lower hook of the scale beam was connected with a horizontal lever of equal arms. Therefore, the weight indicated by the beam would be transmitted to the reverse end of the lever, acting as a downward pressure. For compressive strength tests, the wedge-shaped piece which acts on the prism would be replaced by another which would distributed the pressure as shown in Figure 4.1. For the adhesion tests, the cruciform-shaped specimen was placed directly under the hooks of the scale beam. Of course, the lower lever should have been removed in advance. The lower brick or stone was confined to the bed piece by staples, while the upper part of the cruciform was embraced by the ends of a crescent-shaped iron, suspended from the hook of the scale-beam. In these tests, rupture was attained as quickly as possible, taking the necessary care of avoiding shock waves, by pouring sand into the pan of the spring-

balance suspended from some given point of the beam.

An extensive program for the brick-cement paste (and mortar) bond was performed for the Croton Point front bricks and tested after 320 days. Some of the specimens were wetted with a sponge every two or three days, while others were kept dry. The real bond strength could not be satisfactorily measured because in many tests the adhesion to the brick overcame the cohesive strength either of the bricks themselves, or of the mortar composing joint between them. The researcher experienced first hand, what would become a somewhat frustrating tradition in measuring bond resistance for over a century, that is, no matter how carefully the program was executed, there would always be some unexpected problem that would prevent to completely understand the bond behavior and mechanism. However, even though a complete understanding is not yet possible, some interesting partial deductions can always be done with most tests. In the case of the Croton Point front bricks, the conclusions were the following:

1. Particles of unground cement particles exceeding $1/80$ inch in diameter may be allowed in the cement paste without sand to the extent of fifty per cent of the whole, without detriment to its adhesive or cohesive properties, while a corresponding proportion of sand injures the strength of the mortars in these respects about forty per cent.
2. When these unground particles exist in the cement paste to the extent of the sixty-six per cent of the whole, the adhesive strength is diminished about twenty-eighth per cent. For a corresponding proportion of sand, the diminution is sixty-eighth per cent.
3. The addition of these sifting exercises a less injurious effect upon the cohesive than upon the adhesive property of cement. The converse is true when sand, instead of sifting, is used...
4. At the age of 320 days (and perhaps considerably within this period), the cohesive strength of pure cement mortar exceeds that of Croton front bricks. (The converse is true when the mortar contains fifty per cent or more of sand).
5. When cement is to be used without sand, as may be the case when grouting is resorted to, or when old walls are to be repaired by injections of thin paste, there is no advantage in having it ground to an impalpable powder.

An important issue was to study the effect of the sand on the adhesive properties of the mortars. Wheeler (4.5) showed that the trend that increasing amounts of sand

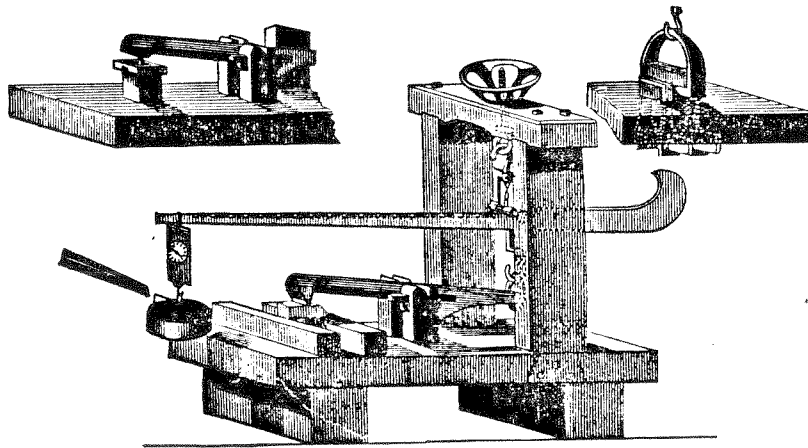


Fig 4.1
 Testing Machine used by In Testing Bond
 Mearching

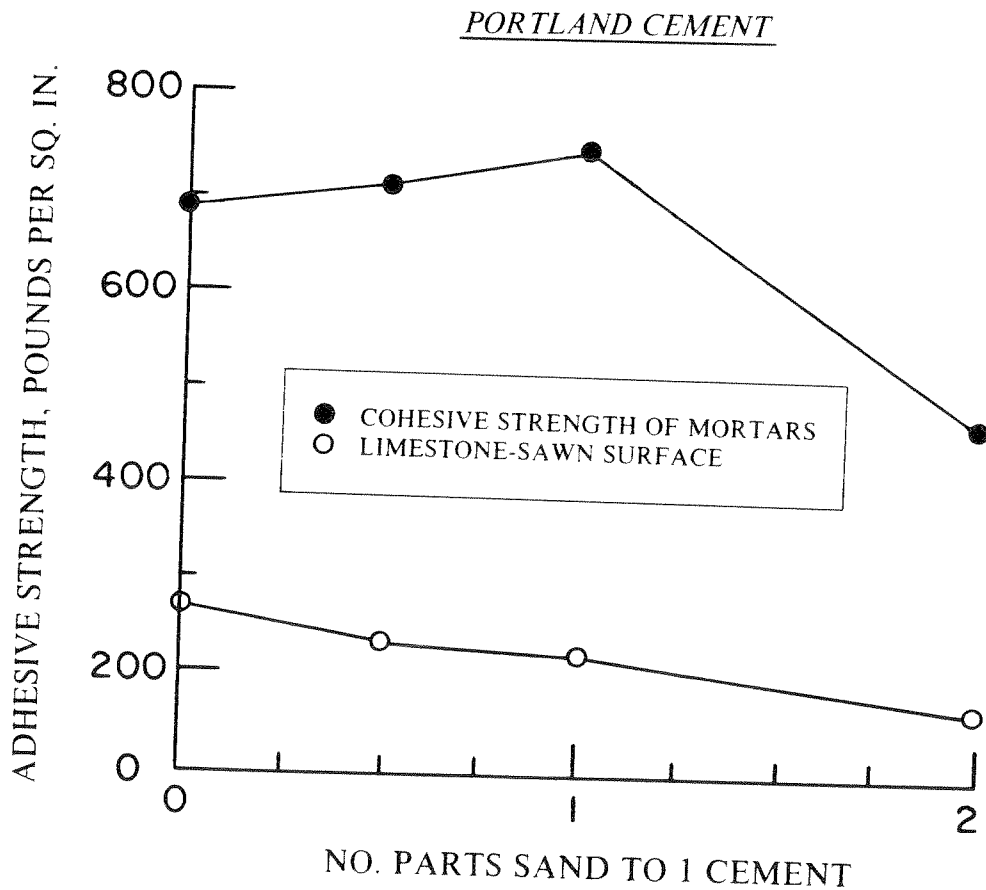


Fig 4.2
 Effect of Sand Content on the Adhesive Properties of Mortars

decreased the bond strength was confirmed (Fig 4.2).

Johnson (4.3) reported a standard test of adhesion, according to the recommendations given by the French Commission. The adhesion specimen would be made of a special form of briquette, moulded in two parts, these two parts consisting of the two materials whose adhesion is to be tested, provided both can be molded or using a prism of the solid material to which adhesion is to be determined (Fig. 4.3). Wheeler (4.5) using this type of briquette determined the adhesive strength of portland cement mortar with various substances. As it can be seen in Fig 4.4, the adhesive strength ranged from 300 psi on sawn brick to 85 psi on sandstone having a cleavage surface. This important result on the influence of the rock nature on the bond was somewhat neglected until Farran wrote his classical papers in 1955 (see chapter 3 for details).

In this chapter results for the aggregate-cement paste bond will be presented. Microhardness tests were performed on the CH film. A comprehensive test on the mechanical properties of the bond was performed. The program included four types of rocks (basalt, amphibole-gneiss, granite and limestone) with three surface conditions (smooth, sand-blasted and rough) tested at different ages. Over 150 tests were performed to characterize the properties of the rock and cement paste and in order to perform an analysis of the aggregate-cement paste bond using probabilistic treatment over 170 bond tests were conducted.

4.2 Microhardness Tests on the Interfacial Film

The micro-hardness measurements made by Lyubimova and Pinus (4.6) shown in Fig 4.5 are a classic reference found in many textbooks. According to their results, there is a considerable decrease in the microhardness in the transition zone as compared to the bulk paste. Even though the results have a very attractive interpretation, it should be mentioned that recent research by Skalny and Mindess (4.7) performing several hundred microhardness measurements on the transition zone was not able to

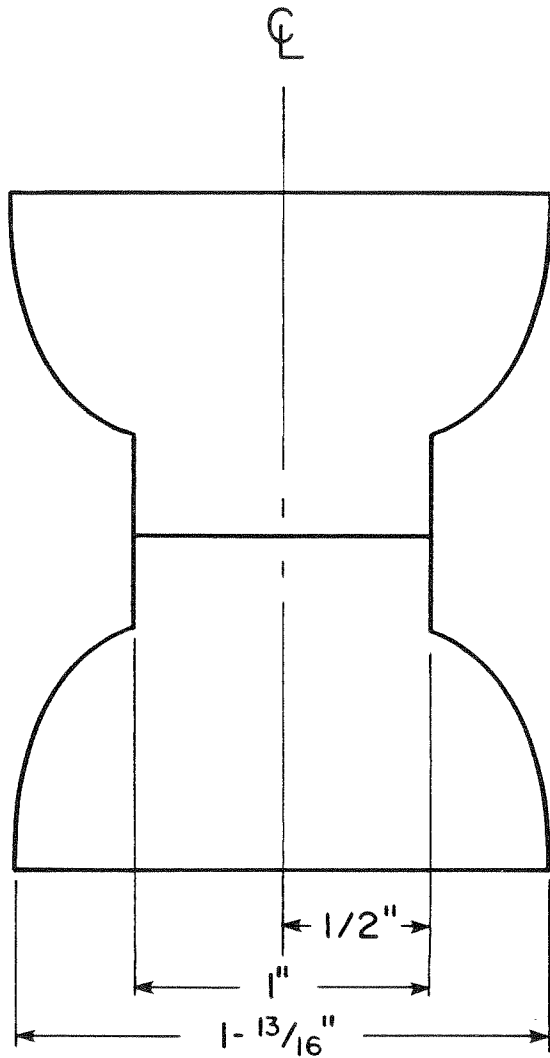


Fig 4.3
Bond Specimen

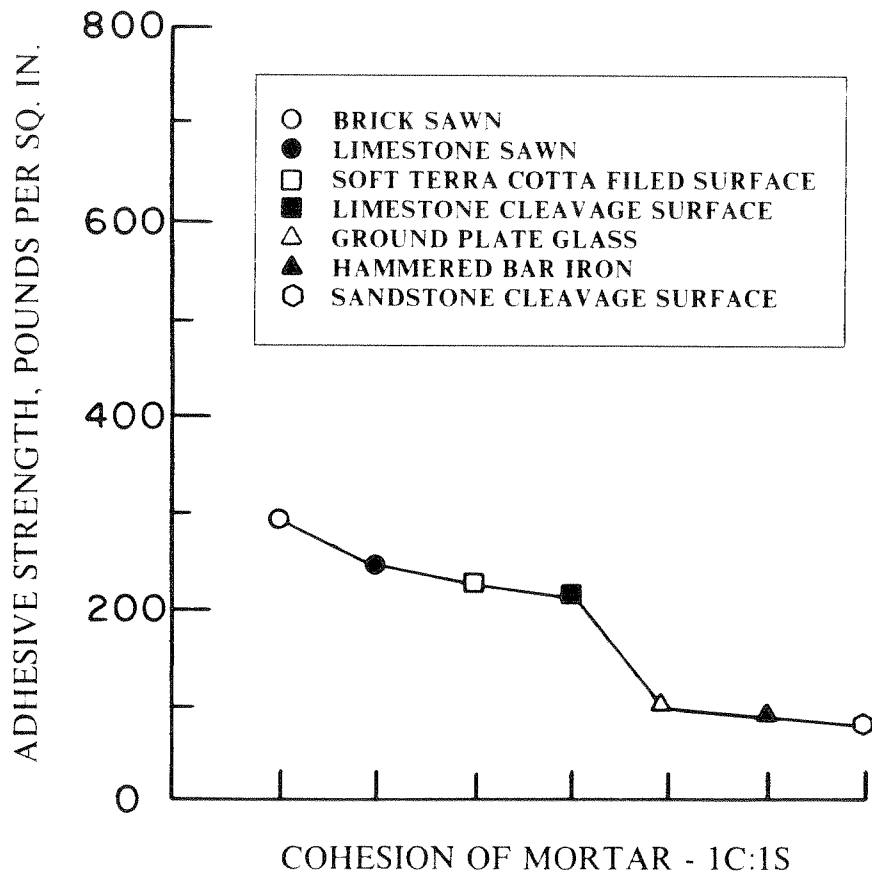


Fig 44
Effect of Type of Rock on the Bond Strength

make any statistically significant conclusion. Also the idea of taking microhardness measurements on the transition zone by successive abrasion of the interface was not successful (4.8).

In this section, the analysis of microhardness will be limited to the interfacial film. The film is fairly homogeneous and well crystallized while the transition zone is porous and inhomogeneous, therefore the microhardness results for the film should be more reproducible. A more ambitious goal is to develop some of the fundamentals for the fracture toughness of film using indentation techniques.

This research will use the Vickers pyramid and Fig. 4.6 shows a schematic diagram of the load P and the 'plastic' impression $.I a$ and the radial/median crack $.I c$. It can be shown that the hardness H and the toughness K_c of the material are given by (4.9):

$$H = \frac{P}{\alpha_o a^2}$$

$$K_c = \frac{P}{\beta_o c^{3/2}}$$

where α_o and β_o are constants. For the Vickers indenters $\alpha_o = 2$ and β_o is a complex geometrical factor.

Let us start analyzing a 30-day old interfacial film obtained when cement paste was cast against a quartz aggregate. Fig. 4.7 shows the impression of the Vickers pyramid on the film and as it can be noted the impression was sharp and well defined, however there was no development of radial/median crack pattern. To check the reproducibility, different loads were applied in order to induce a range of values of $.I a$ and as it can be seen in Fig. 4.8 the results were very good. The hardness of this film was $(6.34 \pm 0.17) 10^5 \text{ kg/m}^2$. It should be mentioned that no cracks were obtained for any load level and beyond a threshold load (30 kg in this particular test) the displaced material tended to pile up on the corners of the impression as shown in Fig. 4.9.

One reason why there was no formation of cracks could be because of the high

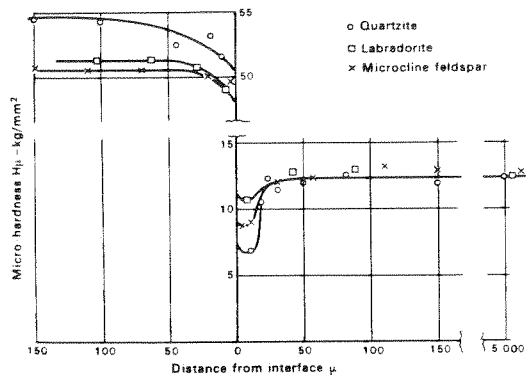


Fig. 4.5
 Variation in Micro-hardness Across the Transition zone

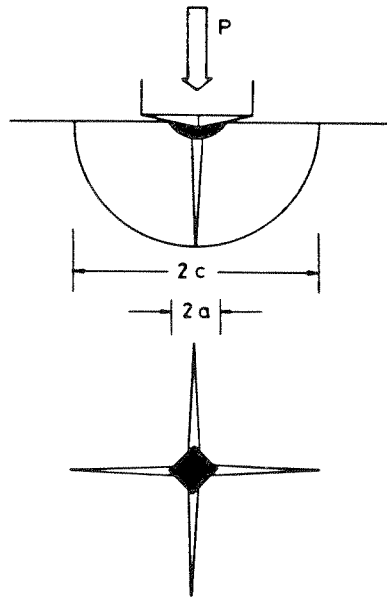


Fig. 4.6 Schematic of Vickers-produced indentation-fracture system, peak load P , showing characteristic dimensions c and a of penny-like radial/median crack and hardness impression, respectively.

flexibility of the film added to the existence of a less dense zone behind the film at this age. It should be interesting to know if with increasing age as hydration continues and the zone behind the film gets denser, and therefore decreasing the flexibility of the film, the formation of the cracks on the film would occur. This turned out to be the case for a year old interfacial film as shown in Fig. 4.10. The hardness increased about 25%, giving a value of $(7.89 \pm 0.40) 10^5 \text{kg}/\text{m}^2$.

The development of a system of cracks due to the indentation motivates some exploratory discussion on the fracture toughness of the transition zone using the indentation fracture technique. The word exploratory should be emphasized because even though this technique is fairly well established for homogeneous ceramic materials (4.10, 4.11) the transition zone still have many unknown characteristics which prevents the knowledge of the limitations in adopting such methods. Also the techniques for measuring the interface toughness of thin films is still in the initial stages, even though fast progress has been achieved (4.12). Anstis et al. (4.9) derived for the indentation test the functional dependence of the toughness K_c and the pertinent parameters (contact force P , material hardness H , elastic modulus E) by the following equation:

$$K_c = \delta_v P (E/H)^{1/2} c^{-3/2}$$

where δ_v is a material-independent constant for the Vickers-produced radial cracks, and in this work it is adopted the value 0.016.

Applying this equation for the indentation tests of the 1-year old transition zone and assuming an elastic modulus of $50 \text{GN}/\text{m}^2$ the average value for the toughness is $0.07 \text{MN}/\text{m}^{3/2}$. It should be mentioned that Hillemeier and Hilsdorf (4.13) obtained an average value of $0.1 \text{MN}/\text{m}^{3/2}$ for the fracture toughness of the cement paste-rock interface using a CT-specimen. The fact that the toughness of the transition zone and of the cement-rock interface yielded values of the same order of magnitude is very encouraging. Nevertheless, the indentation techniques for measuring the fracture

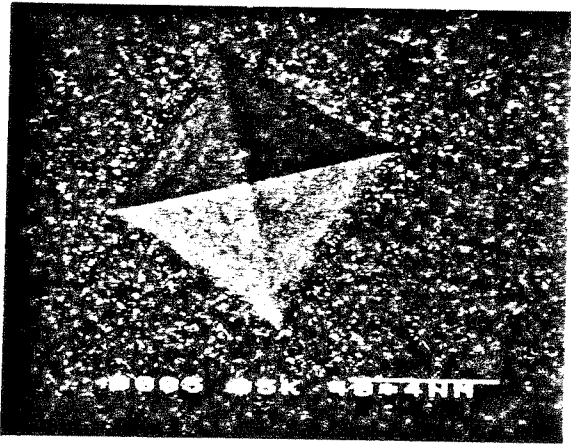


Fig 4.7
Impression of the Vickers pyramid on the
CH film (30-days old specimen)



Fig 4.9
Displaced Material piling up on the
corners for Higher loads



Fig 4.10
Development of a System of cracks
(1-year old specimen)

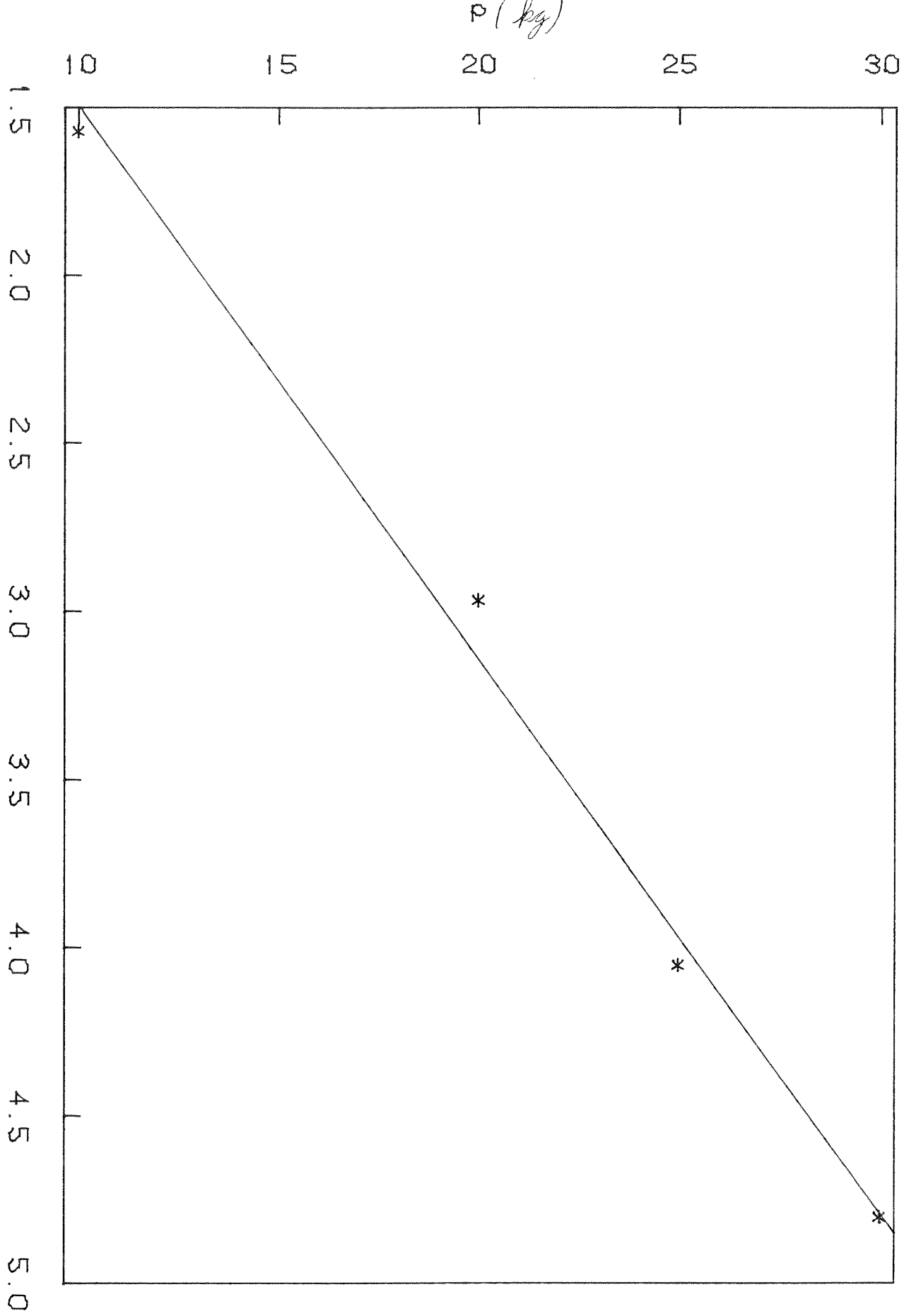


Fig 4.11
Crack Arrested at a void



Fig 4.12
Complex System of cracks

The of Different kinds of α α^2 ($10^{-5} m$)
the Revision of the Measurements



toughness of the transition zone should be analyzed in more details to understand its limitations. As examples, Fig. 4.11 shows that the "south" crack did not develop, probably because it was arrested in the void close to the bottom of the impression; and Fig 4.12 shows that sometimes the crack pattern can be more complicated than the one predicted.

4.3 A Note on Elastic Mismatch for Composite Materials

When dealing with composite materials, it is fundamental to realize the importance of the elastic mismatch in producing the final stress state in the material. In this section, attention will be given to the stress analysis of a body formed by two isotropic materials. Considering linear elasticity, the stresses in such material will usually depend on three parameters associated to the elastic constants of each individual material. However, Dundurs (4.14) showed that the number of parameters will decrease to two if the plane theory of elasticity is used; and it is interesting to point out that no restriction is made if the interfaces between the two materials are bonded or smooth, however if the body is multiply connected it is required that the vector sums of tractions on holes vanish for every hole.

The choice of the two parameters to characterize the elastic response of the composite material is not unique, Dundurs suggested the following:

$$\alpha = \frac{\mu' m'' - \mu'' m'}{\mu' m'' + \mu'' m'}$$

$$\beta = \frac{\mu'(m' - 2) - \mu''(m'' - 2)}{\mu' m' + \mu'' m''}$$

where

μ : shear modulus

ν : Poisson's ratio

$m = 4(1-\nu)$: for plane strain

$m = \frac{4}{1+\nu}$: for generalized plane stress

The superscripts ' and '' are used to distinguish the two materials.

This choice of parameters permits to create useful geometric constructions in the plane α, β . The range of Poisson's ratio and shear modulus is:

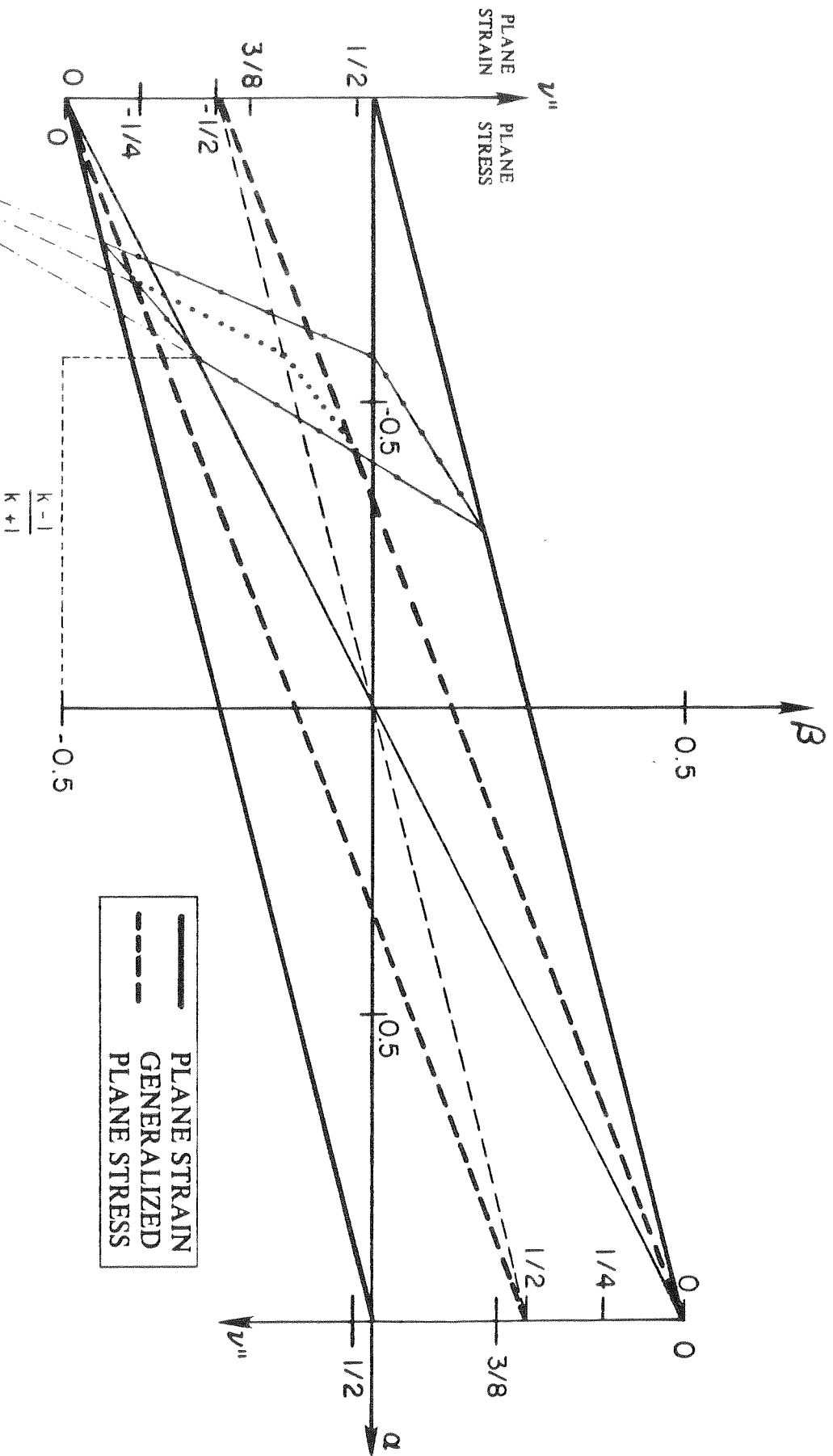
$$0 < \nu', \nu'' < 1/2 \quad 0 < \mu', \mu'' < \infty$$

in the α - β plane, all the possible values of α and β are contained in parallelograms, which are bounded by the lines (4.15, 4.16):

$$\alpha = \pm 1 \quad \beta = \begin{cases} (\alpha \pm 1)4 & \text{for plane strain} \\ (3\alpha \pm 1)/3 & \text{for generalized plane stress} \end{cases}$$

The α - β plane has the following characteristics:

- (I) The parallelogram corresponding to plane strain contain the one corresponding to plane stress.
- (II) Materials with the same shear moduli will be represented in the line $\alpha = \beta$. Identical materials will correspond to the origin (0,0).
- (III) The inversion in labeling the two materials causes a change of the α, β sign, as it can be easily verified. This inversion corresponds to a reflection through the origin in the α - β plane.
- (IV) The Poisson's ratio ν' increases upwardly from 0 to 0.5 while ν'' increases downwardly, as shown in Fig. 4.13. Note that this variation is not linear for plane strain, however it is linear for generalized plane stress. Materials with the same Poisson's ratio will be represented by a line passing through the origin.
- (V) Materials with a ratio of shear moduli k are represented by a quadrilateral "k-polygon", Bogy (4.17). When k and m are fixed the possible combination of α and β are restricted to a line that passes through the point $\alpha = \beta = -1$ (or $\alpha = \beta = 1$). Connecting these points to the terminal points of the line $\alpha = (k-1)/(k+1)$ the "k-polygon" is formed. Note that it degenerates to a straight line for $k = 0, 1, \infty$. Fig. 4.13 shows a "k-polygon" for $k = 0.27$. The selection for this value of k was motivated because it is a typical ratio for rock ($\mu = 26 \text{ GN m}^{-2}$) and cement paste ($\mu = 7 \text{ GN m}^{-2}$)



199 1. 43

4.4 Analysis of the Aggregate-Cement Paste Bond Using Probabilistic Treatment of Brittle Strength

The aim of this section is to characterize the statistical properties of the aggregate-cement paste bond as influenced by the age of the cement paste, the mineralogy of the rock and its surface conditions. It is expected that the aggregate-cement paste bond is influenced by the mechanical properties of the two materials (rock and cement paste). Therefore the following test program to study the mechanical behavior of the rock, cement paste and their interface was undertaken.

Rock

1. Specific Gravity and Absorption
2. Modulus of Elasticity
3. Compressive Strength
4. Tensile Strength

Cement

1. Chemical Analysis
2. Physical Tests

Cement Paste

1. Compressive Strength
2. Tensile Strength

Aggregate Cement-Paste Bond

1. Tensile Strength

Different authors used diverse tests for measuring the aggregate-cement paste bond. Although pure tension tests are attractive, the problems with the gripping on the extremities induce a state of stresses which may be far from homogeneous. Flexure tests are easy to perform and usually give reliable results. In this research a splitting

test ('brazilian test') along the interface was selected because of the interesting stress distribution that originates in the specimen and presents no problem with grips in order to originate tensile stresses on the interfacial plane.

In order to advance the knowledge on the concrete assessment it is necessary to characterize the statistical analysis of strength data for the evaluation of the failure probabilities. As it was emphasized in this work, concrete is a complex material and the traditional approach of modeling it as a two-phase material without considering the interfacial zone has severe limitations. In this section, two important items on the statistical analysis of the aggregate-cement paste bond will be addressed:

1. Laboratory test to obtain reliable strength data.
2. Use of a statistical model to describe failure.

There are many statistical models to analyze failure of brittle materials. In this work, the model proposed by Weibull will be used exclusively.

4.4.1 Weibull's Statistical Theory for Brittle Materials

In 1939 Weibull (4.18) developed a statistical formulation for the failure of brittle solids. It was remarkable that he was able to tackle this problem before the tools of the rigorous treatments of extreme value statistics were available. Weibull treated the case in which brittle solid can be assumed to be homogeneous, isotropic and containing uniformly distributed randomly oriented flaws.

Let us start reviewing this treatment as applied to uniaxial stress states to later on discuss the multiaxial stress states. In this formulation, it is assumed that brittle solids can be approximated by a series model, that is, the strength is that of the weakest unit. It is assumed that there is no interaction of flaws and failure occurs when the strength of the worst flaw is reached. Only tensile stress is assumed to cause failure.

Consider a chain of N links in which the individual failure probabilities (at a given load) are $F_1, F_2, \dots, F_i, \dots, F_n$. Denoting G and S the failure and survival

probabilities of the chain as a whole, the probability that the chain survives is the product of the individual survival probability.

$$S(\sigma) = 1 - G(\sigma) = \prod_{i=1}^N (1 - F_i)$$

and,

$$\begin{aligned} \ln S &= \sum_{i=1}^N \ln(1 - F_i) = -\sum_{i=1}^N \left(F_i + \frac{F_i^2}{2} + \frac{F_i^3}{3} + \dots \right) \\ \ln S &\approx -\sum_{i=1}^N F_i \end{aligned}$$

if F_i is small. We can generalize this result to a volume V composed of elements dV which may be under different tensile stresses σ . It is reasonable to assume that F_i for each volume element dV is proportional to its volume and some function of stress. Weibull proposed the following expression:

$$F_i(\sigma) = \left(\frac{\sigma}{\sigma_0} \right)^m dV$$

Therefore, the failure probability is given by:

$$G = 1 - S = 1 - e^{-\int \left(\frac{\sigma}{\sigma_0} \right)^m dV}$$

The parameter σ_0 , which has the dimensions of stress is a scaling constant, while the parameter m is often referred to as the Weibull parameter or the flaw density parameter.

It should be mentioned that this two parameter distribution predicts a small but finite probability of failure at low stresses. To avoid that Weibull proposed a three parameter distribution:

$$\begin{aligned} G(\sigma) &= 1 - e^{-\int \left(\frac{\sigma - \sigma_u}{\sigma_0} \right)^m dV} & \sigma > \sigma_u \\ G(\sigma) &= 0 & \sigma < \sigma_u \end{aligned}$$

The term σ_u is sometimes referred to as the zero strength.

For the multiaxial case the one-dimension stress state is replaced by the normal stress acting on a crack. The probability of failure is given by:

$$G = 1 - e^{-[K \int \sigma_n^n dA] dV}$$

In the principal stress space, as shown in Fig. 4.14.

$$\sigma_n = \cos^2 \varphi (\sigma_1 \cos^2 \psi + \sigma_2 \sin^2 \psi) + \sigma_3 \sin \psi \cos 2\varphi$$

$$dA = \frac{1}{4} \pi \cos \varphi d\psi d\varphi$$

and the integration is carried out over the range for which σ_n is tensile. The brazilian test was analyzed in detail by Vardar (4.19) and Vardar and Finnie (4.20). A general treatment is given by Ratigan (4.21).

There are many methods available for determining the constants for a two parameter model. In this work the cumulative probability of failure G is obtained after ranking the experimental data in ascending order:

$$G = \frac{j}{N+1}$$

j = rank position

N = number of tests

4.4.2 Materials

The properties of the cement used is given in Table 4.2.

The following rocks were used to study the aggregate cement paste bond: granite, amphibole-gneiss, basalt and limestone.

4.4.3 Test Methods

The specific gravity and absorption for the rock with a saturated surface dry condition was determined according to the ASTM method C127.

The compressive strength of the rock was determined according to the ASTM D 2938-79 method ("Unconfined Compressive Strength of Intact Rock Core Specimens"), because the samples were obtained from cores for a dam foundation.

The rock elastic modulus was determined according to the ASTM D 3148-79

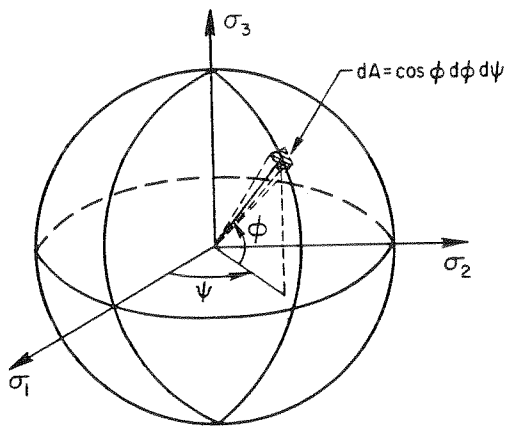


Figure 4.14 Geometric variables used to describe location on a unit sphere.

Fig 4.14

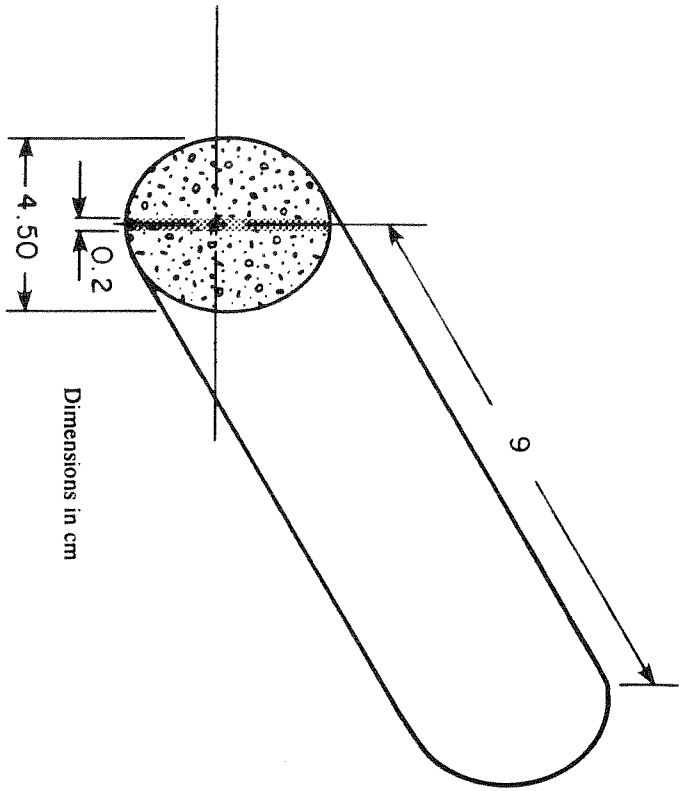
Table 4.2
Properties of the Cement

Physical Properties	
Fineness, No. 200 sieve	97.0 percent
Specific Surface, Blaine	3271 cm^2/g
Initial Set	4 hr. 40 min.
Specific Density	3.17 g/cm^3
A utoclave Expansion	0.06
Hydration Heat @ 7days	68.2 cal/g
Hydration Heat @ 28 days	83.5 cal/g
Chemical Properties	
Chemical Analysis	
Compound	Percentage Present
Silicon dioxide, SiO_2	21.14
Aluminum oxide, Al_2O_3	5.37
Ferric oxide, Fe_2O_3	2.65
Calcium oxide, CaO	64.48
Magnesium oxide, MgO	1.94
Sulfur trioxide, SO_3	1.45
Sodium oxide, Na_2O	0.20
Potassium oxide, K_2O	0.27
Ignition Loss	2.31
Calculated Compound Composition	
Compound	Percentage Present
Tricalcium Silicate, C_3S	57.85
D icalcium Silicate, C_2S	16.97
Tricalcium A luminumate, C_3A	9.75
Tetracalcium A luminumoferrite, C_4AF	8.06

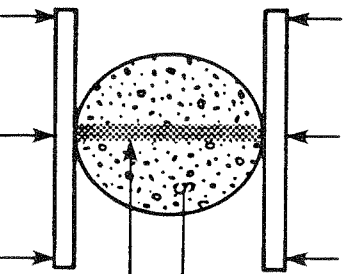
method ('Elastic Modulus of Intact Rock Core Specimens in Uniaxial Compression').

The height/diameter ratio of the specimen was equal to 2.

The aggregate-cement paste research was performed using cylindrical rock cores united by a cement paste along the diametral plane, as shown in Fig. 4.15. The cement paste had a 0.35 water to cement ratio. To avoid bleeding 0.1% of Natrosol (hidroxi-ethyl cellulose) was used. It was expected that the surface conditions of the rock would play an important rule on the bond results. Therefore, three surface conditions were analyzed. The first condition was 'polished surface' in which the cores were cut diametrically with a diamond sawn of 1.8 thickness; the second condition was



SPECIMEN DIMENSIONS



LOADING SCHEME

Fig 4/15
Bond Test

"sand-blast surface" in which the sawn-cut diametral surfaces were sand blasted to increase the roughness; and the third condition was "rough surface" in which the cores were failed by splitting test to originate the two diametral surfaces. After superficial saturation of the half cores, the two parts were fixed with Scotch tape after the introduction of a wood sheet 2mm thick, determining therefore the thickness of the bonding paste. After the pasting, the specimens were introduced in a wood mold with the original diameter. The process of molding the bond specimens is shown in Figs. 4.16.

The specimens were stored in the fog room until tested (28 and 90 days).

4.4.4 Test Results

The rock properties are shown in Table 4.3. The bond strength results are presented in Table 4.4. As expected, the bond strength was always smaller than the cement paste the tensile strength for all types of rock and all ages.

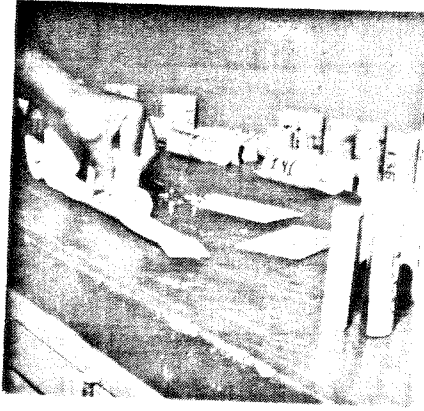
The effect of the aggregate surface on the bond strength was not uniform for all rocks, as shown in Fig. 4.17. For instance, for basalt the highest bond strength was obtained with fractured surface, while the limestone bond strength markedly decreased for the fracture surface as compared to the sand blast; Valenta (4.22) reported similar behavior for limestone-aggregate bond tested under flexure. The reasons for that may be the disruption of the rock surface by cracks or the creation of loose crystal grains of rock originated by the surface preparation, specially for the rough surface.

Fig 4.17 also shows that the results for the basalt-aggregate bond was in average lower than the other rocks. One of the reasons is the extremely high elastic modulus ($987,000 \text{ kgf/cm}^2$) which causes a greater stress concentration due to the elastic mismatch with the cement paste; one should note however the big dispersion of the results on the elastic modulus of the rock, with adds to the uncertainty of the bond strength.

At 28 days, the highest aggregate-cement paste strength was achieved for the



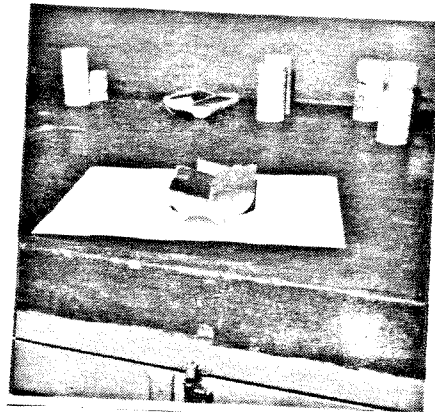
Use of a wood sheet 2 mm thick to fix the thickness of the paste



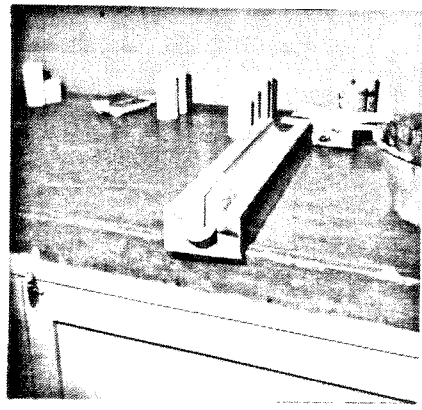
Placement of the specimen on a Scotch tape



Removal of the wood sheet



Placement of the cement paste



Mold to fix the final dimensions

Fig 4 15
Process of Molding The Bond Specimens

Table 4.3
Summary of the Rock Properties

Rock	Type of Test	# Specimens	Average	S. D. *
amphibole- gneisse	specific weight (kg/dm^3)	10	2.714	0.110
	absorption	10	0.36%	0.25%
	elastic modulus (kgf/cm^2)	5	748000	210000
	compressive strength (kgf/cm^2)	5	1151	548
	tensile strength (kgf/cm^2)	19	169.41	50.21
basalt	specific weight (kg/dm^3)	7	2.877	0.097
	absorption	7	0.76%	0.46%
	elastic modulus (kgf/cm^2)	5	987000	373000
	compressive strength (kgf/cm^2)	5	807	233
	tensile strength (kgf/cm^2)	18	164.17	39.21
granite	specific weight (kg/dm^3)	9	2.583	0.038
	absorption	9	1.14%	0.44%
	elastic modulus (kgf/cm^2)	12	266000	76000
	compressive strength (kgf/cm^2)	12	791	170
	tensile strength (kgf/cm^2)	6	94	19
limestone	tensile strength (kgf/cm^2)	20	76	10

*Standard Deviation

TABLE 4.4
Summary of the Strength Results

Material	Number of Specimens	Type of Test	Average ² (kgf/cm ²)	S.D.* (kgf/cm ²)
cement paste 28 days	15	compressive	269.15	80.92
cement paste 90 days	15	compressive	439.53	63.14
cement paste 28 days	15	splitting	29.37	7.17
cement paste 90 days	15	splitting	31.24	3.2
amphibole-gneisse/ cement paste smooth surface 28 days	21	bond	24.25	6.14
amphibole-gneisse/ cement paste smooth surface 90 days	20	bond	26.37	6.66
basalt/ cement paste smooth surface 28 days	20	bond	18.62	4.05
basalt/ cement paste smooth surface 90 days	22	bond	21.16	4.07
amphibole-gneisse/ cement paste sand blast surface 28 days	21	bond	24.94	5.41
basalt/ cement paste sand blast surface 28 days	16	bond	17.46	8.17
limestone/ cement paste sand blast surface 7 days	16	bond	24.53	8.74
limestone/ cement paste sand blast surface 28 days	16	bond	25.20	5.27
amphibole-gneisse/ cement paste rough surface 28 days	3	bond	16.17	1.55
basalt/ cement paste rough surface 28 days	3	bond	19.49	4.39
granite/ cement paste rough surface 28 days	5	bond	21.66	4.16
limestone/ cement paste rough surface 7 days	6	bond	22.05	7.27
limestone/ cement paste rough surface 28 days	6	bond	19.20	1.84

*Standard Deviation

limestone with sand blasted surface. This result would be expected according to the reactions that occur on the carbonate rock-cement paste interface as described in chapter 3.

AGGREGATE-CEMENT PASTE BOND STRENGTH 28 DAYS

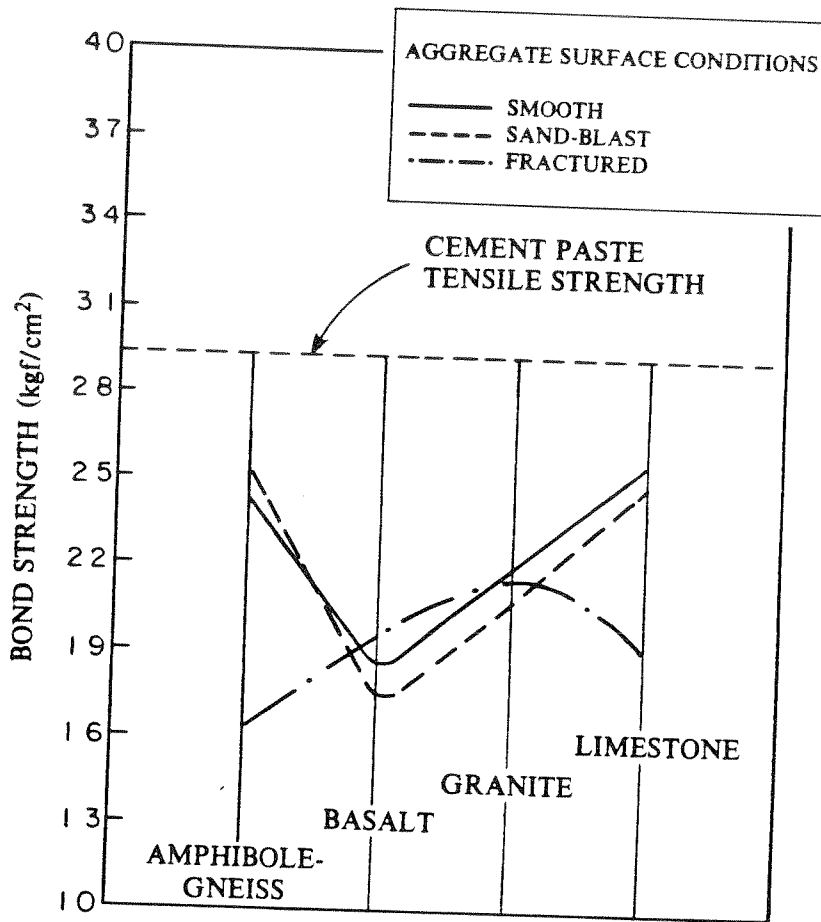


Fig. ~~4.16~~ 4.17

It should be noted that only tests with at least 16 results were included in the analysis. The value for m for each set was obtained from the slope of the plot $\log \log \left(1 - \frac{j}{N+1}\right)$. For the bond test, it was assumed a volumetric distribution of flaws on the cement paste zone. Figure 4.18 show the plot of the test results. As expected, because of the assumption $\sigma_u = 0$, the test results depart from the curve at lower stresses.

In this section, the aggregate-cement paste bond is assumed to have a brittle behavior under load, that is, the release of strain energy occurs only during rupture or fracture of the bond. In order to use extreme value statistics, it is assumed that flaws are present in large numbers. It is also assumed that these flaws are isotropically distributed and that they do not interact with one another. For concrete, this last assumption may be too restrictive because it is known that cracks may coalesce during failure, therefore the work presented here may be considered as an analysis of the local failure of the aggregate-cement paste interface; a global failure analysis for concrete will not be made because the complex crack interaction mechanism is not yet established.

4.5 Overall Conclusions

Combining the information in Chapters 3 and 4, it is now possible to discuss the effects of the aggregate-cement paste bond in concrete. Let us consider a typical volume of concrete, in which the aggregates are dispersed in the cement paste matrix as shown in Fig 4.19. The contact between the aggregate and the matrix may not be perfect, particularly when bleeding water accumulates under the larger aggregates producing localized zones of lower mechanical strength.

The surface effects of the aggregate originate zones of paste with a higher w/c ratio in the transition zone, causing the development of a different crystal structure as compared to the bulk matrix. The microstructure of the transition zone for a portland

(Note: axis for all series of Fig. 4.18)
4.18

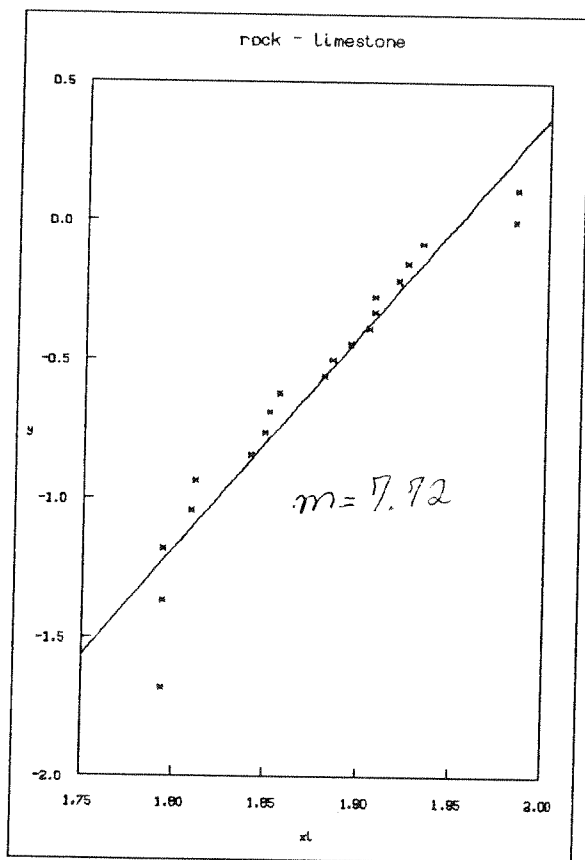
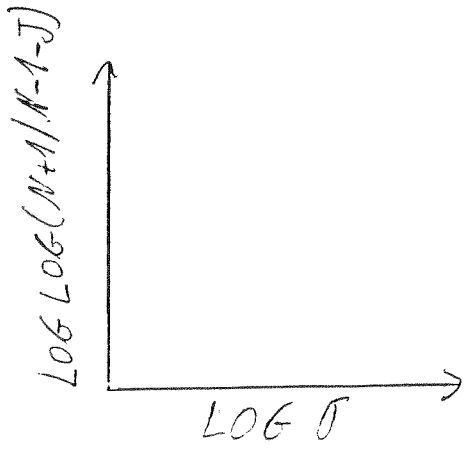
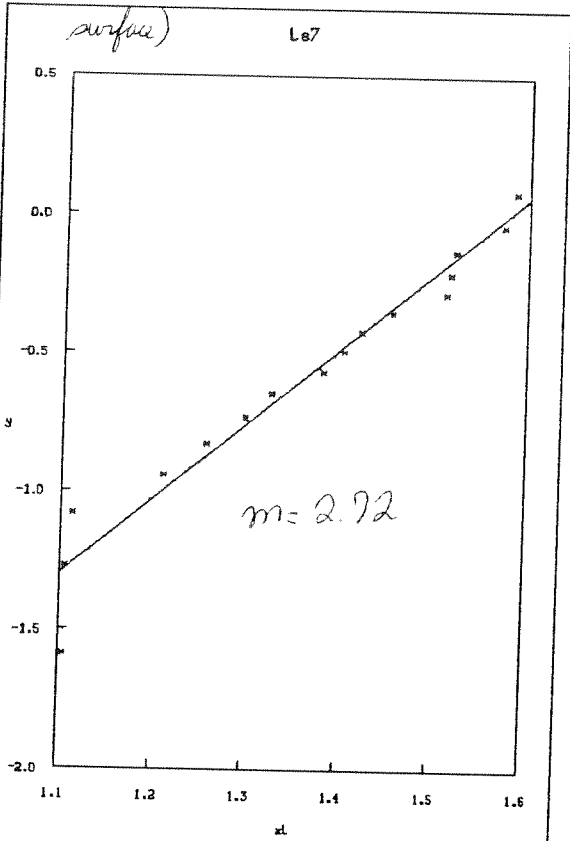
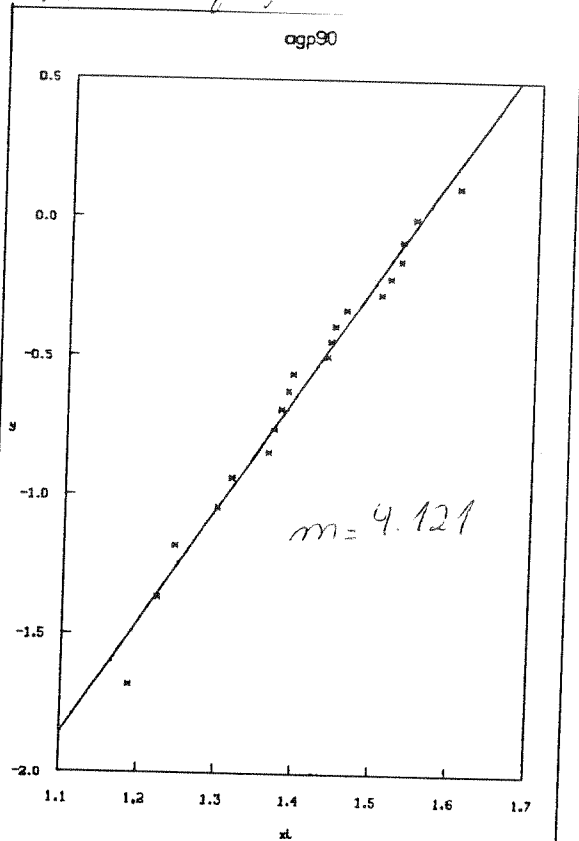


Fig 4.18 A
Plot to obtain Weibull parameter

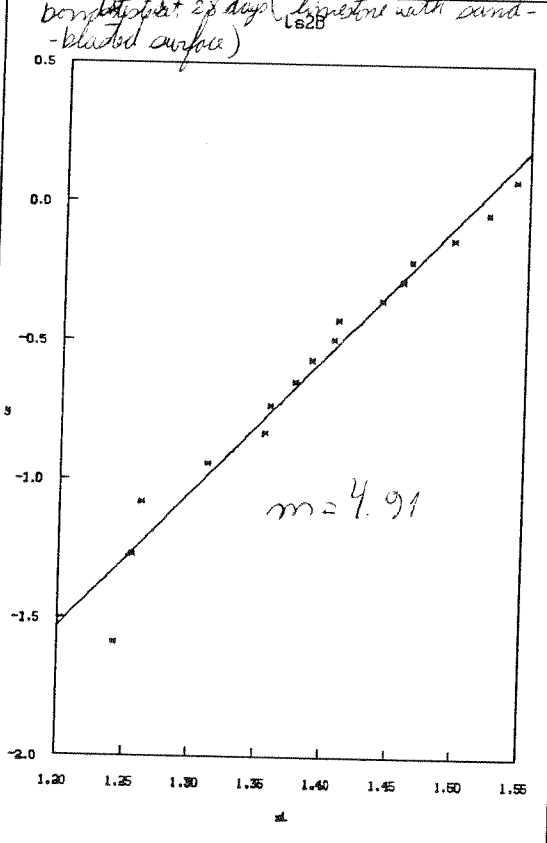
at 7 days
bond tested (limestone with sand-blasted surface)



bond tested at 90 days (amphibole-gneiss with smooth surface)



bond tested at 28 days (limestone with sand-blasted surface)



bond tested at 28 days (amphibole-gneiss with smooth surface)

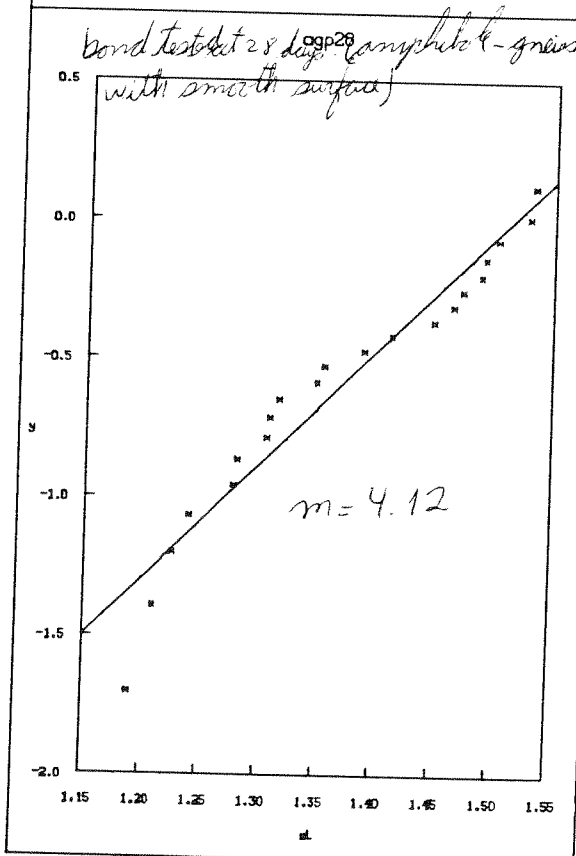
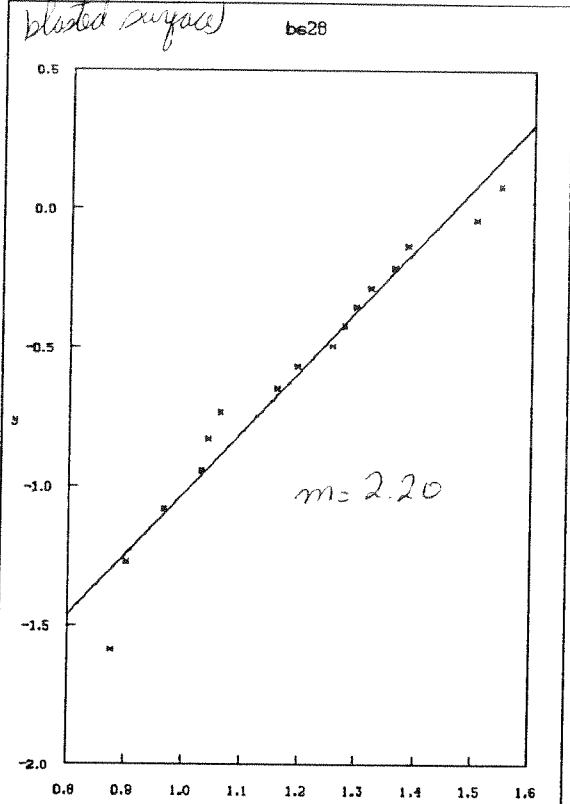
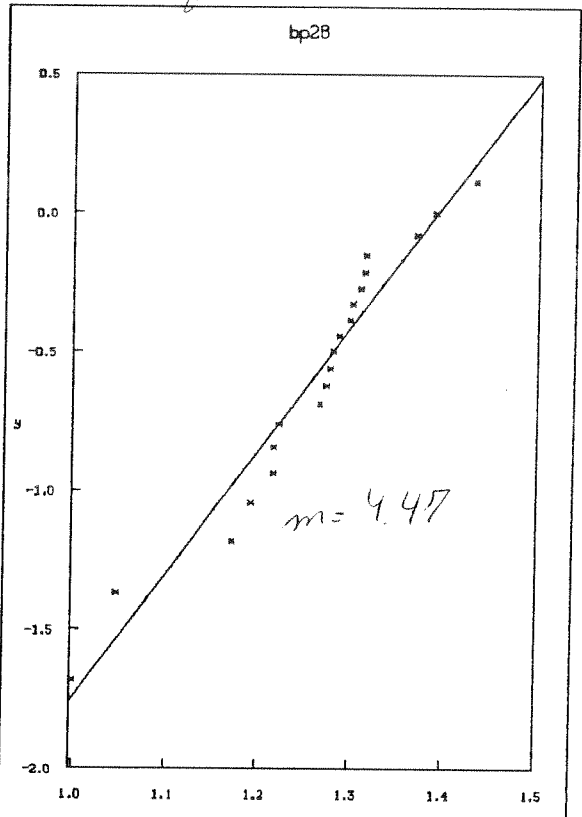


Fig 18.9
Plot to obtain Weibull parameter

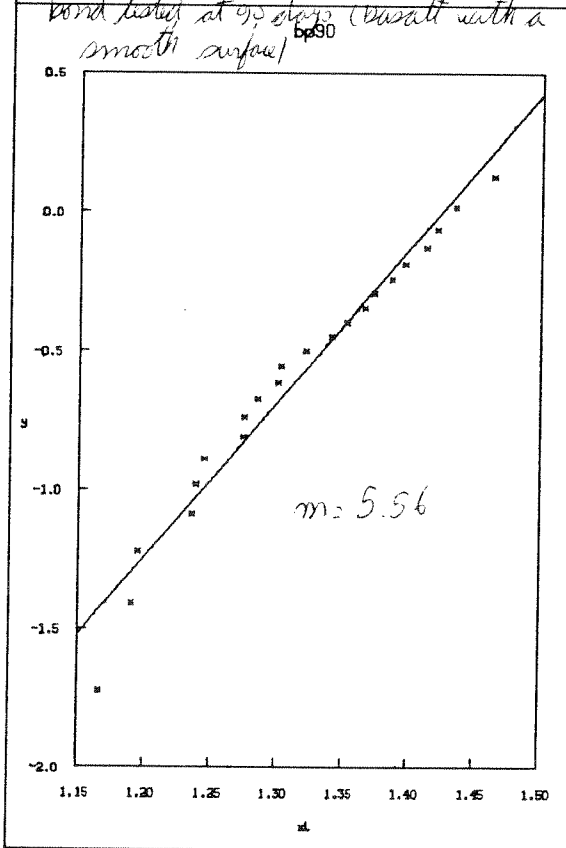
bond tested at 28 days (basalt with a sand-blasted surface)



bond tested at 28 days (basalt with a smooth surface)



bond tested at 90 days (basalt with a smooth surface)



bond tested at 28 days (concrete-glass with a sand-blasted surface)

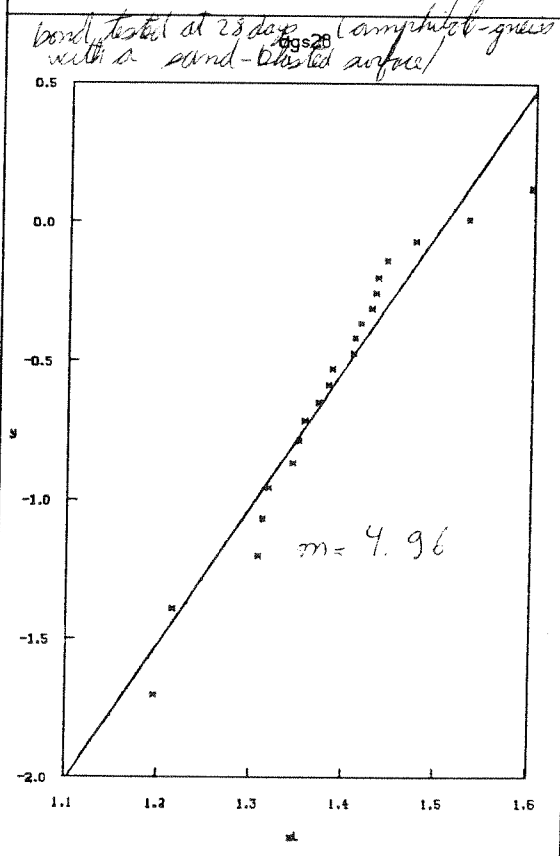


Fig 13
Plot to obtain wellbore parameter

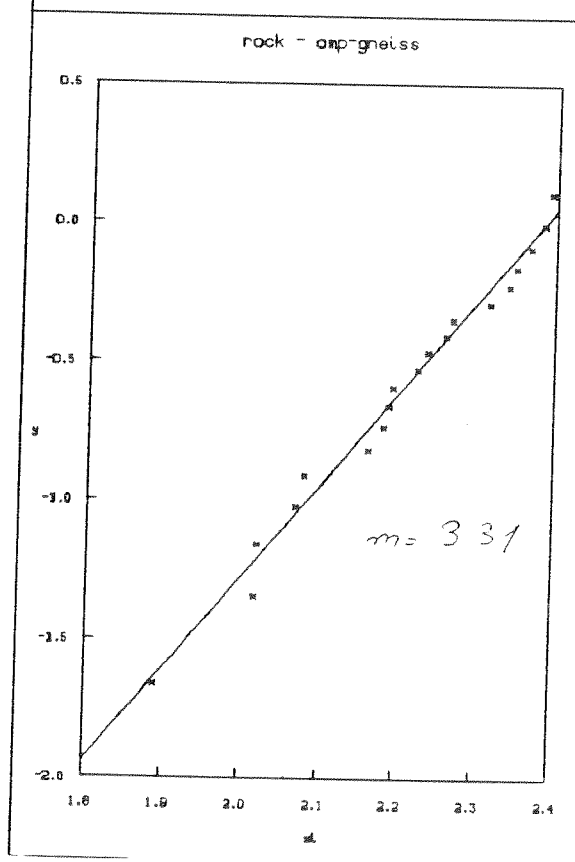
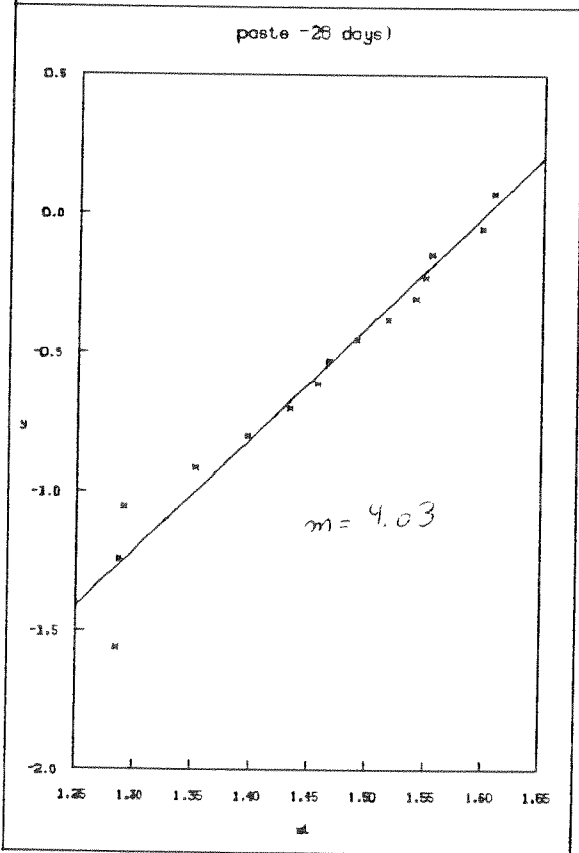
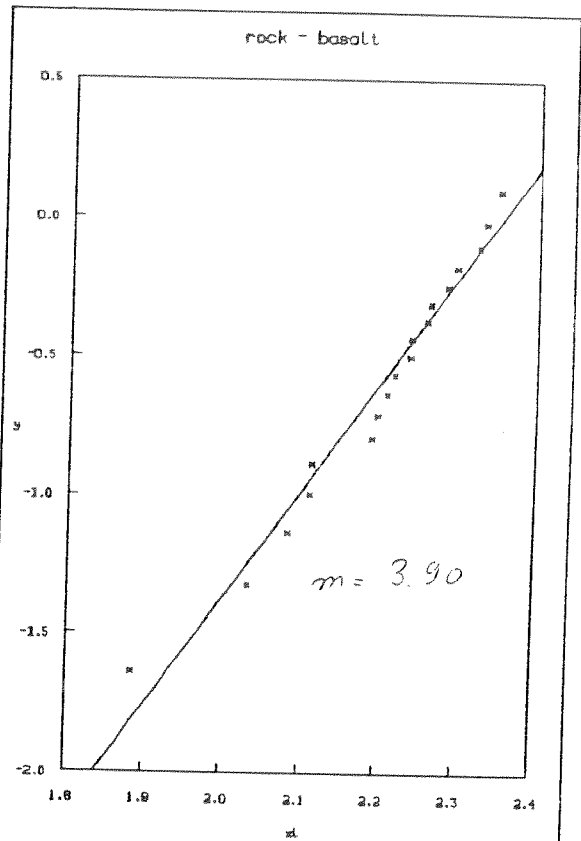
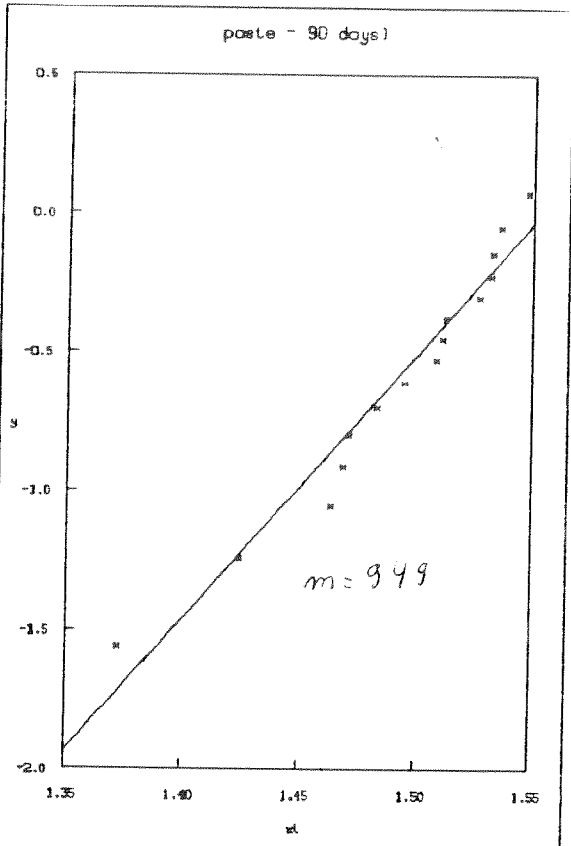


Fig 18D
 plot to obtain Weibull parameters

concrete at early ages is diagrammatically represented in Fig. 4.19. In chapter 3 it was emphasized that the through-solution mechanism of hydration is the most logical model to explain the crystal structure present in the transition zone. By this model, the cement grains dissolve to originate ions that can easily migrate in the higher water paste around the aggregate. These ions precipitate larger crystals with a better developed morphology than the matrix because in the transition zone there is more space available for their growth due to a higher porosity. The calcium hydroxide crystals are formed with a preferential way, with the c-axis perpendicular to the aggregate surface.

Now let us expose the concrete element to mechanical, thermal and hygrometrical loads. The overall behavior will depend on the properties of the three phases existing: the aggregate, the matrix and the transition zone between them. Usually the aggregate and the matrix have different mechanical and thermal properties which will induce stress concentrations on the interface, which is unfortunately the weakest phase; therefore most of the cracks will originate on the transition zone. This type of crack is usually referred in the literature as microcracks, and Fig. 4.20 shows a schematic path of this crack for a non-reactive aggregate at early ages. The microcrack will tend to propagate over the higher porosity zone at early ages. At later ages, however this zone is filled with hydration products and the fracture path will mostly pass through the CH film. Fig 4.21 shows that the crack plane for CH crystal on the interface is perpendicular to the c-axes. When a carbonate rock is used there is a chemical bond between the aggregate and the matrix, improving the characteristics of the transition zone and consequently the mechanical properties of the concrete. Fig 4.22 shows a microcrack path for such aggregate and it can be seen that the transition zone may not be the weakest phase and the mineralogy of the aggregate such the existence of cleavage planes may control the cracking pattern.

At this point it is interesting to speculate on how to improve the aggregate-

UNLOADED CONCRETE SPECIMEN

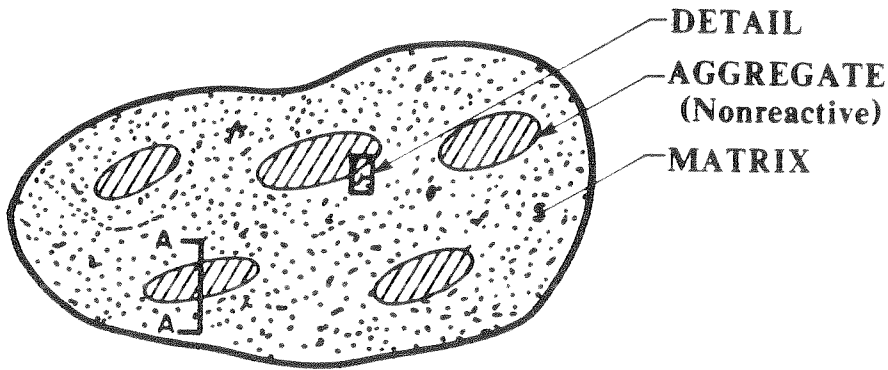
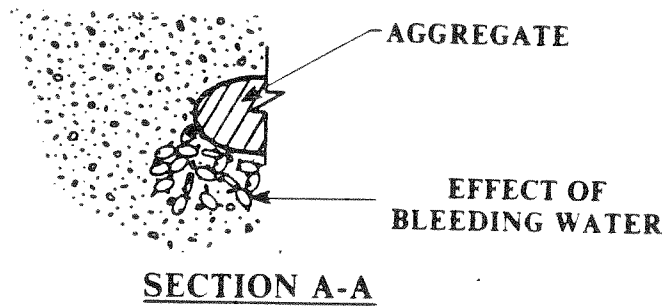
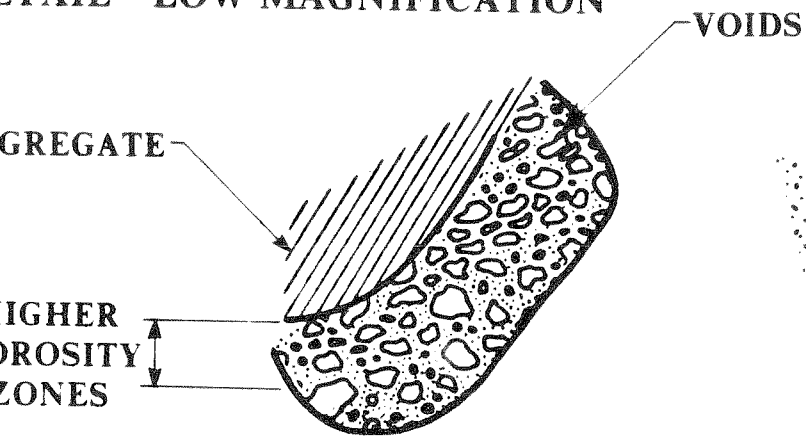
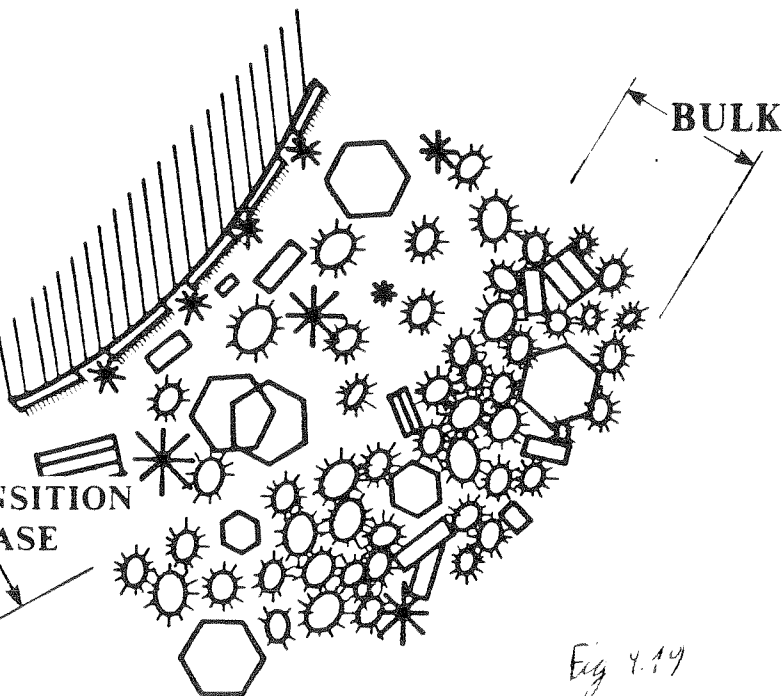


Fig. 4.19

DETAIL - LOW MAGNIFICATION



DETAIL - HIGHER MAGNIFICATION







-  C A S H
-  Ca(OH)₂
-  C S H
-  CEMENT GRAIN

Fig 4.19

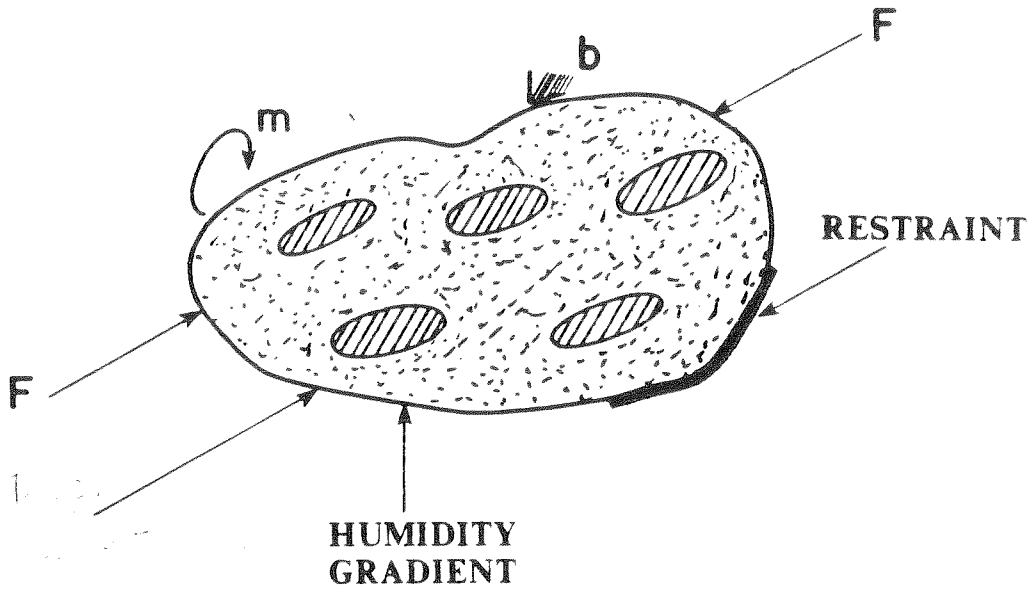


Fig 4.20

I) EARLY AGES

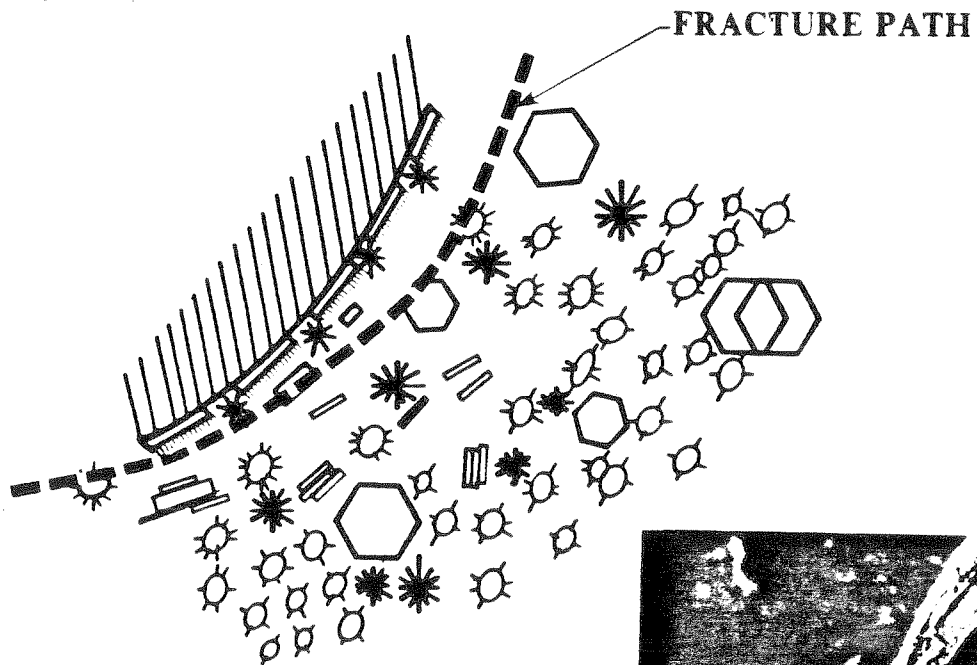
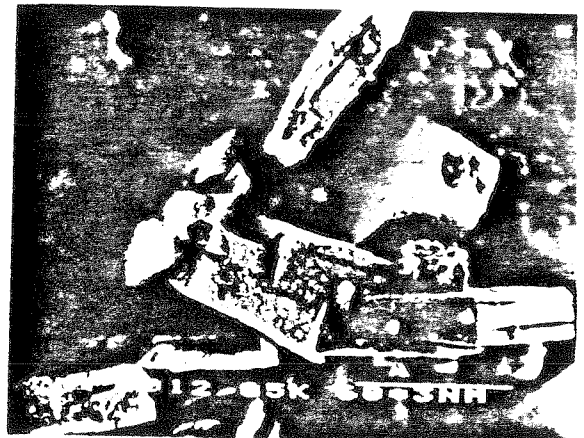


Fig. 4.20



Crack on the LV specimen at 100
psi

II) LATER AGES

(Reactive Aggregate)

FRACTURE PATH

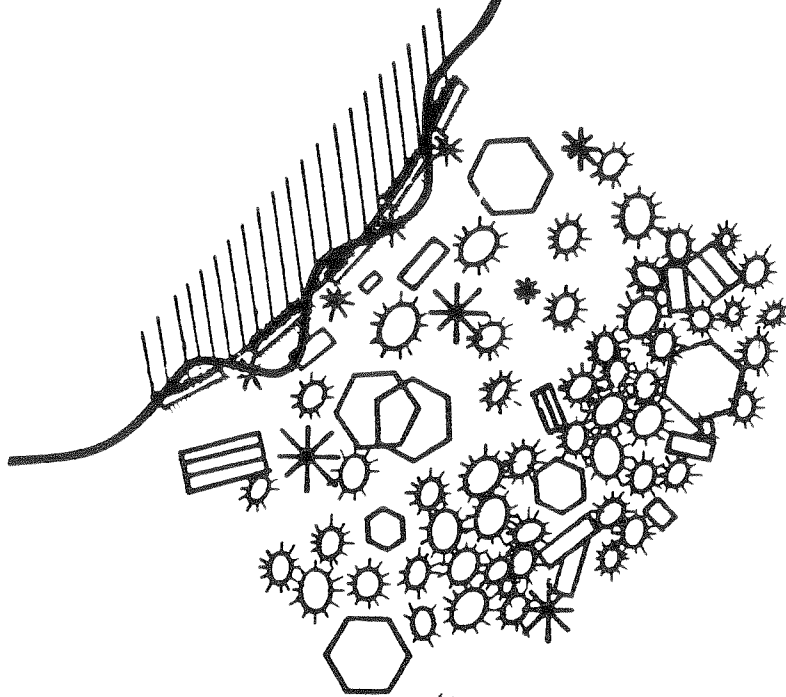


Fig 4.27

II) LATER AGES

(Inert Aggregate)

FRACTURE PATH

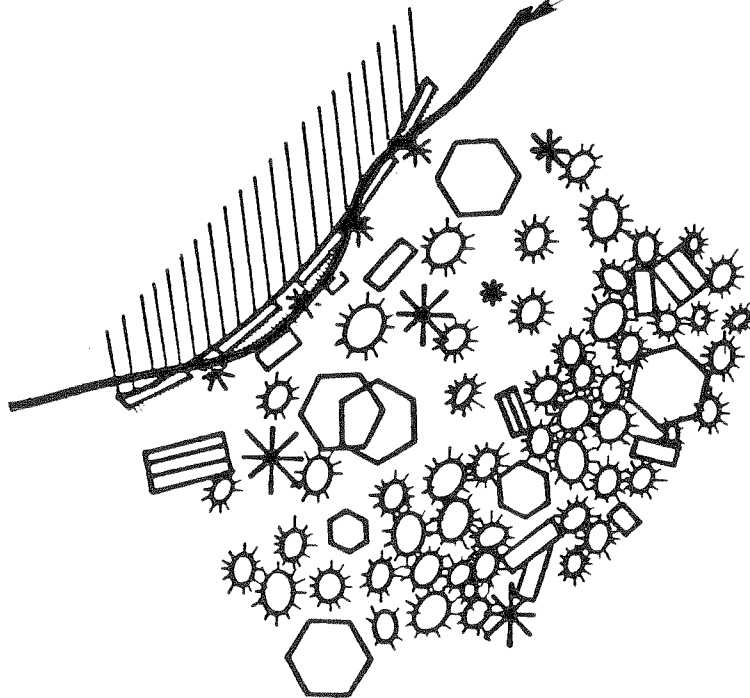


FIG. 32 Fig 4.28

cement paste bond. It was shown that the hydration products crystal size and concentration have a major rule on the transition zone. Metallurgists have been improving and controlling the quality of their products for years by having the knowledge of the crystal size effect on the mechanical behavior. For the concrete technologist this is still a farfetched ambition, however some important qualitative trends can already be established. In the case of the expansive cement, for instance it was suggested that the increase of mechanical strength of concrete was caused by a crystal refinement of the calcium hydroxide in combination with a higher concentration of ettringite in the transition zone. The use of silica fume besides reducing the bleeding acts as a activating site for hydration which causes an overall densification and crystal refinement in the matrix and in particular in the transition zone. The bond improvement obtained when carbonate rocks are can also be considered as a case of crystal refinement because the dissolution and reprecipitation of calcium carboante originates a network of smaller crystals.

4.6 References

- 4.1 Alexander K.M., Warlaw J. and Gilbert D.J., "Aggregate-Cement Bond, Cement Paste Strength, and the Strength of Concrete". *The Structure of Concrete*, The Cement and Concrete Association, pp. 59-81, London, 1968.
- 4.2 Stuble L., Skalny J. and Mindess S., "A Review of the Cement-Aggregate Bond". *Cement and Concrete Research*, 10, 277, 1980.
- 4.3 Johnson J.B., *The Materials of Construction*. First Edition, John Willey & Sons, New York, 1877.
- 4.4 Gillmore Q.A., *A Practical Treatise on Limes, Hydraulic Cements and Mortars*. Van Nostrand, New York, 1864.
- 4.5 Wheeler, as quoted by Johnson (4.3) pps. 597-599.

- 4.6 Lyubimova T. Yu and Pinus E.R., "Crystallization Structure in the Contact Zone between Aggregate and Cement in Concrete". Colloid J. USSR.
- 4.7 Skalny S. and Mindess S., "Physico-Chemical Phenomena at the Cement Paste-Aggregate Interface". Meeting on Reactivity of Solids, Dijon, France, 1984.
- 4.8 Ollivier J.P., *Personal Communication*.
- 4.9 Antis G.R., Chantikul P., Lawn B.R. and Marshall D.B., "A Critical Evaluation of Indentation Techniques for Measuring Fracture Toughness: I, Direct Crack Measurements". Journal of the American Ceramic Society, **64**, 1981.
- 4.10 Smith S.S., Magnusen P. and Pletka B.J., "Fracture Toughness of Glass Using the Indentation Fracture Technique". *Fracture Mechanics for Ceramics, Rocks and Concrete*. ASTM STP 745, 1981.
- 4.11 Lawn B.R. and Wilshaw T.R., Journal of Materials Science, **10**, 1049, 1975.
- 4.12 Chiang S.S., Marshall D.B. and Evans A.G., "A Simple Method for Adhesion Measurements". *Surfaces and Interfaces in Ceramic and Ceramic-Metal Systems*. Edited by J. Pask and A.E. Evans. Plenum Press, New York, 1981.
- 4.13 Hillemeier B. and Hilsdorf H.K., "Fracture Mechanics Studies on Concrete Compounds". Cement and Concrete Research, **7**, 1977.
- 4.14 Dundurs J., "Effect of Elastic Constants on Stress in a Composite Under Plane Deformation". J. Composite Materials, **1**, 310, 1967.
- 4.15 Bogy D.B., "Two Edge-Bonded Elastic Wedges of Different Materials and Wedge Angles Under Surface Traction". Journal of Applied Mechanics, **377**, 1971.
- 4.16 Bogy D.B., "On the Problem of Edge-Bonded Elastic Quarter-Planes Loaded at the Boundary". Int. J. Solid Structures, **6**, 1287, 1970.

- 4.17 Bogy D.B., 'The Plane Solution for Joined Dissimilar Elastic Semistrips Under Tension'. *Journal of Applied Mechanics*, 43, 1975.
- 4.18 Weibull W., *Ingenjörsvetenskapsakademiens Handl.*, No. 151, Stockholm.
- 4.19 Vardar O., 'Fracture of Brittle Solids under Multiaxial and Dynamic Loading'. Ph.D Thesis, University of California, Berkeley, 1975.
- 4.20 Vardar O. and Finnie I., 'An Analysis of the Brazilian Disk Fracture Test Using the Weibull Probabilistic Treatment of Brittle Strength'. *International Journal of Fracture*, 11, 1975.
- 4.21 Ratigan J.L., 'A Statistical Fracture Mechanics Approach to the Strength of Brittle Rock'. Ph.D. Thesis, University of California, Berkeley, 1981.
- 4.22 Valenta O., 'The Significance of the Aggregate-Cement Paste Bond for Durability of Concrete. International Symposium on the Durability of Concrete, RILEM, Prague, 1961.

CHAPTER 5

O

A GENERALIZED CONTINUUM THEORY FOR CONCRETE

5.1. Introduction

The composite nature of concrete has a very strong physical appeal because the macroscopic phases (rock particles dispersed in a porous matrix) can be seen by direct inspection. This fact inspired many researchers to model concrete as a two phase material. However, most of the available models oversimplified the reality, giving limited and sometimes questionable overall information. For instance, the classical approach of idealizing concrete as an elastic infinite matrix with a stiff spherical inclusion in order to explain the vertical cracks that develop during uniaxial compression does not model satisfactorily actual concrete, where particles interact with each other. A more satisfying approach is given by Ortiz and Popov (5.1), who modeled concrete as a two-phase interacting media and were able to derive general constitutive equations with the aid of thermodynamic potentials.

In this chapter, an intuitive formulation will be used to model concrete as consisted of granular particles dispersed in a porous matrix. This theory is based on formal arguments of continuum mechanics and it was originally proposed by Goodman and Cowin (5.2) for granular materials.

We will follow Deresiewicz (5.3) in understanding a porous material as "consisting of a continuous solid matrix which surrounds either isolated or interconnected voids filled with gas, liquid or a solid binder" and a granular material as "consisting of an aggregate of discrete, solid granules in contact". The voids between the granules may be filled with liquid or gas; if a binding element fills a part or all the voids, hold-

ing the granules in a fixed position as, for example, concrete and sandstone, we will call the material "porous-granular".

The motivation of this work is to present an unified formulation which permits to understand and predict the concrete behavior. The following research areas need a fairly comprehensive understanding of the thermomechanics response of concrete:

1. The Effect of the Microstructure on the Concrete Model

Most of the existing models for concrete are based exclusively on the phenomenological approach. While they may give a fair overall prediction of a specific behavior, much information on the internal behavior is lost.

The present model will introduce two extra variables that are not included in the traditional continuum mechanics: porosity and aggregate content.

The reason for selecting porosity is that it can model many important properties:

- a) aging effect: will produce a lower porosity due to hydration.
- b) aggregate-matrix bond: will cause a localized higher porosity due to the bleeding water and the growth of larger crystals in the interface (as it shown in chapter 2)
- c) cracking propagation: will cause an associated higher porosity related to the fracture process.

The introduction of the aggregate content will guarantee a granular behavior in concrete.

2. Constitutive Equations

Since the present model is based on the rational mechanics, it will produce an entropy inequality which associated to the Coleman's method permits to derive constitutive equations in a natural way. Therefore, elasticity, viscoelasticity and plasticity can be formulated from a very basic approach.

3. Fracture Mechanics of Porous-Granular Material

There is no acceptable fracture mechanics theory for concrete-like materials. Gjorv, Sorensen, Amesen (5.4) showed that cement paste is notch sensitive, mortar is less notch sensitive and concrete is very little notch sensitive. It is interesting to mention that one of the main problem in using the traditional fracture mechanics for concrete is its granular nature, where the aggregate acts as a crack arrestor, either because of the elastic mismatch or by a Gordon interface crack arrest mechanism; also there is not a defined crack tip for concrete, only a fracture zone where microcracks gradually change into cracks. Even though no specific formulation for crack propagation will be given, the present model is general enough to incorporate the fracture mechanics of concrete.

This chapter presents in section 2 a brief literature review that shows the evolution of the understanding of granular and porous materials. In section 3 the theory of generalized continuous media is discussed, in section 4 we derive the continuum theory for concrete.

5.2. Brief Literature Review

Coulomb in 1773 presented a yield criteria for granular materials, which states that slip on a plane happens when the shear acting on the plane is resisted by the cohesion of the material (adhérence) and a constant (the coefficient of internal friction) times the normal stress on the plane.

Dilatancy, the property of a material by which it increases in volume when sheared, was first scientifically studied by Reynolds in 1885, who coined the word. The mathematical theory of dilatancy in a modern tensor analysis was done by Reiner (5.5). This paper has had great influence in many subsequent work in rational continuum mechanics and it presented the fluid constitutive equation for the now called Reiner-Rivlin fluid.

Granular material was often modeled by representing the individual granules as spheres or other convex shapes in contact in regular arrays. In earlier works, Gassmann (5.6), the relation between the contact force and the displacement of the grains was based on Hertz's theory; with the development of the tangential component of the contact force theory due to Mindlin (5.7) and Mindlin and Deresiewicz (5.8) it was possible to include the tangential components of the forces at the contact between the grains. Duffy and Mindlin (5.9) give the stress-strain relations for the case of a medium composed of elastic spheres arranged in a face-centered cubic array.

The effect of inclusions in an elastic infinite medium has been analyzed by different approaches. For plane problems, the use of the theory of functions of a complex variable developed by Muskhelishvili (5.10) provides powerful methods for solving complex problems. Goodier (5.11) presented the solution for cylindrical inclusions and Edwards (5.12) for spheroidal inclusions.

Eshelby (5.13) studied the elastic field of an ellipsoidal inclusion that undergoes a change of shape and size in an infinite homogeneous isotropic elastic medium. He developed a clever process of imaginary cutting, straining and welding operations to solve the problem. We cut round the inclusion and remove it from the matrix; next we allow the unconstrained transformation to take place. Now we apply surface tractions such that restore the inclusion to its original form (note that the stress is zero in the matrix and constant in the inclusion). We consider the applied surface tractions as a layer of body force over the interface between the matrix and inclusion; so, finally, we should remove this layer of body force (this elastic field is found by integration from the expression for the elastic field of a point force).

Biot's (3.14-3.17) deformation theory of a porous elastic solid that contains a compressible fluid had a major influence in soil and rock mechanics. He considered the skeleton as purely elastic and the fluid compressible viscous, so his theory may be considered as a generalization of the theory of elasticity to porous materials. Macken-

zie (5.18) studied a porous material with spherical voids and computed the effective bulk and shear moduli of the material. Later on, Carrol and Holt (5.19) extended the Mackenzie's model to include dynamic effects, geometric nonlinearity and plastic yielding; they also developed a dynamic pore-collapse relation for elastic-plastic materials.

The effect of cracks on the properties of a material has been studied by Walsh (5.20-5.22). Defining the elastic constants of a body containing cracks and voids as the effective elastic constants of the body and intrinsic elastic constants to the material uninfluenced by these imperfections, Jaeger and Cook (5.23) give the following summary of such effects:

1. The effective Young's modulus of a body containing open cracks and cavities is less than the intrinsic Young's modulus of a solid body.
2. The effective Young's modulus of a body containing closed cracks is less than its intrinsic Young's modulus if the surfaces of the crack slide past one another.
3. The effective Poisson's ratio of a body containing very flat open cracks is less than its intrinsic Poisson's ratio.
4. The effective Poisson's ratio of a body containing closed cracks is greater than its intrinsic Poisson's ratio.

Green and Naghdi (5.24) give a dynamical theory of interacting continua which is applicable to deforming porous media. The theory is based on an energy equation and an entropy production inequality, together with the use of invariance requirements under superposed rigid body motions. Crochet and Naghdi (5.25) using this theory give the constitutive equations appropriate to flow of Newtonian viscous fluids through elastic media.

Manins and Roberts (5.26) dealt with the initial deformation of a liquid filled porous elastic medium in which the permeability is a function of the local deformation of the medium. They assumed for this problem the fluid as being incompressible

Newtonian Viscous and the medium material as incompressible. Goodman and Cowin (5.2) formulated a continuum theory of granular materials; and their work was extended by Jenkins (5.27), Passman (5.28), A hmadi and Sohrabpour (5.29), A hmadi (5.30, 5.31). The details of this theory will be given in section 4.

3. Generalized Continuous Media

We will refer to generalized continuum when the configuration of the model representing a material may be fully described by a certain number of variables that are not included in those used for the classical continuum of Cauchy.

There are many interesting situations in which we should use the generalized models of materials. An important example is the continuum originally developed by E. & L.F. Cosserat in which each point of the continuous media has the six degrees of freedom of a rigid body (in classical elasticity a material point has only the three degrees of freedom corresponding to its position in the Euclidean space). Eriksen and Truesdell (5.32) showed that the orientation of a given point of such media can be represented by the values of three mutually perpendicular vectors called the directors of an oriented medium and as Toupin (5.33) points out, now it is natural to consider the generalization in which the three directors are stretchable and not constrained to remain mutually orthogonal (5.34).

The continuum of Cauchy assumes that the body can be divided into small subbodies of the continuum. Therefore, the configuration of the subbodies is described by the position of their center of mass and which velocity (when smoothed out), form the macroscopic velocity field of the continuum. However, a body may have microstructure, that is, the character of the body changes when the subbodies become smaller than a minimum size; so the smoothing process must take place at the level of the minimal subbody that may be too large to be regarded as a simple particle. This minimal subbody may be considered as a microcontinuum with a velocity distribution

and the method of virtual power developed by Germain may be used to determine the force system on the body as a whole, by integrating the force acting on the velocity field within the microcontinuum, Lubliner (5.35). If the velocity distribution in the microcontinuum is determined by derivatives of the macroscopic velocity field, then the continuum is called a simple multipolar continuum (dipolar if only first derivatives appear).

Mindlin (5.36) presented the mechanics of elastic media with microstructure. He introduced the concept of unit cell which can be interpreted as a molecule of a polymer, a crystal lattice or a grain of a granular material. The unit cell model yields the same results of the deformable director for linear problems and if the unit cell is rigid the formulation reduces to those of a linear Cosserat continuum.

We will show in section 4 that the continuum theory for granular materials may be considered as a particular solution of the microstructure theory where only the dilation of the micromedium is considered. Green and Rivlin (5.37) developed the theory of multipolar continuum mechanics in which Mindlin's theory may be considered a particular case.

The theory presented by Goodman and Cowin (5.2) for describing the mechanics of granular materials will be the only generalized theory that will be discussed in detail in the next section, because the present model for concrete can be considered as a natural extension of the model. This formulation has been called "volume fraction theory" because it introduces the volume fraction of the material as an additional independent kinematic variable.

This formulation has been used to mixtures of granular materials by Passman (5.28), to the propagation of waves in granular materials by Nunziato and Walsh (5.38), to the static equilibrium of a granular material by Jenkins (5.27); to flows of granular materials by Passman et al. (5.39) and Nunziato et al. (5.40); to porous materials by Nunziato and Cowin (5.41,5.42), Passman (5.43), Ahmadi and

Shahinpoor (5.29); to the bubbly fluid as a continuum with microstructure by Capriz and Cohen (5.44).

5.4. The Goodman-Cowin Continuum Theory for Porous and Granular Materials

Goodman and Cowin (5.2) introduced the concept of distributed body to analyze the distribution of solid constituent in porous and granular materials.

Considering that B_t is the configuration of the distributed body at time t ; V_t and M_t are the distributed volume and distributed mass respectively; V is the Lebesgue volume measure. Assuming that V_t is absolutely continuous with respect to the Lebesgue volume measure V , so by the Radon-Nikodym theorem, there exists a real valued Lebesgue integrable function $\nu(x_i, t)$ defined on B_t such that:

$$V_t(P_t) = \int_{P_t} \nu dV \quad (4.1)$$

ν is called the volume distribution function (ν is related to the porosity n or the void ratio e by $\nu = 1 - n = \frac{1}{1 + e}$)

Originally the model assumed that M_t is absolutely continuous with respect to V_t . It implies that the mass of a distributed body is only associated with the distributed volume V_t and not the void volume $V - V_t$. That means the void of a porous or granular material can be neglected. This is justified if we are only interested in the behavior of the bulk material; because it excludes the possibility of studying the permeability and fluid flow of porous and granular materials, once it neglects the void mass. A natural extension of this theory would be consider the void mass; this work has been done by Ahmadi (5.30).

Using the same arguments we define an integrable function on B_t such that:

$$M_t(P_t) = \int_{P_t} \gamma dV_t \quad (4.2)$$

The function γ is called the distributed mass density. The mass $M_t(P_t)$ can also

be expressed as:

$$M_t(P_t) = \int_{P_t} \gamma \nu dV \quad (4.3)$$

where the function $\rho (= \gamma \nu)$ is the classical mass density function.

It should be mentioned that Bedford and Drumheller (5.45 - 5.48) presented a theory for immiscible mixtures, which has been applied to liquids containing distributions of particles, bubbly liquids and fluid-saturated porous media. In their theory they used the local density of the constituents as independent kinematic variables. The local density ρ' is related to the partial density ρ (the mass of the constituent per unit spatial volume) by equation 4.4.

$$\rho' = \frac{\rho}{\nu} \quad (4.4)$$

One wonders if it makes any difference at all if we use the Goodman-Cowin volume fraction ν or the the Bedford-Drumheller local density ρ' , if they are related by a simple expression as equation 4.4. In a recent paper, Bedford and Drumheller (5.49) proved that the two formulations are not equivalent and ,even more important, in the general case of studying the inertia associated with the dilatational motion of discretized material we need both ν and ρ' (or using equation 4.4, any two of the variables ν, ρ, ρ'). For this class of continuum theory they define " volume fraction theory "

Bedford and Drumheller (5.49) showed that the inertia associated with the expansion and contraction of the individual grains can be expressed in terms of ρ' . The inertia associated with the dilatation motion of the grains relative to one another can be expressed in terms of ρ . Therefore, the total dilatational inertia requires both ρ' and ρ (or ν if we use equation 4.8). In that sense, both Goodman-Cowin and Bedford-Drumheller's theory should be considered as special cases of a general theory. Bedford and Drumheller (5.49) generalized the Goodman-Cowin theory using the two variables ρ' and ρ to express the dilatational inertia of the material. They showed that

the general results yield the ones obtained by Goodman and Cowin when the grains are considered to be incompressible (ρ' constant).

5.4.1 Kinematics

The motion of a distributed body relative to the time t_0 is the mapping $\chi_i^{t_0}$ from the product set $B_{t_0} \times (-\infty, \infty)$ into Euclidean three space. The velocity $u_i(X_A, t)$, and the acceleration $a_i(X_A, t)$ of the material point is given by:

$$u_i(X_A, t) = \frac{\partial}{\partial t} \chi_i^{t_0}(X_A, t) \quad (4.5)$$

$$a_i(X_A, t) = \frac{\partial^2}{\partial t^2} \chi_i^{t_0}(X_A, t) \quad (4.6)$$

The deformation gradient $F_{iA}(X_B, t)$ is given by :

$$F_{iA}(X_B, t) = \frac{\partial}{\partial X_A} \chi_i^{t_0}(X_B, t) \quad (4.7)$$

and the velocity gradient $L_{ij}(X_k, t)$ is defined by :

$$L_{ij}(x_k, t) = \frac{\partial}{\partial x_j} u_i(\chi_B^{t_0^{-1}}(x_k, t), t) \quad (4.8)$$

Considering dV_0 an element of the total volume in the reference configuration and dV its image under motion $\chi_i^{t_0}$, their relationship is given by :

$$dV = J dV_0 \quad (4.9)$$

where:

$$J = |\det F_{iA}| \quad (4.10)$$

Using equations 4.1 and 4.14 the following transformations can be easily obtained:

$$dV_t = \nu dV \quad (4.11)$$

$$dV_{t_0} = \nu_0 dV_0 \quad (4.12)$$

$$dV_t = \frac{\nu}{\nu_0} J dV_{t_0} \quad (4.13)$$

When the motion is isochoric $J = 1$ and the distributed body is non-dilatant, otherwise, it is dilatant.

Using equation (4.13) we can see that the incompressible distributed volume constraint is given by:

$$\frac{\nu}{\nu_0} J = 1 \quad (4.14)$$

It should be noted that during a rigid-body motion, the generalized body model is still described by six degrees of freedom. In such motion, the number of additional degrees of freedom is irrelevant. For instance, in a granular continuum where the grains are permitted to spin or deform independently, during a rigid-body motion, the grains will deform and will remain attached to one another.

5.4.2 Thermodynamic Processes

Goodman and Cowin (5.2) postulated a conservation law for the higher order forces associated with the volume distribution. They defined a stress tensor T_{ij} , body force b_i , specific energy ε , heat flux vector q_i , heat supply r , specific entropy η , entropy flux vector Φ_i , temperature Θ , equilibrated inertia k , equilibrated stress vector h_i , external equilibrated body force l and intrinsic equilibrated body force g .

A process G for a distributed body $\{B_t\}$ with a motion χ_i^t is defined as the set:

$$G = \chi_i^t, \gamma, T_{ij}, b_i, \varepsilon, q_i, r, \eta, \Phi_i, \Theta, k, h_i, l, g \quad (4.15)$$

The process G is called a thermodynamic process if the elements of G satisfy the following balance relations:

Balance of Energy

$$\begin{aligned} \frac{d}{dt} \int_{P_t} \gamma \nu \left(\varepsilon + \frac{1}{2} u_i u_i + \frac{1}{2} k i i \right) dV = \\ = \int_{\partial P_t} (T_{ij} u_i + h_j \nu - q_j) n_j dA + \int_{P_t} \gamma \nu (b_i u_i + l \nu + r) dV \end{aligned} \quad (4.16)$$

Entropy Inequality

$$\frac{d}{dt} \int_{P_t} \gamma \nu \eta dV \geq - \int_{\partial P_t} \Phi_i n_i dA + \int_{P_t} \gamma \nu \frac{r}{\Theta} dV \quad (4.17)$$

Balance of Equalibrated Force

$$\frac{d}{dt} \int_{P_t} \gamma \nu k \dot{\nu} dV = \int_{\partial P_t} h_i n_i dA + \int_{P_t} \gamma \nu (l+g) dV \quad (4.18)$$

Balance of Equalibrated Inertia

$$\frac{d}{dt} \int_{P_t} \gamma \nu k dV = 0 \quad (4.19)$$

One should note that the conservation of energy shows power terms associated with $\dot{\nu}$, that is so because ν is kinematically independent of the motion χ_i^b and the temperature. Similar terms appear in the theory of microstructure discussed in section 3.

In a later work, Nunziato and Cowin criticized the balance of equalibrated inertia, equation (4.19) using the argument that one should expect physically that the equalibrated inertia k should depend on the geometrical features of the voids because the kinetic energy associated with the void volume change is $\frac{1}{2} \rho k \dot{\nu}^2$. Therefore, it would be more realistic to assume that k is given by an equation in which it depends on the volume fraction.

Invoking the principle of material objectivity and arguments used by Noll we can get the balance relations for mass, linear momentum and angular momentum.

$$\dot{\gamma} \nu + \gamma \nu u_{i,i} = 0 \quad (4.20)$$

$$\gamma \nu \dot{u}_i = T_{ij,j} + \gamma \nu b_i \quad (4.21)$$

$$T_{ij} = T_{ji} \quad (4.22)$$

Manipulating the above equations and the balance relations we get:

$$\gamma \nu k \dot{\nu} = h_{i,i} + \gamma \nu (l+g) \quad (4.23)$$

$$\gamma \nu \dot{\varepsilon} = T_{ij} D_{ij} + h_i (\dot{\nu})_{,i} - \gamma \nu g \dot{\nu} - q_{i,i} + \gamma \nu r \quad (4.24)$$

$$\gamma \nu \dot{\rho} \geq -\Phi_{i,i} + \gamma \nu \frac{r}{\Theta} \quad (4.25)$$

Introducing the free energy

$$\Psi = \varepsilon - \eta \Theta \quad (4.26)$$

And the extra entropy flux

$$k_i = \Phi_i - \frac{q_i}{\Theta} \tag{4.27}$$

We have

$$-\gamma\nu(\dot{\psi} + \rho\dot{\Theta}) + T_{ij}D_{ij} + h_i(\dot{v})_i - \gamma\nu g\dot{v} + \Theta k_{i,i} - \frac{q_{i,i}}{\Theta} \geq 0 \tag{4.28}$$

5.5. Continuum Theory for Concrete

In this section, the balance equations for a porous-granular material are developed. Ahmadi (5.29,5.30) developed a continuum theory for fully saturated porous and granular materials (two phase systems). The extension for porous-granular materials (three phase systems: granules, matrix and voids) is easy. The analysis of a fully saturated porous-granular is performed in section 5.1 by including fluid in the system.

Let us decompose the volume distribution ν , into ν^g and ν^m referring to the granules and matrix, respectively.

$$\nu = \nu^g + \nu^m \tag{5.1}$$

The mass densities of the granules and matrix will be denoted ρ^{g*} and ρ^{m*} , respectively. The masses of the granules and matrix in a porous-granular body P_t are given by:

$$M^g = \int_{P_t} \nu^g \rho^{g*} dV \tag{5.2}$$

$$M^m = \int_{P_t} \nu^m \rho^{m*} dV \tag{5.3}$$

The total mass of P_t is given by:

$$M = M^g + M^m \tag{5.4}$$

It is convenient to define:

$$\rho^g = \nu^g \rho^{g*} \quad \text{and} \quad \rho^m = \nu^m \rho^{m*} \tag{5.5}$$

Which we interpret as the bulk densities of the granules and the matrix, respec-

tively. The total bulk density of the material is given by:

$$\rho = \rho^g + \rho^m \quad (5.6)$$

As discussed in section 4.2, the following balance equations apply:

Conservation of Mass

$$\text{Granules} \quad \frac{\partial \rho^g}{\partial t} + \nabla \cdot (\rho^g v^g) = 0$$

$$\text{Matrix} \quad \frac{\partial \rho^m}{\partial t} + \nabla \cdot (\rho^m v^m) = 0$$

Balance of Linear Momentum

$$\text{Granules} \quad \rho^g \frac{dv_i^g}{dt} = t_{i,j}^g + \rho^g b_i^g + p_i^g$$

$$\text{Matrix} \quad \rho^m \frac{dv_i^m}{dt} = t_{i,j}^m + \rho^m b_i^m + p_i^m$$

Balance of Angular Momentum

$$\text{Granules} \quad t_{ij}^g = t_{ji}^g$$

$$\text{Matrix} \quad t_{ij}^m = t_{ji}^m$$

Balance of Equilibrated Force

$$\text{Granules} \quad \rho^g k^g \frac{dv^g}{dt} = h_{i,i}^g + \rho^g l^g + g^g$$

$$\text{Matrix} \quad \rho^m k^m \frac{dv^m}{dt} = h_{i,i}^m + \rho^m l^m + g^m$$

Conservation of Energy

$$\text{Granules} \quad \rho^g \dot{e}^g = t_{i,j}^g v_{i,j}^g + h_k^g v_{i,k}^g + q_{k,k}^g + \rho^g r^g - g^g v^g - p_k^g v_k^g$$

$$\text{Matrix} \quad \rho^m \dot{e}^m = t_{i,j}^m v_{i,j}^m + h_k^m v_{i,k}^m + q_{k,k}^m + \rho^m r^m - g^m v^m - p_k^m v_k^m$$

Entropy Inequality

$$\rho^m \Theta^m v^m + \rho^g \Theta^g v^g - \Theta^m \left(\frac{q_k^m}{\Theta^m} \right)_{,k} - \Theta^g \left(\frac{q_k^g}{\Theta^g} \right)_{,k} - \rho^m r^m - \rho^g r^g \geq 0$$

The balance of equilibrated force can be considered as a special case of an equa-

tion that arises for materials with microstructure, such as the ones described in section 3. Cowin and Nunziato (5.42) pointed out that having the microstructure theory as framework, the terms g^j and $h_{i,i}$ of the balance of equilibrated force can be identified with singularities in the classical linear elasticity known as double force systems without moments. We may combine three double forces without moment along three mutually perpendicular axes and the singularity may be described as a "center of compression" or "center of dilatation". Various singularities of this type are discussed in section 132 of Love's book (5.50). An example of this singularity would be an ellipsoidal inclusion that undergoes a change of size in an infinite homogeneous isotropic elastic medium; a solution for this problem was presented by Eshelby (5.13) as discussed in section 2. Both g^j and $h_{i,i}$ can be related to centers of dilation, while the equilibrated stress vector h_i may be related to a single double force system without moment. For granular materials, Jenkins (5.27) mentioned that the term ρl can have the physical meaning of an externally controlled pore pressure, and the reason for that in the general case is because ρl can be related to a force system like a center of dilation, however one which is externally controllable.

The free energies are defined by:

$$\psi^g = e^g - \eta^g \Theta^g \quad (5.7)$$

$$\psi^m = e^m - \eta^m \Theta^m \quad (5.8)$$

Combining with the entropy inequality we have:

$$-\rho^m (\dot{\psi}^m + \eta^m \dot{\Theta}^m) + q_k^m \Theta_{,k}^m / \Theta^m + t_{ik}^m d_{ik}^m + h_k^m v_{i,k}^m - g^m v^m - p_k^m v_k^m - \rho^g (\dot{\psi}^g + \eta^g \dot{\Theta}^g) + q_k^g \Theta_{,k}^g / \Theta^g + t_{ik}^g d_{ik}^g + h_k^g v_{i,k}^g - g^g v^g - p_k^g v_k^g \geq 0 \quad (5.9)$$

$$C_{ik} = \frac{1}{2} (u_{i,k} + u_{k,i}) \quad (5.10)$$

$$d_{ik} = \frac{1}{2} (u_{i,k} - u_{k,i}) \quad (5.11)$$

The derivation is fairly general, it only neglects the energy interaction between the granules and the matrix.

5.5.1 Laws of Motion and Thermodynamic Processes for Fully Saturated Concrete.

In the last section the basic laws of motion for concrete were derived. However, it should be mentioned that it was valid for the behavior of the bulk material and once it neglects the void mass it excludes the possibility of studying the permeability and fluid flow. This section shows how to take the fluid in account. Let us decompose the volume distribution ν , into ν^g , ν^m and ν^f referring to the granules, matrix and fluid, respectively.

The mass densities of the granules, matrix and fluid will be denoted ρ^{g*} , ρ^{m*} and ρ^{f*} , respectively. The mass of the fluid in a saturated-concrete body P_t are given by:

$$M^f = \int_{P_t} \nu^f \rho^{f*} dV \quad (5.12)$$

The total mass of P_t is given by:

$$M = M^g + M^m + M^f \quad (5.13)$$

It is convenient to define:

$$\rho^f = \nu^f \rho^{f*} \quad (5.14)$$

The total bulk density of the material is given by:

$$\rho = \rho^g + \rho^m + \rho^f \quad (5.15)$$

The balance equation derived in the previous sections are valid and should be added the corresponding contribution of the fluid.

The entropy inequality would be given by:

$$\begin{aligned} \rho^m \Theta^m i^m + \rho^g \Theta^g i^g + \rho^f \Theta^f i^f - \Theta^m \left(\frac{q_k^m}{\Theta^m} \right)_{,k} \\ - \Theta^g \left(\frac{q_k^g}{\Theta^g} \right)_{,k} - \Theta^f \left(\frac{q_k^f}{\Theta^f} \right)_{,k} - \rho^m \tau^m - \rho^g \tau^g - \rho^f \tau^f \geq 0 \end{aligned} \quad (5.16)$$

Defining,

$$\psi^f = e^f - \eta^f \Theta^f \quad (5.17)$$

We have the inequality:

$$-\rho^m (\dot{\psi}^m + \eta^m \dot{\Theta}^m) + q_k^m \Theta^m_{,k} + t_{ki}^m a_{ik}^m + h_{ki}^m v_{,k}^m - g^m i^m - p_k^m v_k^m - \quad (5.18)$$

$$\begin{aligned}
 & -\rho^g(\dot{\Psi}^g + \eta^g \dot{\Theta}^g) + q_k^g \Theta_{,k}^g / \Theta^g + t_{\alpha k}^g d_{\alpha k}^g + h_k^g v_{,k}^g - g^g v^g - p_k^g v_k^g - \\
 & -\rho^f(\dot{\Psi}^f + \eta^f \dot{\Theta}^f) + q_k^f \Theta_{,k}^f / \Theta^f + t_{\alpha k}^f d_{\alpha k}^f + h_k^f v_{,k}^f - g^f v^f - p_k^f v_k^f \geq 0
 \end{aligned}$$

Since we are dealing with a fully saturated media, we have the following constraint:

$$v^g + v^m + v^f = 1 \quad (5.19)$$

It should be noted that we are dealing with regular tensor notation. We have that:

$$v^g = \frac{\partial v^g}{\partial t} + v_k^g v_{,k}^g \quad (5.20)$$

$$v^m = \frac{\partial v^m}{\partial t} + v_k^m v_{,k}^m \quad (5.21)$$

$$v^f = \frac{\partial v^f}{\partial t} + v_k^f v_{,k}^f \quad (5.22)$$

Combining with the previous constraint (5.19), gives:

$$v^g + v^f + v^m - v_{,k}^g v_{,k}^g - v_{,k}^f v_{,k}^f - v_{,k}^m v_{,k}^m = 0 \quad (5.23)$$

The consequence of the constraint on the constitutive equation will be analyzed by using the method of the Lagrangian multiplier, suggested by Truesdell and Noll (5.51); Green, Naghdi and Trapp (5.52).

Multiplying the Lagrangian multiplier function $\Lambda(x, t)$ by the constraints (5.23) and adding to the inequality (5.18), it follows that:

$$\begin{aligned}
 & -\rho^m(\dot{\Psi}^m + \eta^m \dot{\Theta}^m) + q_k^m \Theta_{,k}^m / \Theta^m + t_{\alpha k}^m d_{\alpha k}^m + h_k^m v_{,k}^m - (g^m - \Lambda) v^m - p_k^m v_k^m - \\
 & -\rho^g(\dot{\Psi}^g + \eta^g \dot{\Theta}^g) + q_k^g \Theta_{,k}^g / \Theta^g + t_{\alpha k}^g d_{\alpha k}^g + h_k^g v_{,k}^g - (g^g - \Lambda) v^g - p_k^g v_k^g - \\
 & -\rho^f(\dot{\Psi}^f + \eta^f \dot{\Theta}^f) + q_k^f \Theta_{,k}^f / \Theta^f + t_{\alpha k}^f d_{\alpha k}^f + h_k^f v_{,k}^f - (g^f - \Lambda) v^f - p_k^f v_k^f - \Lambda (v_{,k}^g v_{,k}^g + v_{,k}^f v_{,k}^f + v_{,k}^m v_{,k}^m) \geq 0
 \end{aligned} \quad (5.24)$$

5.5.2 Constitutive Equations

The equations 5.1 to 5.11 apply for any mixture of two materials, where no chemical interaction between them takes place. To specialize the theory for concrete, modeled as a mixture of porous and granular materials, adequate constitutive postulates should be given. In this section, the bulk material (no fluid flow) will be analyzed.

The following independent constitutive variables are postulated for the distributed matrix:

$$\{S^m\} = \{\nu^m, \nu_{,i}^m, \dot{\nu}^m, \Theta^m, \Theta_{,i}^m, C_{ij}^m, \dot{C}_{ij}^m, u_i^m\}$$

And for the aggregates:

$$\{S^g\} = \{(\rho^g)^{-1}, \nu^g, \nu_{,i}^g, \dot{\nu}^g, \Theta^g, \Theta_{,i}^g, u_{,i}^g, \dot{C}_{ij}^g, u_i^g\}$$

The following constitutive equations (5.25) are postulated:

$$\begin{aligned} \Psi^m &= \Psi^m(\{S^m\}, u_{,i}^m) & \Psi^g &= \Psi^g(\{S^g\}, u_{,i}^g) \\ \eta^m &= \eta^m(\{S^m\}, u_{,i}^m) & \eta^g &= \eta^g(\{S^g\}, u_{,i}^g) \\ t_{ij}^m &= t_{ij}^m(\{S^m\}, u_{,i}^m) & t_{ij}^g &= t_{ij}^g(\{S^g\}, u_{,i}^g) \\ h_k^m &= h_k^m(\{S^m\}, u_{,i}^m) & h_k^g &= h_k^g(\{S^g\}, u_{,i}^g) \\ p_k^m &= p_k^m(\{S^m\}, (\{S^g\})) & p_k^g &= p_k^g(\{S^m\}, (\{S^g\})) \\ g_k^m &= g_k^m(\{S^m\}, (\{S^g\})) & g_k^g &= g_k^g(\{S^m\}, (\{S^g\})) \\ q_k^m &= q_k^m(\{S^m\}, (\{S^g\})) & q_k^g &= q_k^g(\{S^m\}, (\{S^g\})) \end{aligned}$$

A thermodynamic process is said to be admissible for concrete if the constitutive equations (5.25) are satisfied.

Incorporating the functional dependence of Ψ^m and Ψ^g expressed in (5.25) into the inequality (5.9) we have:

$$\begin{aligned} & -\rho^m \left[\frac{\partial \Psi^m}{\partial \Theta^m} + \eta^m \right] \dot{\Theta}^m - \rho^m \left[\frac{\partial \Psi^m}{\partial \Theta_{,i}^m} \dot{\Theta}_{,i}^m + \frac{\partial \Psi^m}{\partial C_{ij}^m} \dot{C}_{ij}^m + \frac{\partial \Psi^m}{\partial \dot{\nu}^m} \dot{\nu}^m + \frac{\partial \Psi^m}{\partial u_{,i}^m} \dot{u}_{,i}^m \right] + \quad (5.26) \\ & + \left[t_{kl}^m - \rho^g \frac{\partial \Psi^g}{\partial C_{kl}^m} \delta_{kl} + \rho^m \frac{\partial \Psi^m}{\partial \nu_{,k}^m} \nu_{,l}^m - \rho^m \frac{\partial \Psi^m}{\partial C_{kl}^m} \right] a_{kl}^m + \left[\rho^m \frac{\partial \Psi^m}{\partial \nu_{,k}^m} \nu_{,j}^m \right] v_{[j,k]}^m + \left[h_k^m - \rho^m \frac{\partial \Psi^m}{\partial \nu_{,k}^m} \right] \nu_{,k}^m \\ & - \left[\rho^m \frac{\partial \Psi^m}{\partial \nu^m} + g^m \right] \dot{\nu}^m - p_k^m u_k^m + q_k^m (\ln \Theta^m)_{,k} - \\ & - \rho^g \left[\frac{\partial \Psi^g}{\partial \Theta^g} + \eta^g \right] \dot{\Theta}^g - \rho^g \left[\frac{\partial \Psi^g}{\partial \Theta_{,i}^g} \dot{\Theta}_{,i}^g + \frac{\partial \Psi^g}{\partial C_{ij}^g} \dot{C}_{ij}^g + \frac{\partial \Psi^g}{\partial \dot{\nu}^g} \dot{\nu}^g + \frac{\partial \Psi^g}{\partial u_{,i}^g} \dot{u}_{,i}^g \right] + \\ & + \left[t_{kl}^g + \pi^g \delta_{kl} - \rho^m \frac{\partial \Psi^m}{\partial C_{kl}^g} \delta_{kl} + \rho^g \frac{\partial \Psi^g}{\partial \nu_{,k}^g} \nu_{,l}^g - \rho^g \frac{\partial \Psi^g}{\partial C_{kl}^g} \right] a_{kl}^g + \left[\rho^g \frac{\partial \Psi^g}{\partial \nu_{,k}^g} \nu_{,j}^g \right] v_{[j,k]}^g + \left[h_k^g - \rho^g \frac{\partial \Psi^g}{\partial \nu_{,k}^g} \right] \nu_{,k}^g - \\ & - \left[\rho^g \frac{\partial \Psi^g}{\partial \nu^g} + g^g \right] \dot{\nu}^g - p_k^g \nu_k^g + q_k^g (\ln \Theta^g)_{,k} \geq 0 \end{aligned}$$

Where $v_{[k,l]}$ is the antisymmetric part of the velocity gradient tensor $v_{k,l}$. The following definition was used:

$$\pi^g = -\frac{\partial \Psi^g}{\partial(\rho^g)^{-1}} \quad (5.27)$$

Also the assumption of small displacement was used:

$$\frac{d}{dt} u_{i,j} \approx u_{i,j} \quad (5.28)$$

Using the arguments given by Coleman and Noll (*), it follows that there exists at least one admissible thermodynamic process in which the values of $\dot{\Theta}^m, \dot{\Theta}_{,i}^m, \dot{\nu}^m, \dot{\nu}_{,k}^m, \dot{\nu}^m, \dot{C}_{ij}^m, \dot{C}_{ij}^m, \nu_{[ij]}^m, \dot{u}_k^m, \dot{\Theta}^g, \dot{\Theta}_{,i}^g, \dot{\nu}^g, \dot{\nu}_{,k}^g, \dot{\nu}^g, \dot{d}_{ij}^g, \dot{C}^g$ can be specified independently of any other term in the inequality. The entropy inequality then implies the following restrictions:

$$\eta^m = -\frac{\partial \Psi^m}{\partial \Theta^m} \quad (5.29)$$

$$\frac{\partial \Psi^m}{\partial \Theta_{,i}^m} = \frac{\partial \Psi^m}{\partial C_{ij}^m} = \frac{\partial \Psi^m}{\partial \nu^m} = \frac{\partial \Psi^m}{\partial u_i^m} = 0 \quad (5.30)$$

$$E h_k^m = \rho^m \frac{\partial \Psi^m}{\partial \nu_{,k}^m} \quad (5.31)$$

$$g^m = -\rho^m \frac{\partial \Psi^m}{\partial \nu^m} \quad (5.32)$$

$$E_{ij} \frac{\partial \Psi^m}{\partial \nu_{,k}^m} \nu_{,i} = 0 \quad (5.33)$$

$$E t_{kl}^m = \rho^g \frac{\partial \Psi^g}{\partial C_{kl}^g} \delta_{kl} - \rho^m \frac{\partial \Psi^m}{\partial \nu_{,k}^m} \nu_{,l}^m + \rho^m \frac{\partial \Psi^m}{\partial C_{kl}^m} \quad (5.34)$$

$$\eta^g = -\frac{\partial \Psi^g}{\partial \Theta^g} \quad (5.35)$$

$$\frac{\partial \Psi^g}{\partial \Theta_{,i}^g} = \frac{\partial \Psi^g}{\partial C_{ij}^g} = \frac{\partial \Psi^g}{\partial \nu^g} = \frac{\partial \Psi^g}{\partial u_i^g} = 0 \quad (5.36)$$

$$E h_k^g = \rho^g \frac{\partial \Psi^g}{\partial \nu_{,k}^g} \quad (5.37)$$

$$g^g = -\rho^g \frac{\partial \Psi^g}{\partial \nu^g} \quad (5.38)$$

$$E_{ij} \frac{\partial \Psi^g}{\partial \nu_{,k}^g} \nu_{,i} = 0 \quad (5.39)$$

$$E t_{kl}^g = -\pi^g \delta_{kl} + \rho^m \frac{\partial \Psi^m}{\partial C_{kl}^m} \delta_{kl} - \rho^g \frac{\partial \Psi^g}{\partial \nu_{,k}^g} \nu_{,l}^g + \rho^g \frac{\partial \Psi^g}{\partial C_{kl}^g} \delta_{kl} \quad (5.40)$$

$${}_D t_{kl}^m \nu_{,k}^m - p_k^m \nu_{,k}^m + q_k^m (tr \Theta^m)_{,k} + {}_D h_k^m \nu_{,k}^m + \quad (5.41)$$

$$+ {}_D t_{kl}^g \nu_{,k}^g - p_k^g \nu_{,k}^g + q_k^g (tr \Theta^g)_{,k} + {}_D h_k^g \nu_{,k}^g \geq 0$$

It should be mentioned that the stress tensor t_{kl} and the equilibrated stress vector

h_i were separated in the elastic (${}_E t_{kl}$ and ${}_E h_i$) and the dissipative (${}_D t_{kl}$ and ${}_D h_i$) components.

5.5.3 Linear Theory

As shown in the previous section, the specific entropies η^m and η^g , the elastic equilibrated stresses ${}_E h_i^m$ and ${}_E h_i^g$, the elastic part of the stresses ${}_E t_{ij}^m$ and ${}_E t_{ij}^g$ and the equilibrated body forces g^m and g^g are all derivable from the free energies Ψ^m and Ψ^g respectively.

Originally, Goodman and Cowin proposed the following definite free energy function for granular material:

$$\rho^g \Psi^g = \rho^g \Psi_g^g(\rho^g, \Theta^g) + \alpha_0 \nu^2 + \alpha \nu_k^g \nu_k^g \quad (5.42)$$

Where α_0 and α are material moduli, independent of ν . Later on, Jenkins (*) suggested that it would be more adequate to assume α depending on the porosity, i.e $\alpha = \alpha(\nu)$.

In this work the free energy for the aggregates will be the Goodman-Cowin free energy plus three extra terms to allow some coupling with the porous matrix. Of course, more complex versions of the free energy can be easily done, however for the present purposes the following equation is proposed:

$$\begin{aligned} \rho^g \Psi^g = & \rho^g \Psi_g^g(\rho^g, \Theta^g) + \frac{1}{2} \alpha_0^g (\nu^g)^2 + \alpha^g (\nu^g) \nu_k^g \nu_k^g + \\ & + \frac{1}{2} b_0^g u_{k,k}^g u_{k,k}^g + c_0^g u_{k,k}^g C_{ll}^m + \frac{1}{2} d_0^g C_{kk}^m C_{ll}^m \end{aligned} \quad (5.43)$$

And for the matrix,

$$\begin{aligned} \rho^m \Psi^m = & \frac{1}{2} \lambda^m C_{kk}^m C_{ll}^m + \mu^m C_{ki}^m C_{ki}^m + \frac{1}{2} \alpha_0^m (\nu^m)^2 + \alpha^m (\nu^m) \nu_k^m \nu_k^m + \\ & + \frac{1}{2} b_0^m u_{k,k}^m u_{k,k}^m + c_0^m u_{k,k}^m C_{ll}^g \end{aligned} \quad (5.44)$$

In order to that the free energy functions remain positive definite, the following restrictions should be satisfied:

$$\alpha_0^g \geq 0 \quad \alpha^g \geq 0 \quad (c_0^g)^2 \leq b_0^g d_0^g \quad (5.45)$$

$$\lambda^m \geq 0 \quad \mu^m \geq 0 \quad a_0^m \geq 0 \quad \alpha^m \geq 0 \quad (a_0^m)^2 \leq b_0^m \lambda^m \quad (5.46)$$

The constitutive equations become:

$$E t_{kl}^m = [(\lambda^m + d_0^g) u_{i,i}^m + (c_0^g + c_0^m) u_{i,i}^g] \delta_{kl} + \mu^m (u_{k,i}^m + u_{i,k}^m) - 2\alpha^m (\nu^m) \nu_{,k}^m \nu_{,l}^m \quad (5.47)$$

$$E h_k^m = 2\alpha^m (\nu^m) \nu_{,k}^m \quad (5.48)$$

$$g^m = -\frac{d\alpha^m(\nu^m)}{d\nu^m} \nu_{,k}^m \nu_{,k}^m - a_0^m \nu^m \quad (5.49)$$

$$E t_{kl}^g = [-\pi^g + (c_0^m + c_0^g) u_{i,i}^m + (b_0^m + b_0^g) u_{i,i}^g] \delta_{kl} - 2\alpha^g (\nu^g) \nu_{,k}^g \nu_{,l}^g \quad (5.50)$$

$$E h_k^g = 2\alpha^g (\nu^g) \nu_{,k}^g \quad (5.51)$$

$$g^g = -\frac{d\alpha^g(\nu^g)}{d\nu^g} \nu_{,k}^g \nu_{,k}^g - a_0^g \nu^g \quad (5.52)$$

CHECK

$$p_k^m = p_k^g = K(u_k^m - u_k^g) \quad (5.53)$$

Fourier's law can be used as a first approximation for the heat fluxes, therefore:

$$q_k^m = K^m \Theta_{,k}^m \quad q_k^g = K^g \Theta_{,k}^g \quad (5.54)$$

The equations of motion for concrete modeled as elastic inclusions (aggregate) in an elastic matrix are:

$$\rho^m u_i^m = (\lambda^m + d_0^g + \mu_m) u_{k,ki}^m + (c_0^g + c_0^m) u_{k,ki}^g + \mu_m u_{k,ki}^m - 2(\alpha^m (\nu^m) \nu_{,i}^m \nu_{,k}^m)_{,k} + K(u_k^m - u_k^g) + \rho^m b_i^m \quad (5.55)$$

$$\rho^m u_i^g = -\pi_{,i}^g + (c_0^m + c_0^g) u_{k,ki}^m + (b_0^m + b_0^g) u_{k,ki}^g - 2(\alpha^g (\nu^g) \nu_{,i}^g \nu_{,k}^g)_{,k} + K(u_k^m - u_k^g) + \rho^g b_i^g \quad (5.56)$$

$$\rho^m k^m \nu^m = 2\alpha^m \nu_{,kk}^m + \rho^m \nu^m - \frac{d\alpha^m(\nu^m)}{d\nu^m} (\nu^m) \nu_{,k}^m \nu_{,k}^m - a_0^m \nu^m \quad (5.57)$$

$$\rho^g k^g \nu^g = 2\alpha^g \nu_{,kk}^g + \rho^g \nu^g - \frac{d\alpha^g(\nu^g)}{d\nu^g} (\nu^g) \nu_{,k}^g \nu_{,k}^g - a_0^g \nu^g \quad (5.58)$$

In some particular conditions, the aggregate in concrete may be considered as incompressible. In this case, the conservation of mass equation reduces to:

$$\frac{\partial \nu^g}{\partial t} + \nabla \cdot (\nu^g \nu^g) = 0 \quad (5.59)$$

which gives:

$$\dot{\nu}^g = -\nu \dot{C}_{kk}^m \quad (5.60)$$

Now, the thermodynamical parameters can be found using the traditional approach for incompressibility.

The next step would be to prove the existence and uniqueness of these equations. This topic will not be treated in the present work. It should be pointed out that Nunziato and Cowin (5.41) treated the boundedness of solutions and established both uniqueness and weak stability of solutions to the mixed boundary-value problem for a particular class of linear elastic materials with voids. This permitted to analyze many applications including response to homogeneous deformations, pure bending of a beam, pressure vessel problems and small-amplitude acoustic waves (5.53 - 5.55). In principle the same could be done with concrete, including the effect of damage in which ν can be considered an integrity parameter ($\nu = 0$ corresponds to a material with no strength in extension or shear) as suggested by Passman (5.43).

5.6 References

- 5.1 Ortiz M. and Popov E.P., 'Plain Concrete as a Composite Material'. *Mechanics of Materials*, 1, no. 2, 1982.
- 5.2 Goodman M.A. and Cowin S.C., 'A Continuum Theory for Granular Materials'. *Arch. Ration. Mech. Analysis* 44, 249, 1972.
- 5.3 Deresiewicz H., 'Mechanics of Granular Matter'. *Adv. Appl. Mech.*, 5, 233, 1958.
- 5.4 Gjorv O.E., Sorensen S.I., Arnesen A. 'Notch Sensivity and Fracture Toughness of Concrete'. *Cement and Concrete Research* 17, 333, 1977.
- 5.5 Reiner M., 'A Mathematical Theory of Dilatancy'. *American Journal of Mathematics*. 67, 350, 1945.
- 5.6 Gassmann F., 'Elastic Waves Through a Packing of Spheres'. *Geophysics*, 16, 673, 1951.
- 5.7 Mindlin R.D., 'Compliance of Elastic Bodies in Contact'. *Journal of Applied Mechanics, Trans. ASME*, 71, 1949.

- 5.8 Mindlin R.D. and Deresiewicz, 'Elastic Spheres in Contact Under Varying Oblique Forces'. Journal of Applied Mechanics, Trans. ASME, 75, 327, 1953.
- 5.9 Duffy J. and Mindlin R.D., 'Stress-Strain Relations and Vibrations of a Granular Medium'. ASME, 57, 1956.
- 5.10 Muskhelishvili N.I., *Some Basic Problems of the Mathematical Theory of Elasticity*. P. Noordhoff, Groningen, 1963.
- 5.11 Goodier J.N., 'Concentration of Stress Around Spherical and Cylindrical Inclusions and Flaws'. J. Appl. Mech., ASME, 55, 7, 1933.
- 5.12 Edwards R.H., 'Stress Concentration Around Spherical Inclusions and Cavities'. Trans ASME, J. Appl. Mech, 18, 1, 1951.
- 5.13 Eshelby J.D. 'The Determination of the Elastic Field of an Ellipsoidal Inclusion and Related Problems'. Proc Royal Soc., 1957
- 5.14 Biot M. A., 'General Theory of Three-Dimensional Consolidation'. Journal of Applied Physics, 12, 155, 1941.
- 5.15 Biot M. A., 'Theory of Elasticity and Consolidation for Porous Anisotropic Solid'. Journal of Applied Physics, 26, 182, 1955.
- 5.16 Biot M. A., 'General Solutions of the Equations of Elasticity and Consolidation for a Porous Material'. Journal of Applied Mechanics, Trans ASME, 78, 91, 1956.
- 5.17 Biot M. A., 'The Elastic Coefficients of the Theory of Consolidation'. J. Appl. Mech. 24, 594, 1957.
- 5.18 MacKenzie J.K., 'The Elastic Constants of a Solid Containing Spherical Holes'. Proc. Phys. Soc., B63, 2, 1950.
- 5.19 Carroll M.M. and Holt, 'Static and Dynamic Pore-Collapse Relations for Ductile Materials'. J. Appl. Phys. 43, 1636, 1972.

- 5.20 Walsh J.B., 'The Effect of Cracks on the Compressibility of Rock'. J. Geophys. Res. 70, 381, 1965.
- 5.21 Walsh J.B., 'The Effect of Cracks on the Uniaxial Elastic Compression of Rocks'. J. Geophys. Res. 70, 399, 1965.
- 5.22 Walsh J.B., 'The Effect of Cracks in Rocks on Poisson's Ratio'. J. Geophys. Res., 70, 5249, 1965.
- 5.23 Jaeger J.C. and Cook N.G.W. *Fundamentals of Rock Mechanics*. Halsted Press, New York, 1979.
- 5.24 Green A.E. and Naghdi P.M., "A Dynamical Theory of Interacting Continua". Int. J. Engng. Sci, 3, 231, 1965.
- 5.25 Crochet M. J. and Naghdi P.M., "On Constitutive Equations for Flow of Fluid through an Elastic Solid". Int. J. Engng. Sci., 4, 383, 1966.
- 5.26 Marinis P.C. and Roberts B.W., "Compression of an Elastoporous Medium". Int. J. Non-Linear Mechanics, 13, 75, 1975.
- 5.27 Jenkins J.T., 'Static Equilibrium of Granular Materials'. J. Appl. Mech. 42, 603, 1975.
- 5.28 Passman S.L., 'Mixtures of Granular Materials'. Int. J. Engng Sci., 15, 117, 1977.
- 5.29 Ahmadi G. and Shahinpoor, "A Continuum Theory for Fully Saturated Porous Elastic Materials". Int. J. Non-Linear Mechanics, 18, 223, 1983.
- 5.30 Ahmadi G., "On Mechanics of Saturated Granular Materials". Int. J. Non-linear Mechanics, 15, 251, 1980.
- 5.31 Ahmadi G., "A Generalized Continuum Theory for Granular Materials". Int. J. Non-Linear Mechanics, 17, 21, 1982.
- 5.32 Ericksen J.L. and Truesdell C., "Exact Theory of Stress and Strain in Rods and Shells". Arch Rational Mech and Anal. 1, 295, 1958.

- 5.33 Toupin R.A., 'Theory of Elasticity with Couple-Stress'. Arch Rational Mech and Anal., 17, 1964.
- 5.34 Naghdi P., *Foundations of the Theory of Continuous Media*. Class Notes, University of California, Berkeley, 1985.
- 5.35 Lubliner J., *Thermomechanics of Deformable Bodies*. Class Notes, University of California, Berkeley, 1984.
- 5.36 Mindlin R.D., 'Microstructure in Linear Elasticity'. Arch Rational Mech and Anal., 16, 51, 1964.
- 5.37 Green A.E., Rivlin R.S., 'Multipolar Continuum Mechanics'. Arch Rational Mech and Anal., UL. 17, 1964.
- 5.38 Nunziato J.W. and Walsh E.K., 'Small-Amplitude Wave Behavior in One-Dimension Granular Solids. J. Appd. Mech. 44, 559, 1977.
- 5.39 Passman S.L., Nunziato J.W., Bailey P.B., Thomas J.P., 'Shearing flows of granular materials'. J. Engng. Mech. Div. ASCE 4, 773, 1980.
- 5.40 Nunziato J.W., Passman S.L., Thomas J.P. 'Gravitational flows of granular materials with incompressible grains'. J. Rheology 24, 395, 1980.
- 5.41 Nunziato J.W. and Cowin S.C., 'A Nonlinear Theory of Elastic Materials with Voids'. Arch. Rational Mech and Anal., 72, 175, 1979.
- 5.42 Cowin S.C. and Nunziato J.W., 'Linear Elastic Materials with Voids'. Journal of Elasticity 13, 125, 1983.
- 5.43 Passman S.L., 'Stress Relaxation, Creep, Failure and Hysteresis in a Linear Elastic Material with Voids'. Journal of Elasticity 14, 201, 1984.
- 5.44 Capriz and Cohen H., 'The Bubbly Fluid as a Continuum with Microstructure'. Mechanics Research Communications, 10, 359, 1983.
- 5.45 Bedford A. and Drumheller D.S. 'A Variational Theory of Immiscible Mixtures'. Arch. Rational Mech. Anal. 63, 37-51, 1978.

- 5.46 Bedford A. and Drumheller D.S., "A Variational Theory of Porous Media". *Int. J. Solids Structures* 15, 967, 1979.
- 5.47 Drumheller D.S. and Bedford A., "A Theory of Bubbly Liquids". *J. Acoust. Soc. Am.* 66, 197, 1979.
- 5.48 Drumheller D.S. and Bedford A., "A Thermomechanical Theory for Reacting Immiscible Mixtures". *Arch. Rational Mech. Anal.* 73, 257, 1980.
- 5.49 Bedford A. and Drumheller, "On Volume Fraction Theories for Discretized Materials". *Acta Mechanica* 48, 173, 1983.
- 5.50 Love, A.E. *A Treatise on the Mathematical Theory of Elasticity*, Cambridge, 1927.
- 5.51 Truesdell C. and Noll W., "The Non-Linear Field Theories of Mechanics". In *Handbuch der Physik* Edited by S. Flugge, Vol. III/3, Springer, Berlin, 1965.
- 5.52 Green A.E., Naghdi P.M. and Trapp, "Thermodynamics of Continuum with Internal Constraints". *Int. J. Eng. Sci.*, 8, 891, 1970.
- 5.53 Cowin S.C. and Puri P., "The Classical Pressure Vessel Problems for Linear Elastic Materials with Voids". *J. Elasticity*, 13, 157, 1983.
- 5.54 Cowin S.C., "The Stresses Around a Hole in a Linear Elastic Material with Voids". *Quart. J. Mech. Appl. Math.*, 36, 1983.
- 5.55 Nunziato J.W. and Walsh E.K., "On the Influence of Void Compaction and Material Non-Uniformity on the Propagation of One-Dimensional Acceleration Waves in Granular Materials". *Arch. Rational Mech. Anal.* 73, 285, 1980.

Chapter 6

Steel-Concrete Bond

6.1. Introduction

In the previous chapters the effect of the microstructure on the behavior of plain concrete has been discussed and analyzed. However most of the application of concrete in civil engineering practice is for reinforced or prestressed concrete structures, therefore this chapter will focus on the interaction between the concrete and the steel both on a microscopic and macroscopic levels.

From a mechanical point of view, bond can be considered as the shearing stress between the concrete and the reinforcing bar (6.1). It is the result of adhesion, friction, and support of the ribs. Plain bars rely mainly on adhesion and friction, while deformed bars depend mainly on the support of the ribs. Strands derive their bond resistance from adhesion, friction, and a mechanism called "lack of fit" which occurs if the wires of a strand will not fit into the mark of the new position, resulting in a wedge action and more friction (6.2).

The importance of the bond between the reinforcing bar and the concrete on the cracking behavior of reinforced concrete, on the deflection behavior and on the anchorage of reinforcing steel has been realized for a long time. In 1913, Abrams (6.3) performed pull-out tests using plain bars to determine the effect of settlement and shrinkage of concrete. His experiments showed that bars cast in a horizontal position exhibited lower bond resistance than vertical bars. Later on, Menzel (6.4) established the fundamental importance of the depth of concrete under a horizontal bar. He showed that as the depth of concrete under the bar increased, the bleeding water accumulated under the bar also increased, thereby weakening the bond resistance. Also his experimental results showed that the best performance was observed for vertical bars pulled against the direction of casting. This topic was further studied by Clark

(6.5,6.6), Collier (6.7), Jirsa et al. (6.8) among others, and the main conclusions were the following:

1. The bond of deformed bars is affected by the type of deformation, the position of anchorage, and the consistency of concrete. The bar size has little effect on the pattern of strength reduction with height.
2. The bond ratio between the top-cast reinforcing bar and the bottom-cast bar decreases as the casting height increases.
3. An increase in anchorage length does not produce a significance change in the bond efficiency of the top bar.
4. An increase in slump reduces the bond capacity as the depth of concrete is increased.

Initially research was concentrated on the global efficiency of the bond, and later it focused on the bond mechanisms, interface stresses, and relative displacements. The work of the following researchers should be mentioned: Mains (6.9), Bresler and Bertero (6.10), who measured the distribution of bond stress using electrical strain gages; Broms (6.11) who analyzed the relationship of bond slip and crack spacing; Lutz and Gergely (6.1) who studied the bond slip and bond splitting of deformed reinforced bars.

A great improvement in the modeling of the reinforcing concrete was achieved with the development of the finite element method, which permitted simulation of the effects of cracks in the reinforcing concrete by analyzing either sharp cracks or distributed cracks. The first condition of analysis, i.e., the sharp crack (6.12), can be implemented by doubling the nodes through which the crack propagates or by varying the stiffness of the linkage elements that connect the nodes of adjacent elements. One of the shortcomings of this approach is that the location and orientation of the cracks are not known in advance. As pointed out by Cedolin and Bazant (6.13), unless the nodes locations are considered as variables and unknown so that the nodes coordinates

are redefined, the crack propagation will necessarily coincide with the original element boundaries. The alternative to the discrete cracks is the continuous smeared-cracking model. In this approach, concrete becomes orthotropic after the first cracking has occurred. It should be noted that cracking is treated as a change in the material properties and that this formulation easily allows the account of aggregate interlocking by retaining a positive shear modulus, which means that secondary cracking does not necessarily appear perpendicular to the first direction of the cracks (6.14).

The main restriction to the use of the traditional finite element method is the lack of a precise criterion for crack propagation. The usual procedure of comparing the stress state resulting from the analysis with the tensile strength of concrete may be misleading: for example with a sharp crack, the stress concentration may be increasingly higher as the mesh in front of the crack is refined, and this causes a lack of objectivity since the concrete may or may not crack depending on the size of the element grid in front of the crack. Since this limitation is related to the lack of criterion for crack propagation, a natural source of inspiration is the fracture mechanics approach. However, for a number of reasons, concrete researchers were reluctant to use fracture mechanics principles. What they questioned was the simple use of the linear fracture mechanics for such a heterogeneous material. Recently, a series of developments were obtained by means of the non-linear fracture mechanics, namely the J-integral (6.15), COD (6.15, 6.16), R-curve analysis (6.15,6.17,6.18) and the "fictitious" crack model (6.19,6.20,6.21), the last two being the most promising for concrete. Returning to the crack propagation criteria, Bazant and Cedolin (6.22,6.23,6.24) proposed the use of an energy criterion based on fracture mechanics. They showed that using this criterion, the results became independent of both the element size and the type of element used.

The characterization of the bond morphology attracted less attention, and little effort was spent in trying to correlate the microstructure and the mechanical properties

of the bond. One of the few exceptions is the work of Al Khalaf (6.25) and Page (6.26) who studied the interface between mild steel and cement paste or mortar. Also the comprehensive work of Sakamoto and Iwasaki (6.27) in describing the influence of sodium chloride on the concrete-steel bond should be mentioned.

The study of reinforcing concrete is often done by considering it as a composite material formed by the reinforcing bars and the surrounding concrete. In this Chapter, reinforcing concrete will be considered as a multiphase material, in which the microstructures of each phase and also their interfaces (steel-concrete, aggregate-matrix) play an important role; therefore in this sense this study may be considered as a corollary of several previous chapters in which each characteristic was studied separately. While unnecessary duplication of material was avoided, some results that may help to put the steel-concrete bond in perspective were emphasized. The analysis of the morphology of the steel-cement paste as affected by age and by the amount of silica fume is described in Section 6.2. Corrosion of the reinforcing steel in concrete is a major problem in engineering practice; and in Section 6.3, the effect of chlorides with and without silica fume on the corrosion of the steel-cement paste is described. The mechanical properties of the steel-concrete bond as influenced by position of the bar, the type of bar (plain and deformed), concrete strength (4 levels), and amount of silica fume (3 levels) are described in Section 6.4.

6.2 Microstructure Characterization of the Interface

The steel-cement paste interface was studied with the same techniques described in Section 3.2, Fig 6.1 summarizes the experimental procedure for casting the cement paste on top of the steel surface and the subsequent breakage of the composite material to analyze the interface either by SEM or by XRD using the method of successive abrasion. One hundred cylindrical specimens of rebar steel (19mm) were polished down to 1 micron for this study.

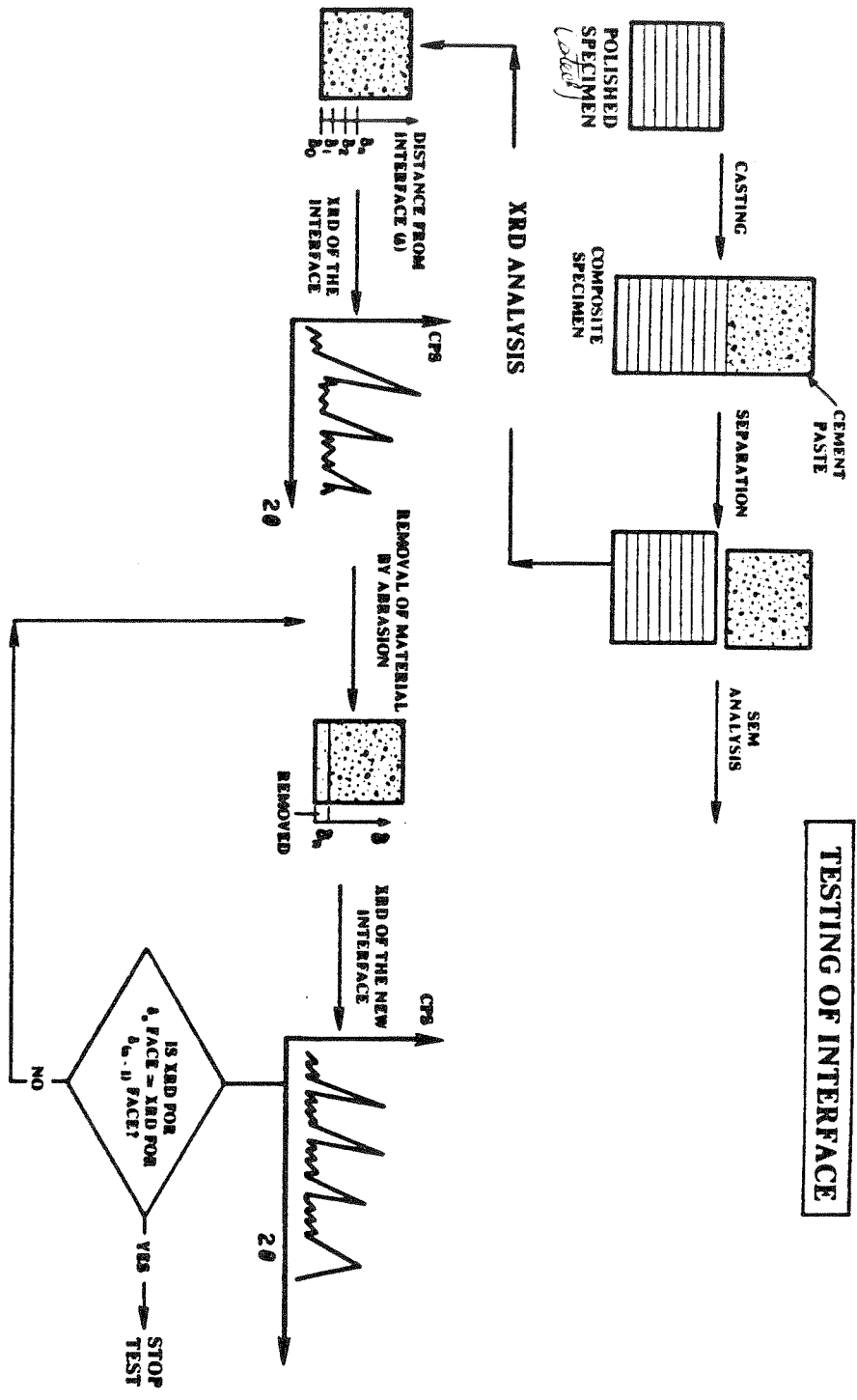
The composition of the portland cement used in this research is presented in Table 2.1. The water-cement ratio of the cement paste was kept constant at 0.35. Three levels of silica fume replacement were used (0, 5, and 16 percent) with the objective of giving qualitative correlation with the performance of concrete using approximately the same levels. In order to produce a workable mix when using 16-percent silica fume replacement, one percent of a water reducer agent was used.

6.2.1 Morphology of the Interface

During the testing time (up to one year) and the temperature (70° F) used in the present investigation, steel may be considered as an inert material. Therefore, the morphology of the transition zone is similar to the one described for quartz. Section 6.3 will analyze the case where steel cannot be regarded as an inert material due to the presence of chloride ions that promote steel corrosion.

The surface effect produced by the steel surface, against which the cement paste was cast, originates zones of matrix with high water-cement ratio near the interface. The influence of this surface effect will extend from the interface and will have a great influence on the steel-cement paste bonding mechanism. As mentioned in different parts of this thesis, Sections 3.3, 3.4, and 3.5, one of the main characteristics of the interface between cement paste and all the materials studied in this thesis is the precipitation of calcium hydroxide crystals with the c-axis perpendicular to the interface. As before, we will refer to these crystals in direct contact with the steel surface as the CH or interfacial film and to the region affected by the surface effect as the transition zone. Fig. 6.2 shows the calcium hydroxide film (cement paste side), and it is interesting to note that the specimen contained 16-percent of silica fume replacement which did not alter the global formation of the CH film. Fig. 6.3 shows the calcium hydroxide film in a 30-days old specimen without silica fume. The CH film is smooth and even though the crystal structure behind it is dense, there is not a perfect union

TESTING OF INTERFACE



6.1
~~Fig. 6.1~~
 Test Procedure

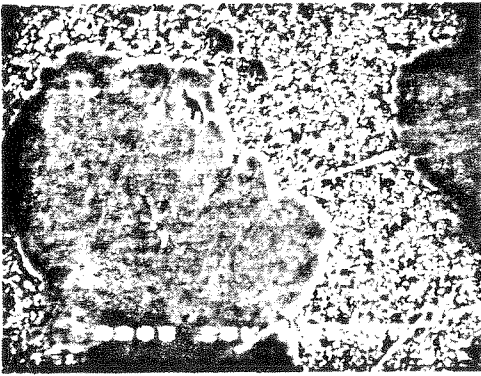


Fig 6.2
 Calcium Hydroxide Film on the
 Cement Paste Side
 (30 days old, 16% silica fume)



Fig 6.3
 Calcium Hydroxide Film on the
 Cement Paste Side
 (30 days old, No silica fume)

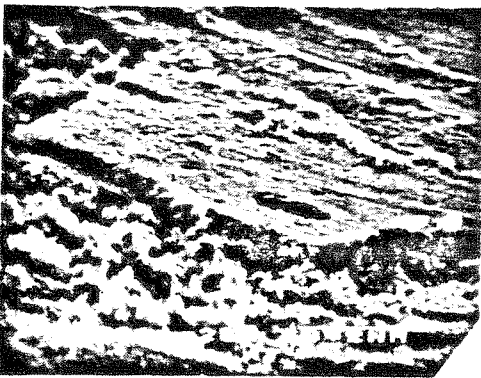


Fig 6.4
 Pozzolanic Reaction on the Top of
 Calcium Hydroxide Film
 (30 days old, 16% silica fume)

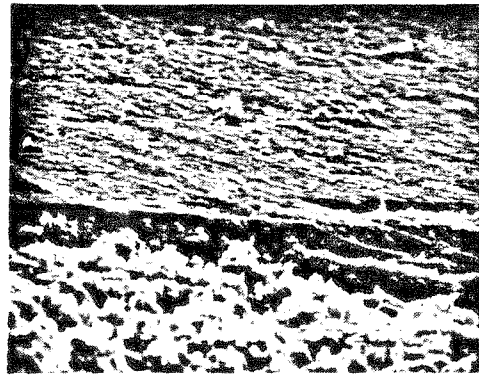


Fig 6.5
 Depopulation of the Structure
 Behind the Calcium Hydroxide
 Film (30 days old, 16% silica fume)



Fig 6.6
 Another view of the Bond Board
 Between the Calcium Hydroxide
 Film and the matrix when
 Silica Fume is Used.

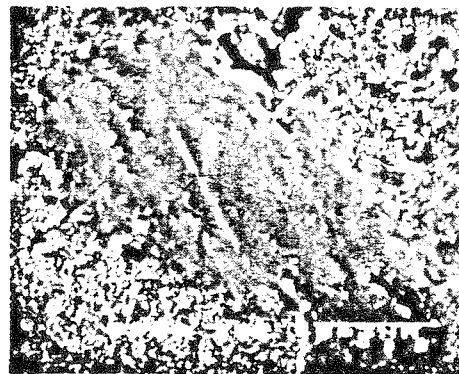


Fig 6.7
 Calcium Hydroxide Film Surrounded
 by a Dense Matrix (16% silica fume)

between the interfacial film and the interfacial zone. Compare now the features shown in Figs. 6.4 and 6.5 for a specimen that contained 16 percent of silica fume replacement at the same age (30 days). The CH film is partially covered with CSH due to the pozzolanic reaction between the calcium hydroxide and the silica fume; also the CH film is united to the matrix by a dense interlocking. The pozzolanic reaction happens in localized zones and seems to introduce "welding points" on the steel-paste interface, however the dominant effect that happens throughout the specimen is the densification of the structure behind the film (Figs 6.6 and 6.7). This causes a reduction in porosity that existed in the interfacial zone which explains the strengthening effect when silica fume is used.

Figs. 6.8 and 6.9 show the distribution of silica fume particles on the steel surface. It can be seen that they are partially dissolved. Some silica fume particles dissolve quickly during the early stages of hydration while others are only partially dissolved when equilibrium is reached. Some of them may take part later in the pozzolanic reaction with the CH film, forming CSH on top of the film (Fig. 6.10 and 6.11). However, some silica fume particles, or their pseudomorphs, get engulfed in the CH film. The effect of these particles on the mechanical behavior of the film is not known, nevertheless we may expect these particles to reinforce the film. Figs. 6.12 and 6.13 show these particles around a crack in the film (probably due to shrinkage). It can be seen that the particles are fairly well distributed in the film and that they bridge the crack in various points. This process consumes energy, therefore these particles toughen the film. However, it should be clear that we are referring to a local toughening effect; the global toughness of the specimen will depend on a variety of other factors such as the size of the flaws, the microstructure of the crystals, etc. Figs. 6.14 and 6.15 show other cracks in the interfacial film with low and high magnifications. Note the "kink" of the crack path due to the presence of one of these inclusions.

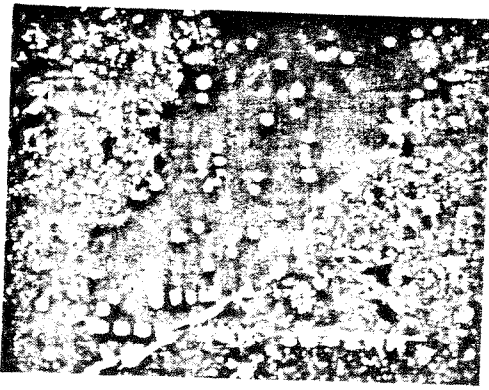


Fig 6.8
Distribution of Silica Fume Particles
on the Steel Surface

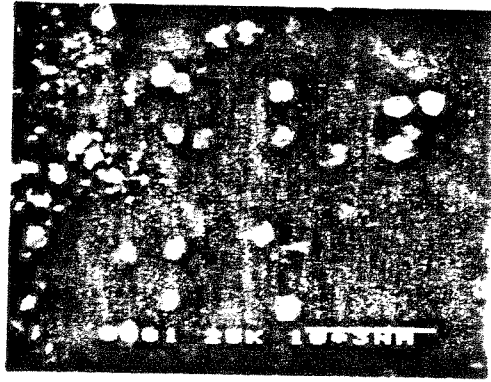


Fig 6.9
Detail of the Partially Dissolved
Particles of Silica Fume on the Interface



Fig 6.10
Pozzolanic Reaction on the Calcium
Hydroxide Film

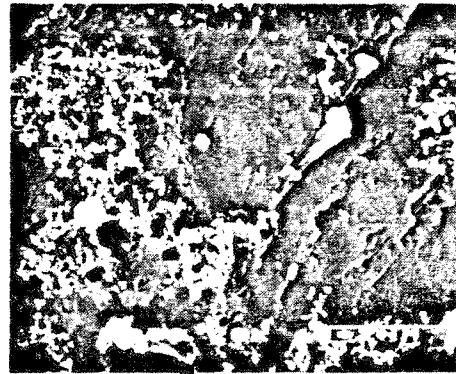


Fig 6.11
Detail of the Pozzolanic Reaction

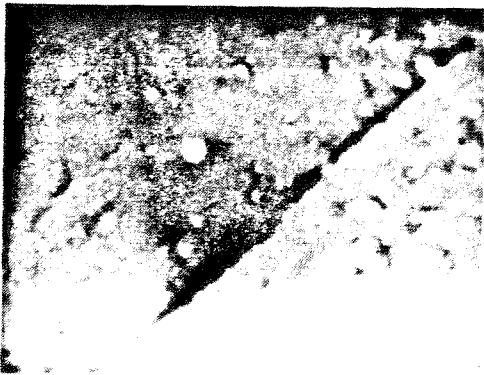


Fig 6.12
Silica Fume Particles Embedded in the
Calcium Hydroxide Film



Fig 6.13
Silica Fume Bridging a Crack in the
Calcium Hydroxide Film

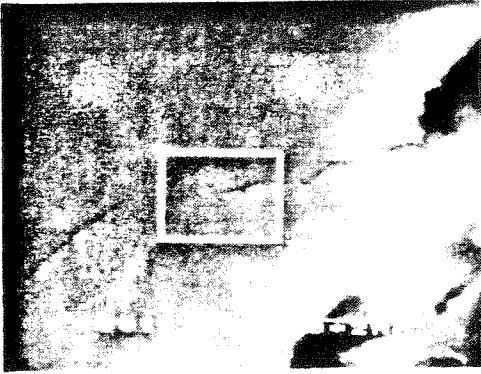


Fig 6.14
General Aspect of the Submicron
Particle Dispersed in the
Calcium Hydroxide Film

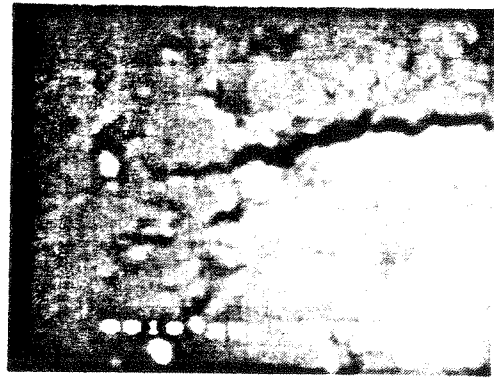


Fig 6.14a
Detail of the zone delimited
by the white Rectangle in
Fig 6.14

6.2.2 XRD Analysis of the Interfacial Zone

The method of successive abrasion of the interface and its analysis by XRD permits the characterization of the hydration products over the interfacial zone. Once the calcium hydroxide crystals are precipitated in a preferential orientation, it is not possible to perform a quantitative analysis of them with this method. The index of preferential orientation, as defined in Sections 3.2 and 3.3, will be used. The ettringite is not subjected to preferential orientation, and its peak at $9.1^\circ 2\theta$ ($Cu-K\alpha$) was selected because it is not interfered with by other peaks, therefore it is possible to estimate the ettringite concentration over the interfacial zone.

The XRD method permits the analysis of the interfacial zone in a global way, as compared to the localized analysis performed by SEM. However, as described in Section 3.2, this method uses the value of the interfacial zone density which is not known but which is assumed to be equal to the bulk density of the paste (which is probably higher). Also when fracturing the composite specimen, some of the interfacial film (and some hydration products bonded to it) may adhere to the steel side, so that the thickness of this attached film is difficult to access, creating problems in defining the reference plane of the original interface. These uncertainties are particularly important for analysis closer to the interface since as already shown, the surface effect decays exponentially with distance from the interface. Therefore in fitting the data, in addition to the traditional method of the least squares, two other linear models, one minimizing the sum of the absolute residuals and the other using a robust criterion, were used in a system for interactive data analysis. It should be mentioned that the term "robustness" means relative insensitivity to moderate departures from assumptions.

The method of robust regression is used to analyze the behavior of least squares estimation when the disturbances are not well behaved. Coleman et al. (6.28) developed the computational procedures for iteratively reweighted least squares.

Consider the vector of observations b ($m \times 1$), the data matrix A ($m \times n$), the vector of parameters x ($n \times 1$) and a vector r ($m \times 1$) to model the equation $b = Ax + r$. The least square solution consists in obtaining the minimum of $\sum_{i=1}^m ((r_i(x))/s)^2$, where r is the residual vector of $b - Ax$ and s is a constant.

The weighted least square approach consists in finding the minimum of $\sum_{i=1}^m W_i ((r_i(x))/s)^2$, where W is a diagonal matrix of weights that are functions of scaled residuals. In the case of iteratively reweighted least squares, we have an optimization in the sense that a function of scaled residuals is minimized. This function determines the formula for the weight function used. The other method consists in solving the linear l_1 data fitting problem. The motivation for using the l_1 approximation rather than the l_2 (least squares) approximation or an l_∞ approximation is that the first one is recommended for data that may contain inaccurate points compared to the overall accuracy of the data. The solution proposed by Barrodate and Roberts (6.29) was used for this method.

Tables 6.1 and 6.2 show the thickness and the orientation of the interfacial zone as affected by age and amount of silica fume.

The analysis of the results should be made with special care. First one should realize that the results reflect a partial description of the morphology of the interfacial zone, and any hasty generalization of the microstructure description in the interfacial phase and even worse direct correlation of it to the mechanical properties will be bound to result in failure or incorrect predictions. One example would be the variation of the interfacial phase thickness with time. For a pure portland cement paste the thickness of the interface increases with time while the strength also increases with time, which may be a paradox. However, this paradox is eliminated when we understand that the physical meaning of the interfacial phase thickness is the measure of how far the surface effect of the steel will influence the bulk matrix. The mechanical

TABLE 6.1
Thickness of the Transition Phase (Microns)

AMOUNT OF SILICA FUME	AGE, days				
	1	7	30	90	420
0%	20.*	31.53	32.58	36.00*	43.11
5%	19.71	30.00*	14.09	19.44	8.71
16%	19.61	17.36	8.58	18.59*	N.A

TABLE 6.2
Orientation of the CH Film

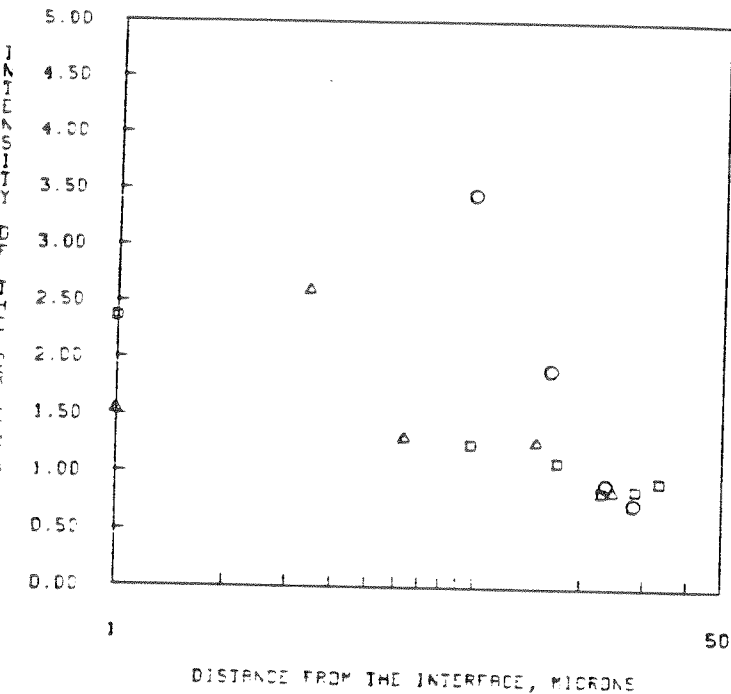
AMOUNT OF SILICA FUME	AGE, days				
	1	7	30	90	420
0%	1.54	4.02	3.10	2.66*	4.55
5%	2.35	2.16	1.77	2.90	1.64*
16%	12.67	7.22	5.85	2.31*	N.A

*Actual experimental points (not obtained from curve fitting).

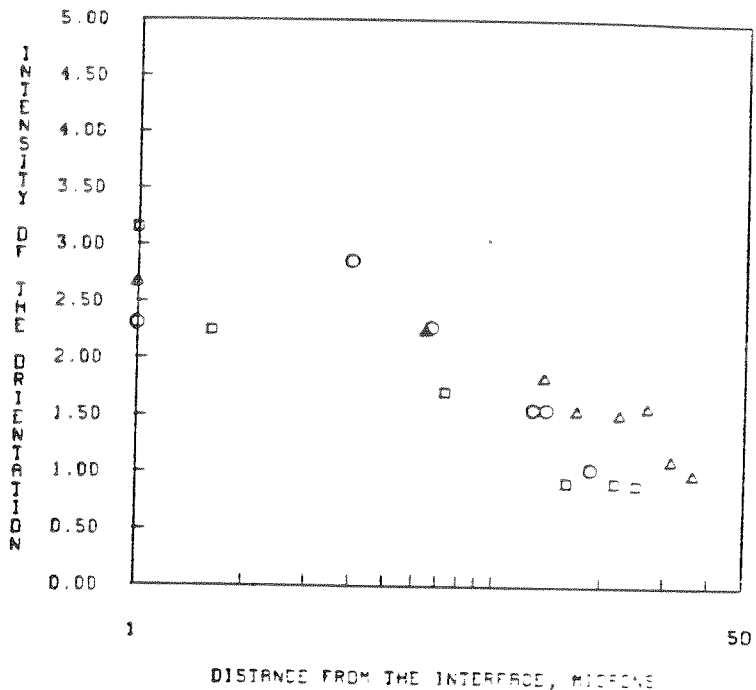
behavior of the interface will be determined by the parameters discussed in Chapter 4.

The use of silica fume produces a remarkable decrease of the interfacial zone thickness as shown in Table 6.1 and Figs. 15A and B. The studies of Kurdowski and Nocun-Wczelik (6.30) showed that active silica powder accelerated the reaction of

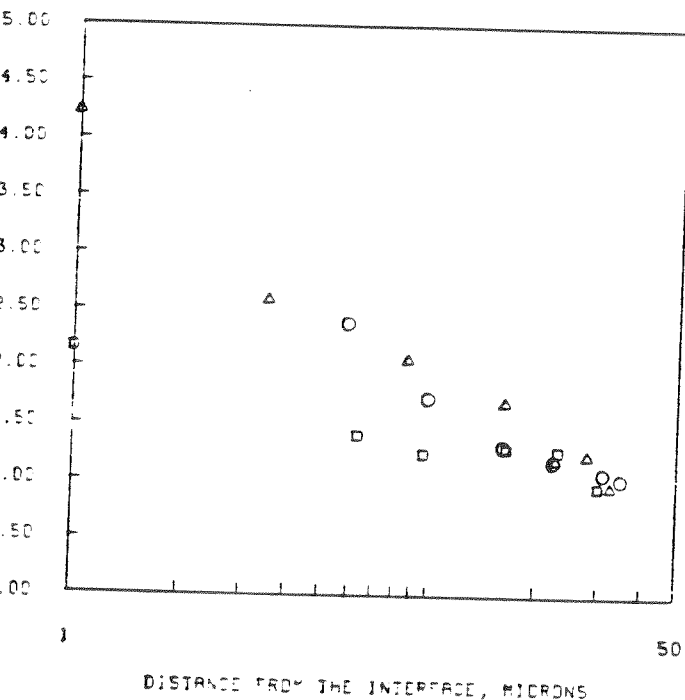
CH PREFERENTIAL ORIENTATION 1 DAY



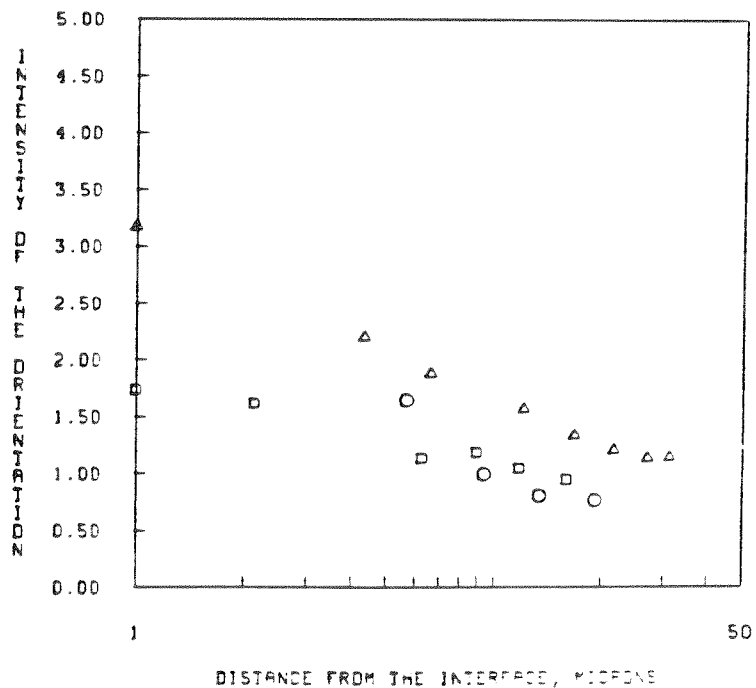
CH PREFERENTIAL ORIENTATION 90 DAYS



CH PREFERENTIAL ORIENTATION 7 DAYS



CH PREFERENTIAL ORIENTATION 30 DAYS



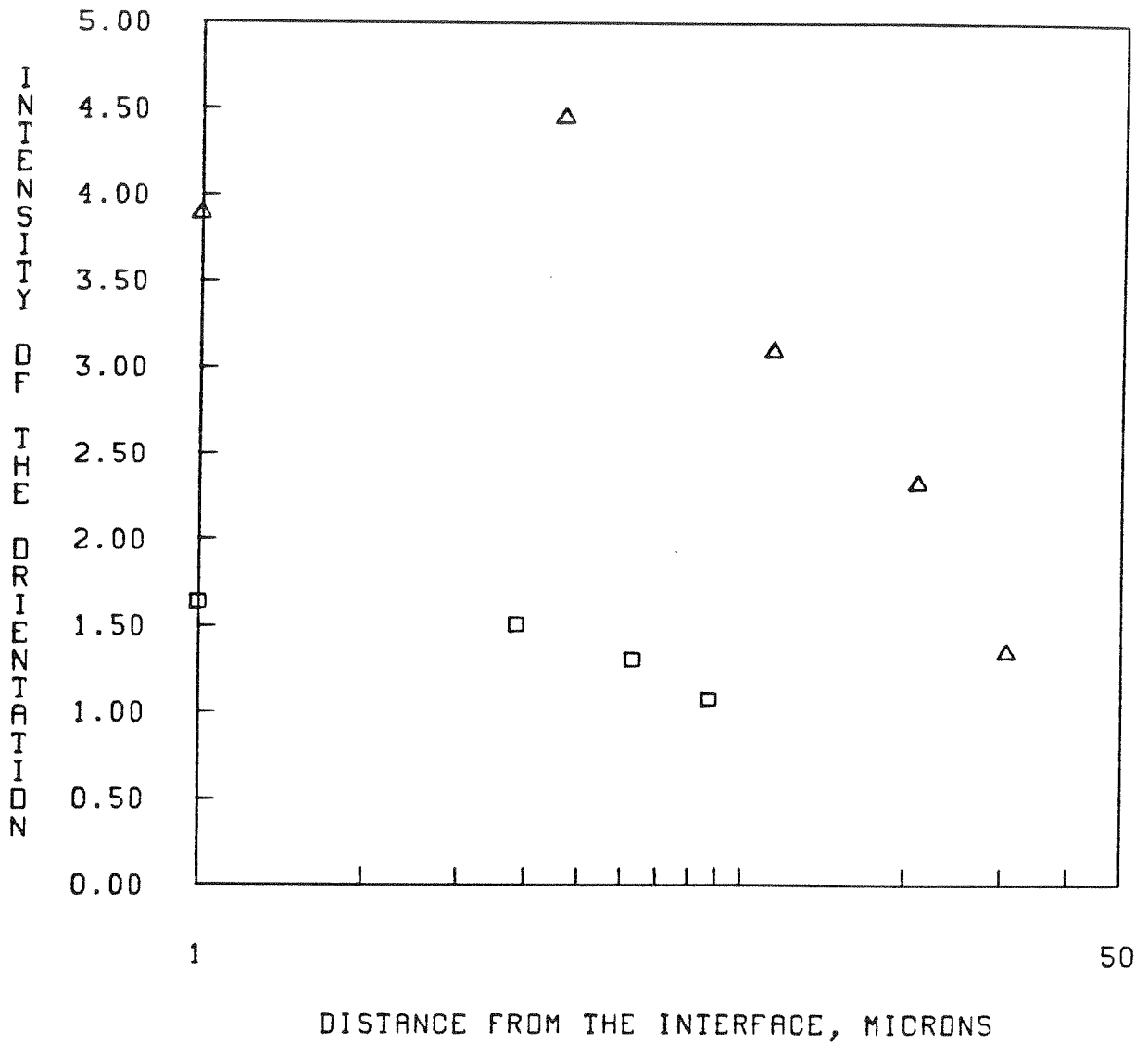
△ 40% silica fume
 □ 50% silica fume
 ○ 10% silica fume

△ 40% silica fume
 □ 50% silica fume
 ○ 10% silica fume

X

Fig 15A
 Calcium Hydroxide Preferential Orientation
 in the Transition Zone

CH PREFERENTIAL ORIENTATION 420 DAYS



△ 0% silica fume
□ 5% silica fume

*Fig. 6.15 B
Calcium Hydroxide Preferential Orientation
in the Transition Zone*

tricalcium silicate with water. Increasing additions of silica cause the development of greater heat and a shorter dormant period. It was concluded that the C_3S hydration is controlled by the conditions governing the liquid phase and that the reaction rate is controlled by the transportation process of calcium ions from the grains surface to the solution. In this case, C_3S hydration will be controlled by the consumption of Ca^{2+} ions from the solution as a result of the CH and CSH precipitation. Therefore the presence of a highly reactive silica lowers the calcium ions concentration in the solution forming CSH with low C/S ratio and increases the rate of C_3S hydration. Since the Ca^{2+} ions cannot easily diffuse in great quantity towards the aggregate face, the preferential orientation of the CH crystals is decreased, and due to the pozzolanic reaction the porosity in the interfacial zone is remarkably decreased.

The observed effect of silica on the preferential orientation of CH may be explained by the following mechanisms:

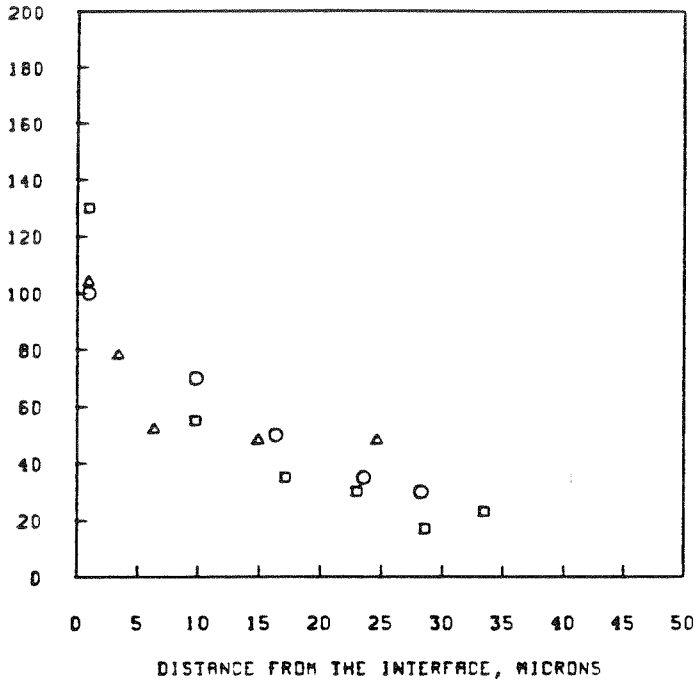
1. Less accumulation of free water at the interface;
2. Nucleation sites preventing a preferential orientation;
3. Pozzolanic reaction reducing the CH on the interface.

Figs. 16A and B show that there is a great concentration of ettringite near the aggregate surface for all ages and all levels of silica fume. This observation supports the through-solution mechanism of cement hydration as the cement particles must dissolve to provide the calcium, sulfate, and aluminate ions which then diffuse towards the aggregate surface where more ettringite get precipitated.

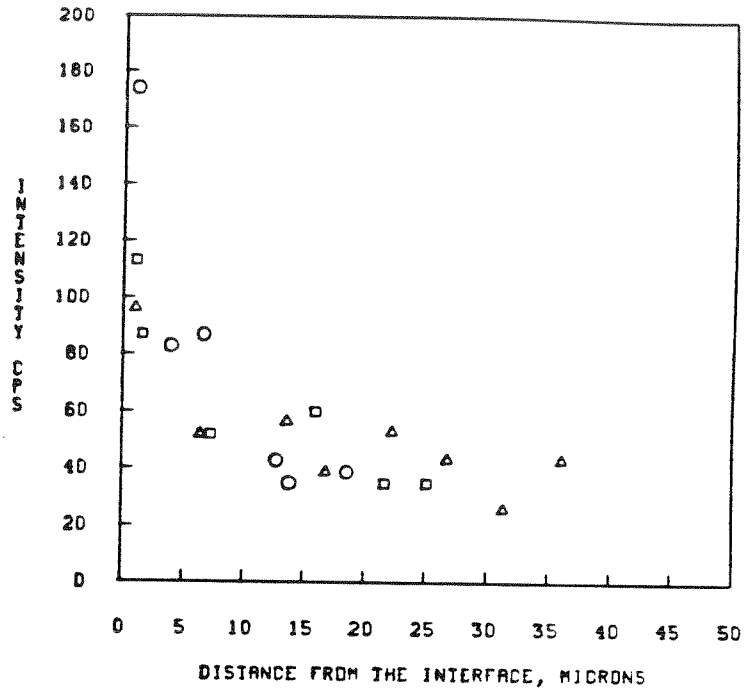
6.3 Effect of Chloride on the Interface

Until quite recently most studies on steel corrosion in reinforced and prestressed concrete structures were quite empiric. The quality of concrete was typically described by compressive strength, w/c ratio, and cement content; and the results were mostly

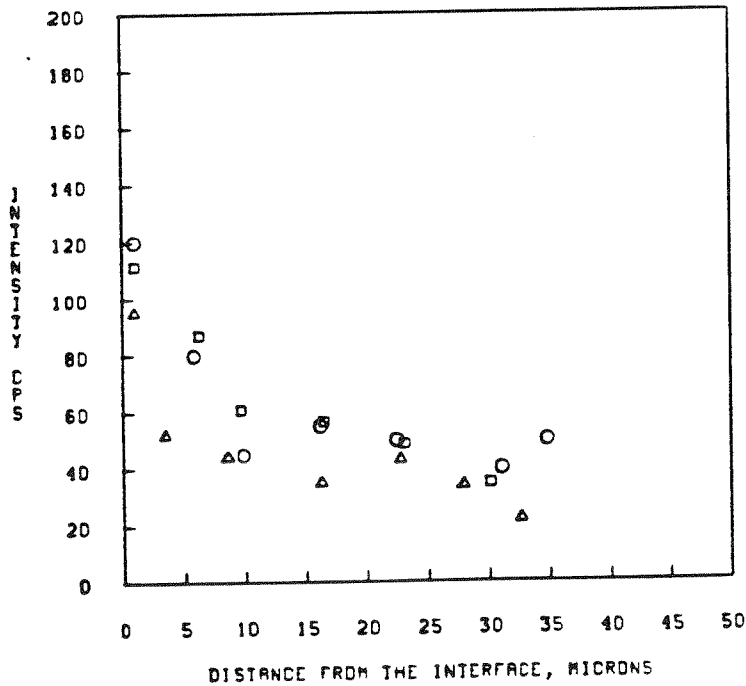
ETTRINGITE DISTRIBUTION 1 DAY



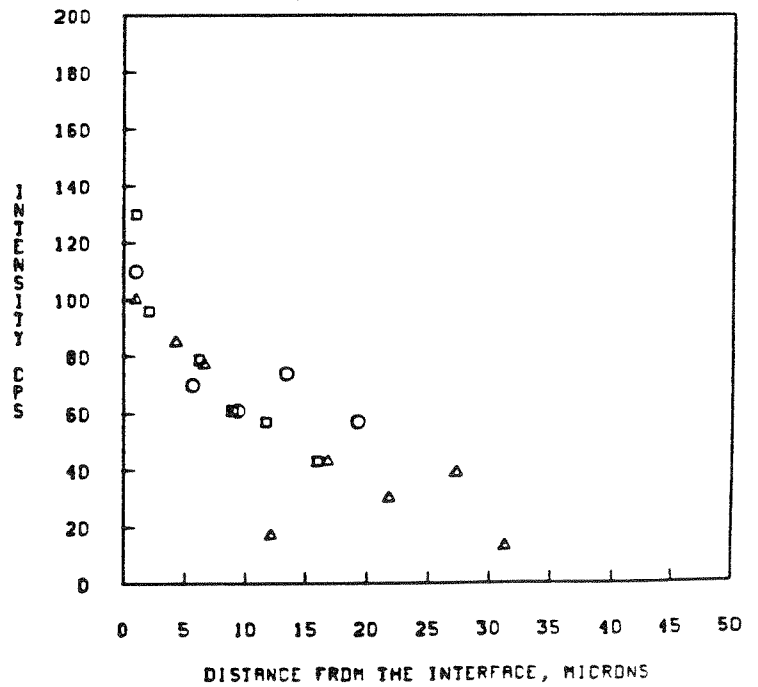
ETTRINGITE DISTRIBUTION 90 DAYS



ETTRINGITE DISTRIBUTION 7 DAYS



ETTRINGITE DISTRIBUTION 30 DAYS

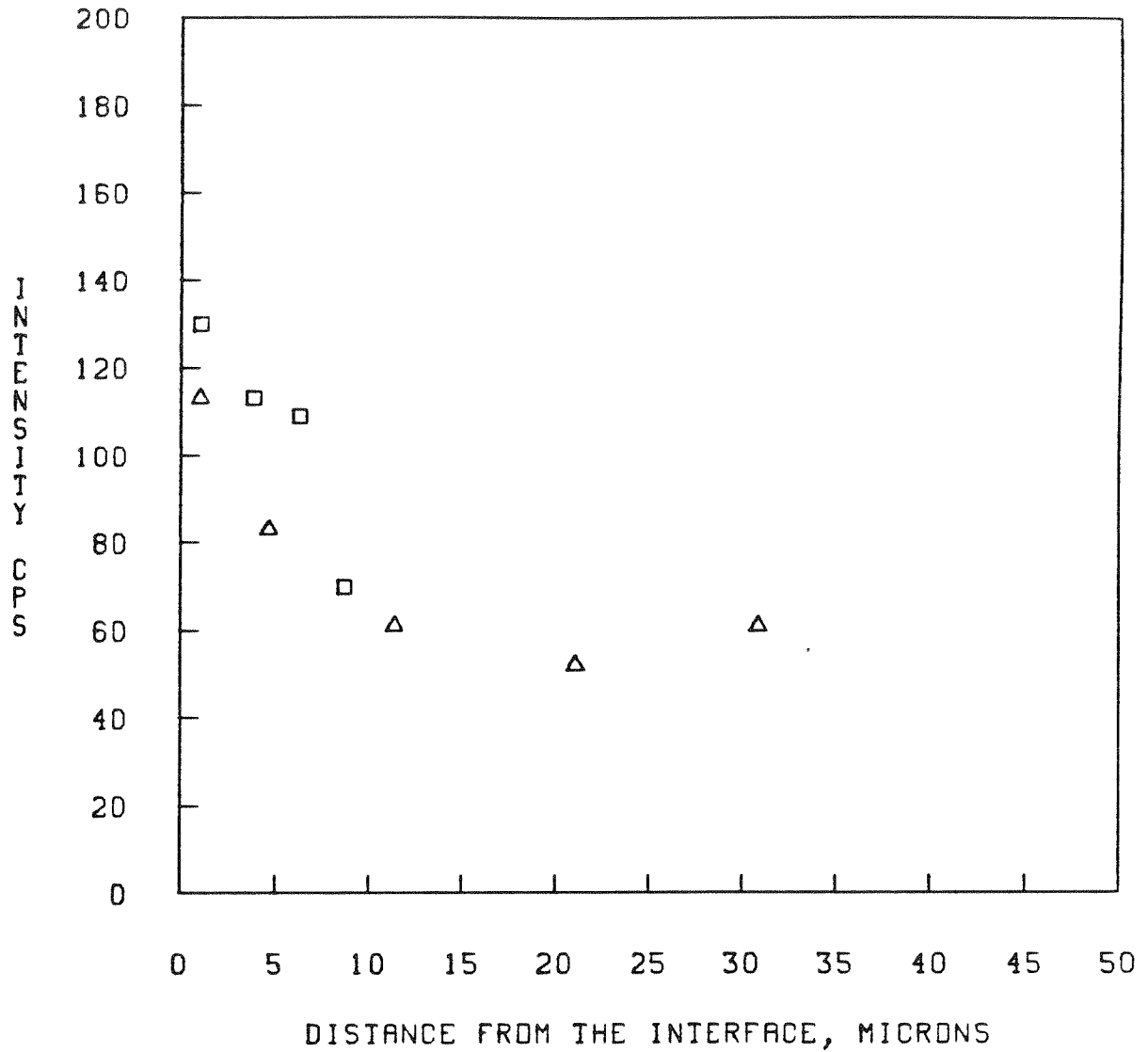


Δ 0% silico fume
 □ 5% silico fume
 ○ 16% silico fume

Δ 0% silico fume
 □ 5% silico fume
 ○ 16% silico fume

Fig. 16A
 Ettringite Distribution in the Transition Zone

ETTRINGITE DISTRIBUTION 420 DAYS



△ 40% silica fume
□ 5% silica fume

*Fig. 16B
Ettringite Concentration in the Transition Zone*

based on thickness of concrete cover and amount of chlorides in the environment. Basic information about the mechanisms of rebar corrosion was scarce, and experience related to basic factors controlling corrosion hardly existed.

During recent years considerable basic research on steel corrosion in concrete has been carried out, and information on concrete as an electrolytic system is now available. Many reports and papers have been published, a recent review of which is given by Slater (6.31).

However, it is interesting to note that comparatively little attention has been given to the microstructure characterization of the steel-cement paste interface during corrosion. It is well known that the interfacial zone between steel and cement paste has quite unique characteristics in the form of higher porosity and larger crystals than the bulk of the cement paste. Information about the microstructure of the interfacial region must therefore be of importance to the corrosion of embedded steel.

Nicol (6.32) and Morea (6.33) provided the first evidence that the interfacial zone separating concrete and embedded steel was composed largely of segregated lime crystals. These observations were later on confirmed by Page (6.34) who used a scanning electron microscope to show that the steel was in intimate contact with a lime-rich layer over most of its surface. He proposed that the massive deposition of $Ca(OH)_2$ crystals over the steel surface during the cement hydration modifies the electrode characteristics of the steel. This lime will provide a continuous source of OH^- which will affect the steel anodic behavior and will also reduce the diffusion of oxygen towards the steel surface.

In the following paragraphs some typical features of the interface between corroding steel and chloride-containing cement paste, with and without condensed silica fume, are presented.

6.3.1 Experimental

In order to study the interface between steel and cement paste, composite specimens consisting of cement paste cast against a polished surface of rebar steel (19 mm) were used. A STM Type II portland cement was employed, and the cement paste had a w/c ratio of 0.35. In order to introduce corrosion, addition of 2-percent calcium chloride (analytical reagent) by weight of cement was used. For half of the specimens, condensed silica fume in the form of 16-percent replacement by weight of the portland cement paste plus a lignosulfonate type of plasticizer were employed. The steel surface which was not in contact with the cement paste was protected against corrosion by coating it with paraffin wax.

The composite specimens were covered with a plastic wrap and stored in a fog room at 20° C. At specified ages up to 180 days, the specimens were removed from the fog room and placed in a dessicator for drying. Due to differential drying shrinkage the cement paste and steel became separated at the steel surface. The specimens were stored in a CO₂ free environment until examination. The interfacial zone was examined by scanning electron microscopy.

6.3.2 Results and Discussion

It has been shown that addition of silica fume reduced the degree of orientation of large CH crystals forming in the transition phase near the aggregate surface. Although the addition of silica fume produced more CSH gel in the cement paste, a solid film of large CH crystals still formed over most of the steel surface in spite of as much as 16-percent portland cement replacement with silica fume.

A typical feature of the lime film formed over the interface can be seen on the left-hand side of Fig. 17, which shows a scanning electron micrograph of the 180-days old specimen with 16-percent silica fume replacement. Just below the interfacial film the area covered by the rectangular mark in Fig. 17 was magnified for further

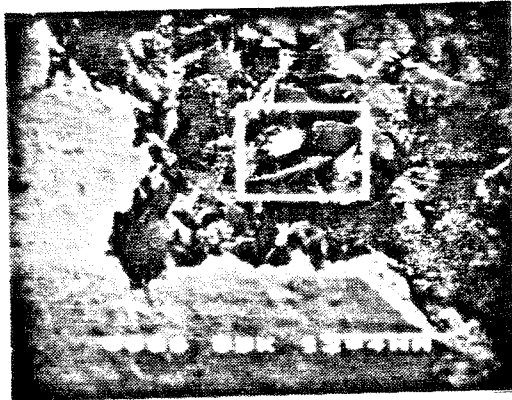


FIG. 8.17
SCANNING ELECTRON MICRO-
GRAPH OF THE STEEL-CEMENT
PASTE INTERFACE IN THE PRES-
ENCE OF CONDENSED SILICA FUME.



FIG. 8.18
A - POZZOLANIC REACTIONS PRO-
DUCT CONDENSED SILICA FUME
AND CH.
B - PLATE-LIKE CRYSTALS OF
MONOSULFATE HYDRATE OR CH.

examination. The result is shown in Fig. 16. Two features which are noteworthy are marked A and B. It is believed that the reticular small crystals on a large CH plate (A) represent the evidence of the pozzolanic reaction between the condensed silica fume and calcium hydroxide. The thin plate-like crystals (B) are probably of monosulfate hydrate. The possibility that large CH crystals are precipitated as small plate-like crystals in the presence of chloride cannot be ruled out. For a definite identification of the reaction products, X-ray energy dispersive analysis is required. Unfortunately, the scanning electron microscope facility used by the authors did not have this equipment. It is interesting to point out that of all specimens only those containing the silica fume showed visual evidence of corrosion. It has been previously been observed that increasing additions of silica fume both reduced the alkalinity and the ability of the cement paste to bind the chloride (6.36). A higher Cl^-/OH^- ratio in the pore solution of the cement paste is probably the reason for the observed corrosion phenomenon. For the specimens which showed corrosion, the phenomenon was typically observed after 3 months in the fog room. Fig. 19 shows bulk corrosion products formed on the interfacial film.

The growth of corrosion products was typically dendritic as demonstrated in Fig. 20, while a general feature of the interfacial film with corrosion products is shown in Fig. 21. At a more advanced stage of corrosion, large deposits of corrosion products showed evidence of spalling of the interfacial film, as demonstrated in Fig. 22.

6.3.3 Conclusions

A study of the interfacial zone between steel and portland cement paste containing calcium chloride showed that for specimens with portland cement alone, the interfacial film consisted of large CH crystals. For specimens in which a 16-percent replacement of the portland cement was done with condensed silica fume, this feature of the interfacial zone did not change too much. However, the specimens with silica fume

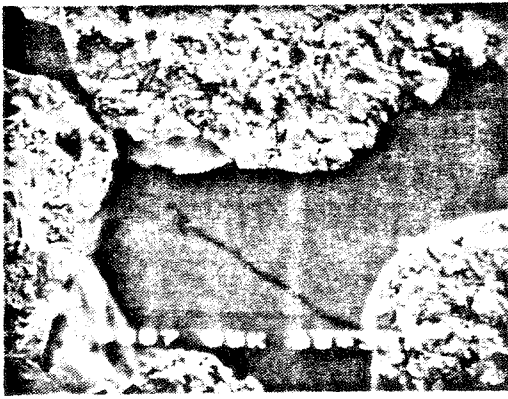


FIG. 19
SCANNING ELECTRON MICRO-
GRAPH OF THE BULK CORROSION
PRODUCTS ON THE INTERFACIAL
FILM.

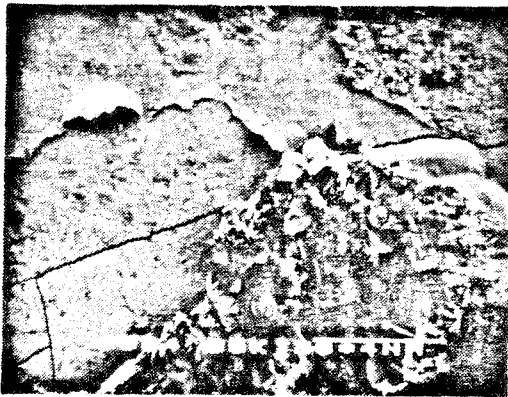


FIG. 22
SCANNING ELECTRON MICRO-
GRAPH OF CORROSION PRODUCTS
AT ADVANCED AGE SHOWING SPAL-
LING OF THE INTERFACIAL FILM.



FIG. 21
SCANNING ELECTRON MICRO-
GRAPH SHOWING THE GENERAL
FEATURES OF CORROSION PRO-
DUCTS ON THE INTERFACIAL FILM.

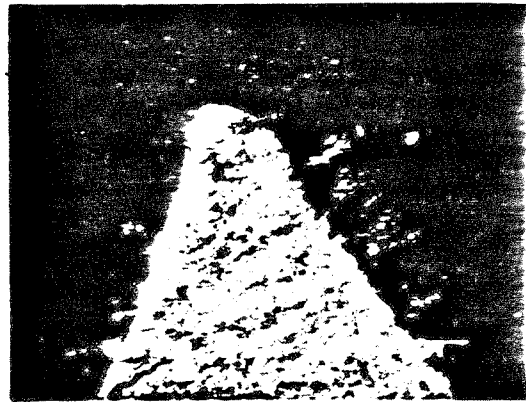


FIG. 20
DENDRITIC GROWTH OF CORRO-
SION PRODUCTS ON THE INTERFA-
CIAL FILM.

were found to be more sensitive to the chloride-induced corrosion. This observation supports the findings of a previous investigation that higher concentrations of chloride ions are present in the pore solution when silica fume is used.

6.4 The Mechanical Behavior of the Concrete-Steel Bond

As described in Section 6.1, the pull-out test has been used for a long time to estimate the concrete-reinforcing steel bond, and much information was gathered. However most of the tests were performed for normal strength concrete made with pure portland cement (or sometimes in combination with a pozzolan as an admixture). Presently the use of high-strength concrete has been increased intensively, and there is no systematic information on the bond strength for this type of concrete, especially when the levels of silica fume and water-reducing agents vary.

After the morphology of the steel-cement paste was analyzed in some detail in Section 6.3, it is tempting to correlate or at least to establish some trends with the macrostructure performance of the interface. Indeed, having this goal in mind, the concrete mix will have three levels of silica fume as used in Section 6.3. In order to understand the combined effect of compressive strength level and the amount of silica fume used, a comprehensive program using 16 different concrete mix designs was studied.

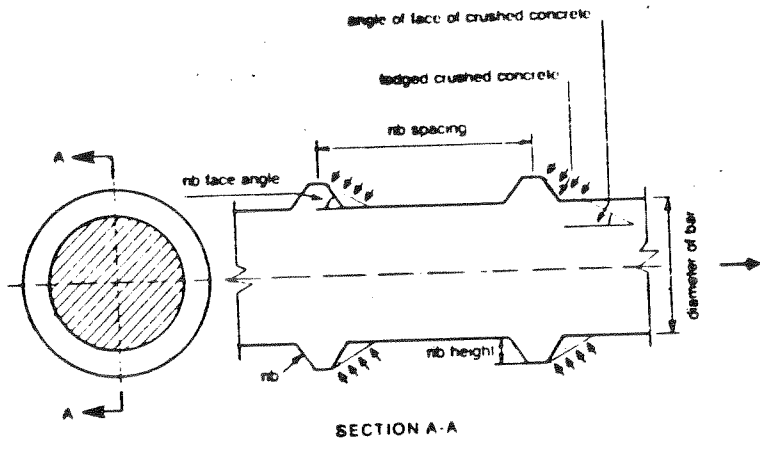
6.4.1 Reinforcing Steel-Concrete Bond Mechanism

The experimental program will use plain and deformed bars in the pull-out tests. Since these bars have a major difference in the cracking formation in the concrete and on the failure mode of the specimen, some basic principles on how these bars perform should be reviewed.

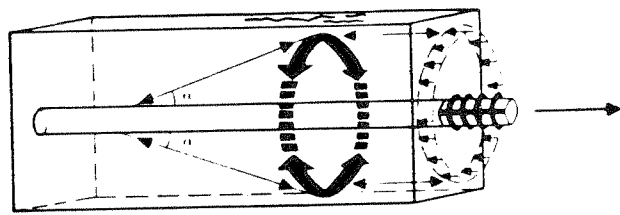
As stated in Section 6.1, the bond for deformed bars depends on the mechanical action. For lower loads, chemical adhesion associated with mechanical interaction

prevents slip. When adhesion is lost and consequently slip occurs, the ribs of a deformed bar will restrain this movement. This mechanism is different for a plain bar, where friction occurs when there is slip between bar and concrete. Lutz and Gergely (6.1) proposed that slip of a deformed bar can occur in two ways: (a) the ribs can push the concrete away from the bar by a wedging action, and (b) the ribs can crush the concrete. They showed also that ribs with a face angle between 40° and 105° produce approximately the same movement. For these ribs, slip is produced mainly due to the crushing of the concrete in front of the rib, once the existing friction between the face of the rib and the concrete is enough to avoid relative movement at the interface. As concrete is being crushed, it is lodged in front of the rib in such a way as to produce an effective face of the rib with angles of 30° and 40° (Fig. 6.23 from Tepfers).

Goto (6.37,6.38) developed a clever scheme to experimentally investigate the bond mechanism by injecting ink in a loaded specimen. After the test, the specimen was split in half along planes that included the bar axes. By this process, it was possible to analyze the internal cracks existing in the concrete. Goto observed that when deformed bars were used lateral cracks or "primary cracks" were formed; and also around the deformed bars just after the formation of primary cracks there developed small internal cracks which do not appear at the concrete surface. When the steel stress became high, new lateral cracks called "secondary cracks" formed near the primary cracks. This caused the development of large hoop stresses in the concrete close to the bar, resulting in possible localized longitudinal cracks. Tepfers (6.39,6.40) analyzed the condition in which the splitting cracks spread across the whole concrete cover of the bar. He considered that the radial components of the bond forces are balanced against "concrete rings" in tension, which resist the tensile hoop stresses (Fig. 6.24).



The geometry of a deformed reinforcing bar and the mechanical interaction between the bar and the concrete. *Fig 23*



Schematic representation of how the radial components of the bond forces are balanced against tensile stress rings in the concrete in an anchorage zone. *Fig 24*



Fig 625
Failure Mode of the Pull-Out Specimen with Deformed Bar

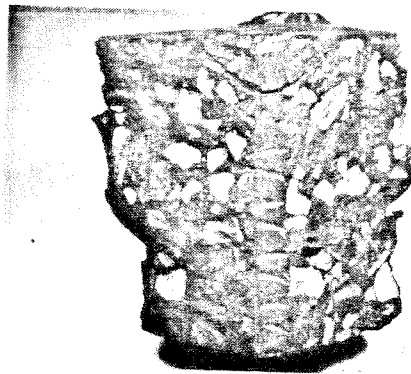


Fig 626
Detail of the Failure Mode

6.4.2 Test Program

The purpose of this investigation was to study the steel-concrete bond by performing pull-out tests. The variables of this investigation were the concrete compressive strength (four levels), the amount of silica fume (three levels), the type of reinforcing bar (plain and deformed) and the position of the bar. In all the 16 mixes, an ASTM Type I-II portland cement with the chemical analysis shown in Table 2.1, was used. The fine aggregate used was a Kaiser radum top sand with 2.68 bulk specific gravity, 0.9-percent absorption and 2.93 fineness modulus. The coarse aggregate was crushed limestone obtained from a local deposit with 2.69 bulk specific gravity, 0.5-percent absorption and 7.06 fineness modulus. The fine and coarse aggregate had a gradation as shown in Table 6.3.

The silica fume used was the same one used in Chapters 2 and 3, and in Sections 6.2 and 6.3. It consisted of 93-percent silica with a specific surface area of $20 - 25m^2/g$ and an average particle diameter of .1 micron.

Twenty-four in. long plain and deformed bars of A-36 steel were used with a minimum f_y of 60 ksi.

One of the purposes of this experiment was to study if the use of silica fume would improve the concrete-steel bond for a given concrete compressive strength. The concrete mixes were designed to produce a cohesive and workable concrete with 4-in. slump and compressive strength range of 3,000 to 12,000 psi. The mix designs are shown in Tables 6.4, 6.5, and 6.6.

Pure portland concrete mix with compressive strength of 3000 and 6000 psi were designed using the ACI method. Trial mixes were performed, and the necessary adjustments were made. The higher compressive strength level (9,000 and 12,000 psi) is not well covered by this method, and the final mix was obtained by extrapolating

TABLE 6.3
Sieve Analysis

Sieve Size	Sand % Retained	Coarse Aggregate % Retained
1"	0	1
3/4"	0	22
1/2"	0	75
3/8"	0	90
# 4	0	97
# 8	13	97
# 16	40	100
# 30	64	100
# 50	83	100
# 100	93	100
# 200	97	100

the tables given by Neville (8.41) and by trial and error.

The cement equivalence factor, K , was used for concrete with silica fume in order to obtain the desired compressive strength level. The value of K is variable, being lower when the amount of silica fume or cement is high. For concrete with 8-percent silica fume the value of K ranged from 4 for 3000-psi compressive strength to 2 for 12000-psi compressive strength. The concretes with 16-percent of silica fume had K varying from 2 to 1.

As the water to cement ratio decreased, the amount of fine aggregate also decreased because the silica fume and cement provided additional fines (Mark). A

TABLE 6.4
CONCRETE MIX DESIGN
0% SILICA FUME CONCRETE

MIX NUMBER	0-3000	0-6000	0-9000	0-12000
Cement (g/10l)	2523	3729	4514	6339
Water (g/10l)	1800	1720	1571	1656
Fine Aggregate (g/10l)	9898	7496	6766	4442
Coarse Aggregate (g/10l)	9906	11380	11611	11974
Plasticizer (ml/10l)	13	19	31	64
Unit Weight (g/10l)	24136	24344	24493	24493
W/C	0.717	0.464	0.3515	0.267
Slump (in)	3.5	3.75	3.75	4.0

lignosulfonate (Zeecon R40) with 1.2 specific gravity was used.

6.4.3 Test Procedure

The concrete mix was batched in a pan mixer with rotating blades. ASTM specifications were followed for mixing (ASTM C192), for the slump test (ASTM C143), for preparing the pull-out specimens (ASTM C234), and for the cylindrical specimens for compressive and splitting tests. Ten cylindrical specimens and four horizontal pull-out specimens were cast for each mix.

The specimens were kept in their molds for 24 hours and then they were stored in a 100% humidity room at 23° C. The tests were performed at the age of 28 days.

Testing the concrete compressive strength for the range 9,000 to 12,000 psi presented problems with the sulphur cap that under high loads would have a plastic

TABLE 6.5
CONCRETE MIX DESIGN
8% SILICA FUME CONCRETE

MIX NUMBER	8-3000	8-6000	8-9000	8-12000
Cement (g/10l)	2004	2984	3858	5481
Silica Fume (g/10l)	160	239	309	438
Water (g/10l)	1760	1688	1569	1598
Fine Aggregate (g/10l)	8930	6915	6484	4580
Coarse Aggregate (g/10l)	10915	12294	12040	12322
Plasticizer (ml/10l)	14	32	54	99
Unit Weight (g/10l)	23785	24152	24315	24518
W/(C+S)	0.817	0.530	0.377	0.279
Slump (in)	3.5	4.0	4.25	4.0

flow causing a premature failure of concrete. To avoid this problem, the specimens were polished with a grinding machine until the concrete surfaces met the ASTM specifications. This was a laborious and time-consuming operation; however it paid off because a higher compressive strength was obtained than when sulphur cap was used, and the dispersion of the results was reduced.

6.4.4 Test Results and Analysis

The compressive strength results for the mixes are given in Table 6.7. It should be noted that the pull-out specimens were made with limestone concrete. The results for the quartz concrete are given for completeness (see Chapter 5). As can be seen, the compressive strength results for the limestone concrete were close to the target

TABLE 6.6
CONCRETE MIX DESIGN
16% SILICA FUME CONCRETE

MIX NUMBER	16-3000	16-6000	16-9000	16-12000
Cement (g/10l)	1678	2489	3383	4792
Silica Fume (g/10l)	269	398	541	766
Water (g/10l)	1757	1676	1590	1639
Fine Aggregate (g/10l)	8606	6805	5989	4631
Coarse Aggregate (g/10l)	11409	12636	12725	12519
Plasticizer (ml/10l)	29	43	76	113
Unit Weight (g/10l)	23750	24048	24304	24460
W/(C+S)	0.911	0.588	0.415	0.306
Slump (in)	3.5	4.25	3.75	3.75

strength levels, with the exception of the concrete mix with no silica fume that failed to get the aimed strength of 12,000 psi.

The tensile-to-compressive strength ratio was approximately 0.14 for the lower strength of the limestone concrete (for all the three levels of silica fume), and it was reduced to 0.08 for the higher strength concrete. This decrease is typical, and the interesting point is that the ratio was not very dependent on the level of silica fume for a given compressive strength level.

Fig. 6.25 shows the failure mode of a pull-out specimen using a deformed bar. As can be seen, the concrete failed by splitting in two orthogonal planes as discussed in Section 6.4.1. Fig. 6.26 shows a detail of the concrete, in which the imprint of the reinforcing bar can be seen.

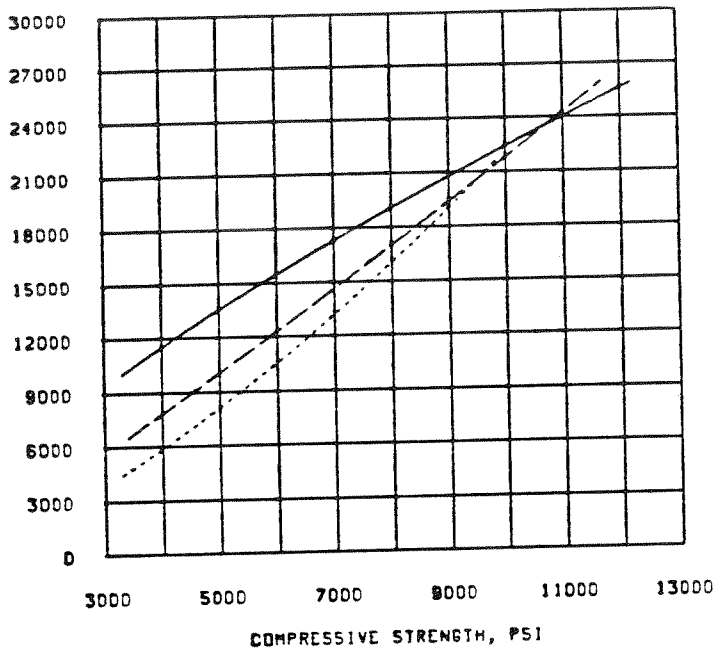
The results show the major influence of the bar position on the bond strength, the "upper" bars showing in most cases a lower strength because they had much higher concrete bleeding which resulted in the accumulation of water and air beneath the lugs with consequent loss of bond strength. For plain bars, as the concrete strength increases the difference of the two bars tends to decrease because the higher amount of cementitious material that is used tends to diminish the concrete bleeding, thus producing a more uniform material.

The results of the pull-out tests are summarized in Tables 6.8, 6.9, 6.10.

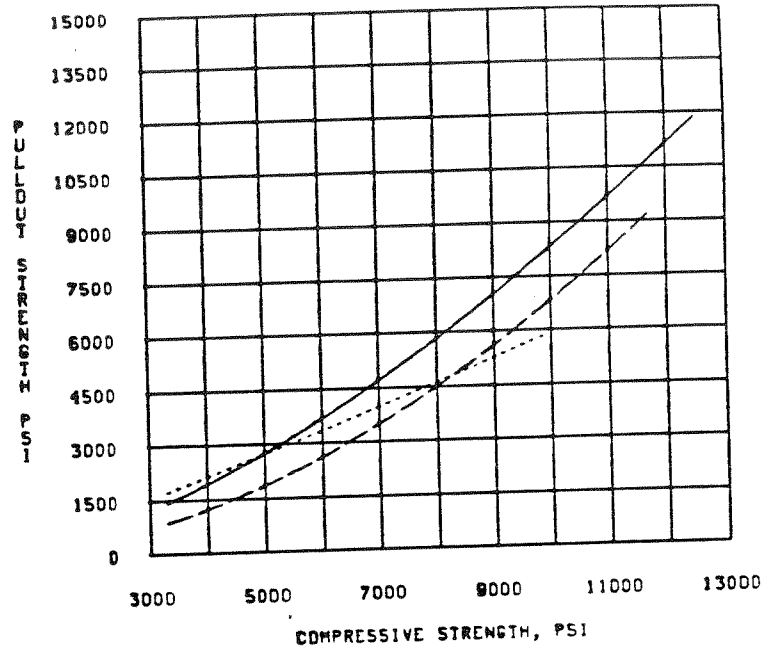
Fig. 6.27 shows the graph of the pull-out strength versus the concrete compressive strength for each bar. The results were fitted with the expression $f_{\text{pull-out}} = K_1 f_c^{K_2}$, where $f_{\text{pull-out}}$ is the pull-out strength, f_c the concrete compressive strength, and K_1 K_2 are constants. The results for plain bar with the concrete mix 0-6000 were not included in the regression because they were not reliable. As can be seen and has been reported before, the concrete compressive strength plays a major role in the pull-out strength. The level of silica fume also has an effect on the pull-out strength, especially in the high compressive strength range of the concrete.

At first glance, these results showing the effect of silica fume on the improvement of the steel-concrete bond seem to be a perfect consequence of the improvement of the steel-cement paste interface, as discussed in Section 6.3. The interface morphology has a major influence on the mechanism of debonding and slip for plain bars. However, we must be cautious and not make general conclusions; first of all some of the characteristics of the interface discussed in Section 6.3 are related to the chemical adhesion, which is mostly gone before failure occurs (especially with deformed bars).

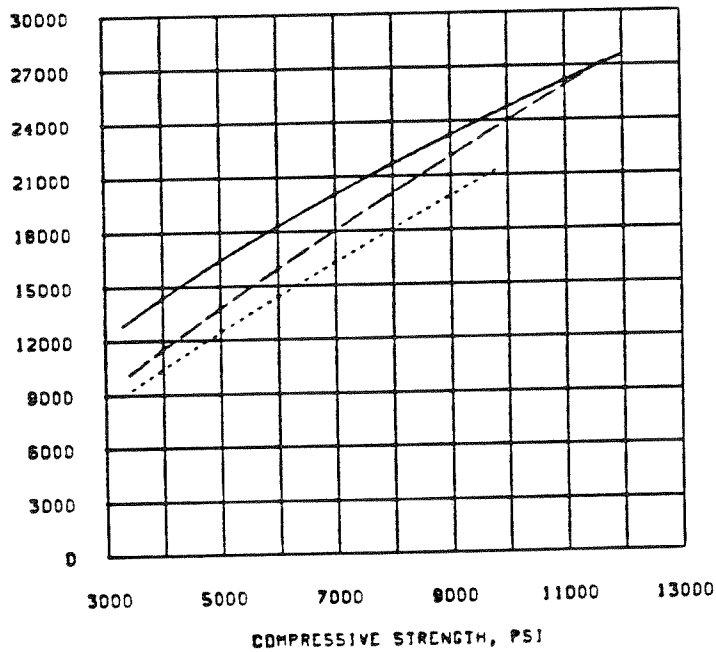
DEFORMED BARS/UPPER POSITION



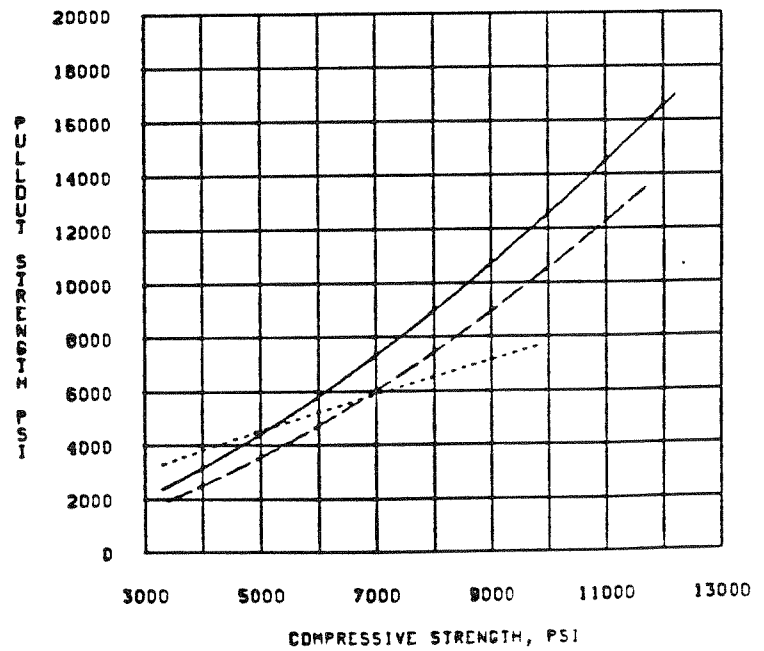
PLAIN BARS/UPPER POSITION



DEFORMED BARS/LOWER POSITION



PLAIN BARS/LOWER POSITION



..... 0% silica fume
 - - - - 8% silica fume
 ———— 16% silica fume

Fig 6.27
 Pull-Out Strength Versus the
 Concrete Compressive Strength

..... 0% silica fume
 - - - - 8% silica fume
 ———— 16% silica fume

TABLE 6.7
CONCRETE STRENGTH (PSI)

MIX #	QUARTZ AGGREGATE		LIMESTONE AGGREGATE	
	Compressive	Tensile	Compressive	Tensile
0-3000	3166	449	3302	446
0-6000	6263	681	5564	673
0-9000	7955	788	8035	713
0-12000	8298	940	9828	860
8-3000	3258	468	3447	508
8-6000	6592	715	5784	707
8-9000	8557	845	9398	837
8-12000	9411	1009	11692	896
16-3000	2988	427	3328	472
16-6000	5128	626	5349	629
16-9000	8787	799	9759	778
16-12000	9714	970	12163	912

The reason why the silica fume increases the pull-out strength for a given compressive strength is that it produces a more uniform material, decreasing the

TABLE 6.8
PULL-OUT STRENGTH (PSI)
0% SILICA FUME CONCRETE

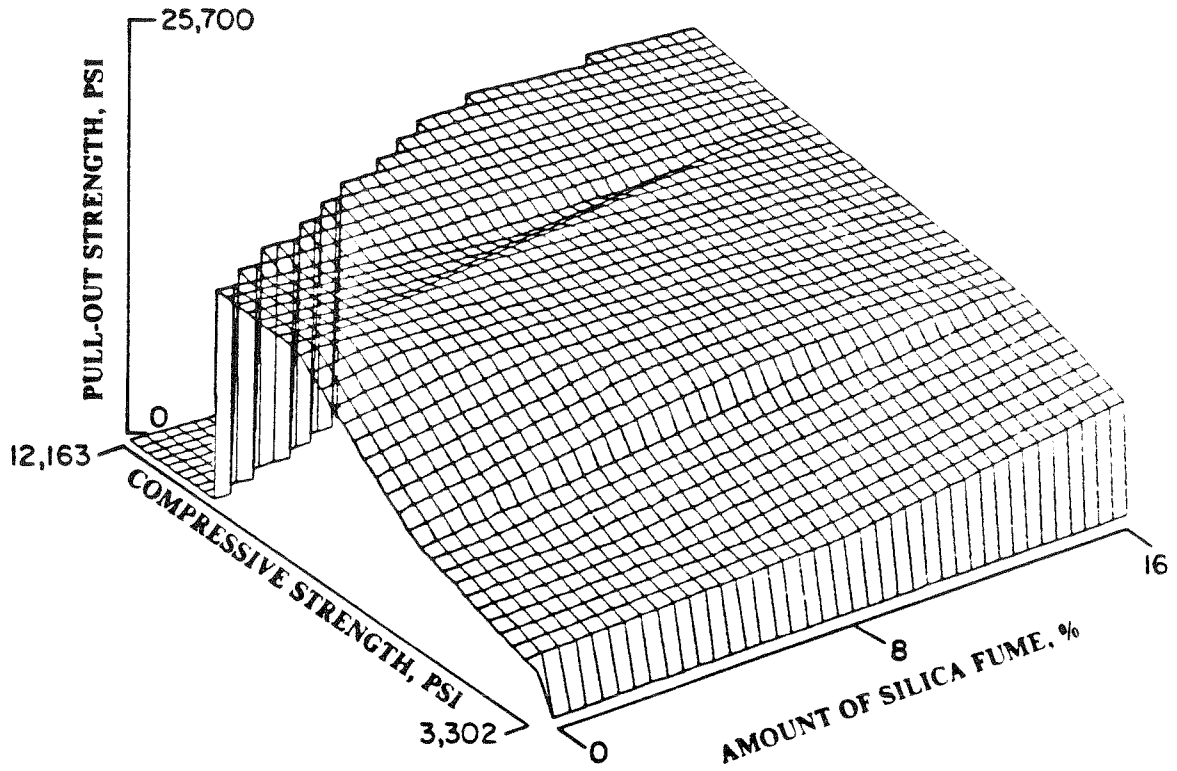
MIX #	Criteria*	Plain Bar		Deformed Bar	
		Upper	Lower	Upper	Lower
0-3000	0.01	—	—	4500	9600
	Max	1690	3360	18630	18260
0-6000	0.01	—	—	8650	12250
	Max	1000	1535	17640	24200
0-9000	0.01	4950	5750	18900	16300
	Max	4950	5850	20500	19100
0-12000	0.01	5520	8500	19800	24400
	Max	7600	14600	28000	25200

general porosity and producing a densifying of the interfaces (steel-concrete and aggregate-matrix) resulting in a better material to resist the splitting forces for deformed bars.

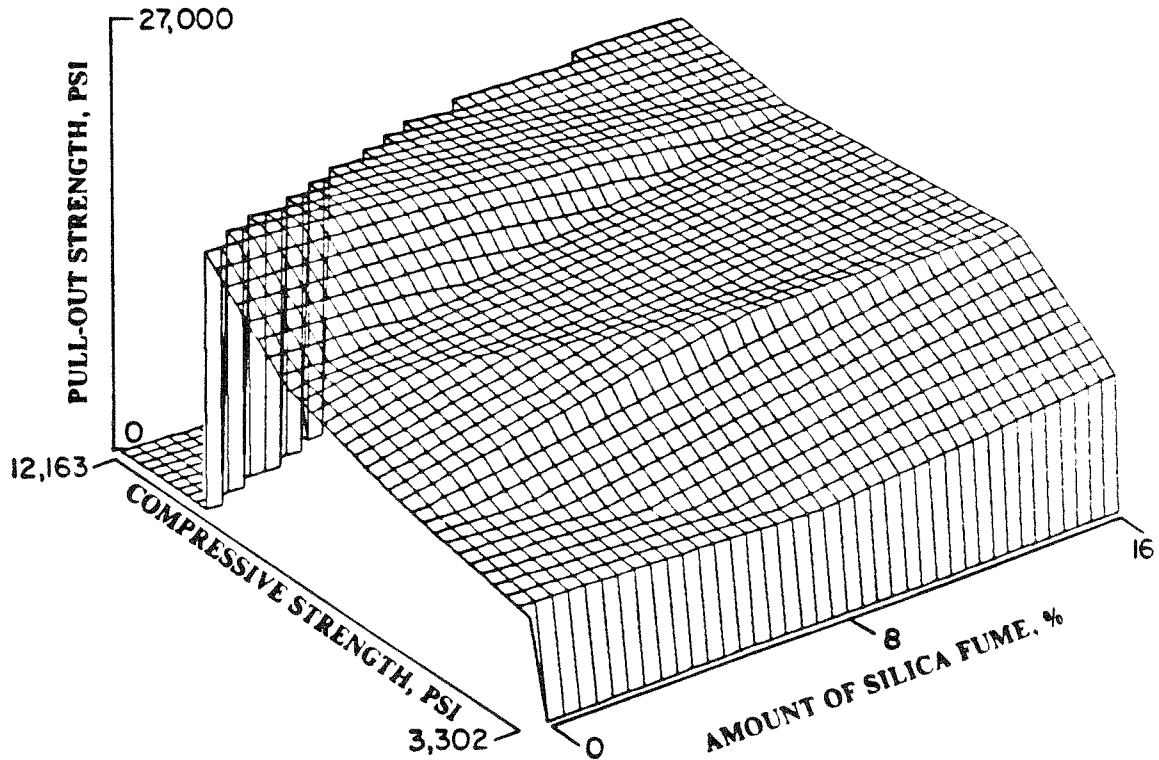
Figs. 6.27A and B show isometric projections for the pull-out strength as a function of the compressive strength of concrete and the amount of silica fume. The projections were obtained from interpolation of the results and not from a mathematical expression. It can be seen that the surface increases as the compressive strength or the amount of silica fume increases.

The dependence of the pull-out strength on the tensile and compressive strength of concrete is shown in the isometric projections of Figs. 6.29A and B.

DEFORMED BARS/Upper Position

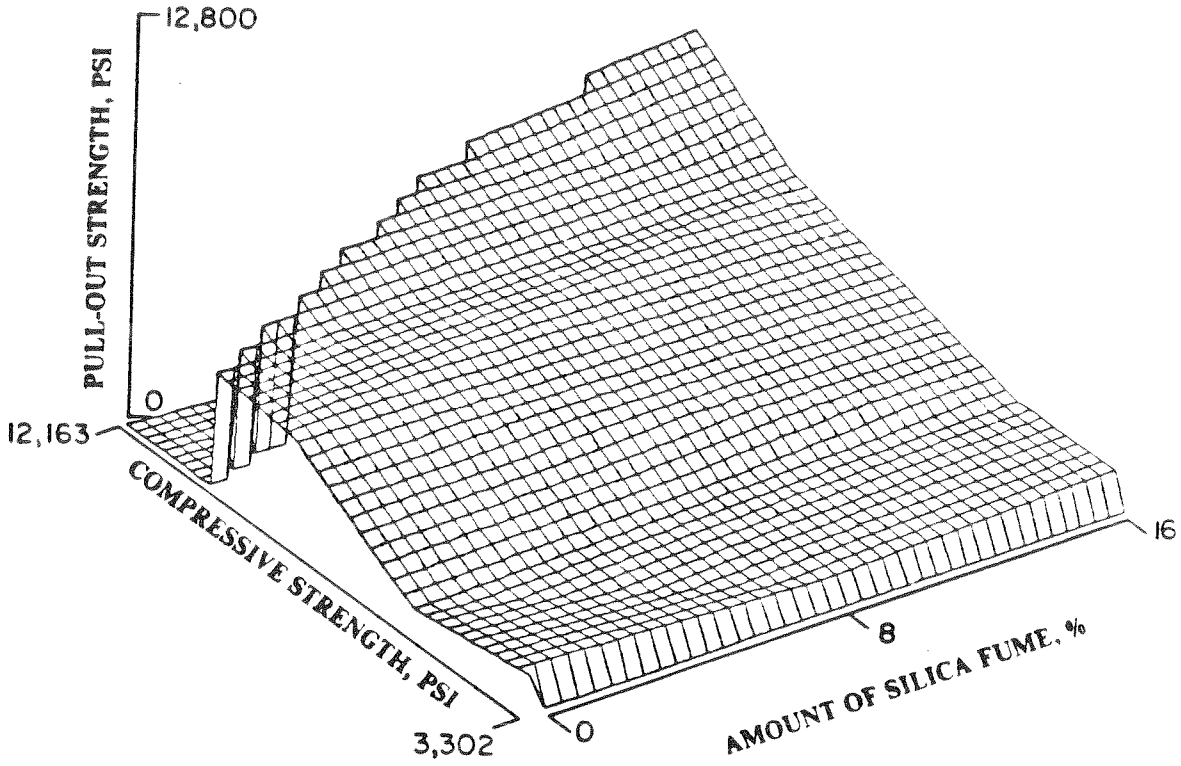


DEFORMED BARS/Lower Position

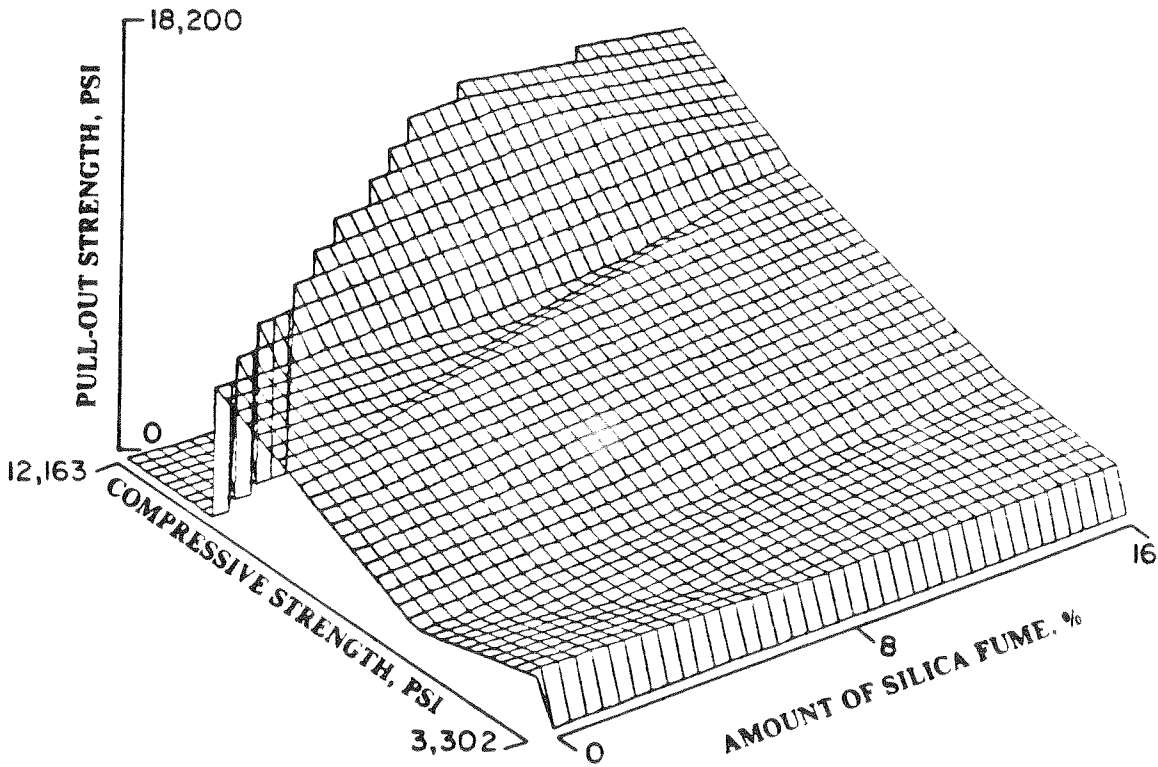


Pull-Out Strength in function of the concrete compressive strength and the amount of silica fume *Fig 28A*

PLAIN BARS/Upper Position

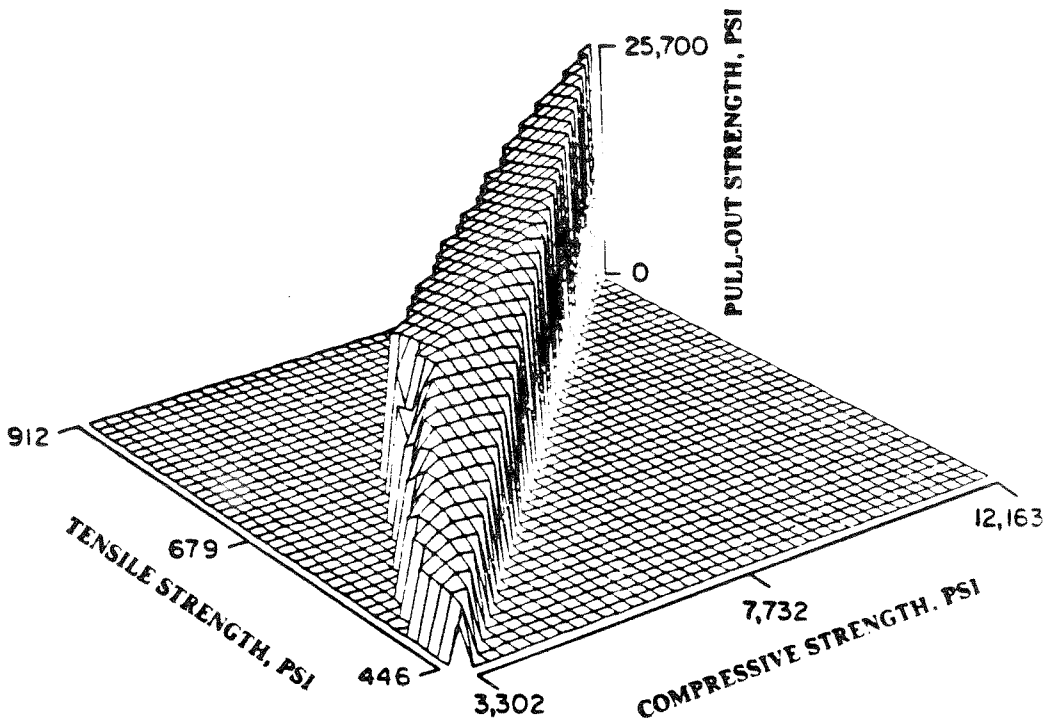


PLAIN BARS/Lower Position



Pull-Out Strength in function of the concrete compressive strength and the Amount of Silica Fume. Fig: 28B

DEFORMED BARS/Upper Position



DEFORMED BARS/Lower Position

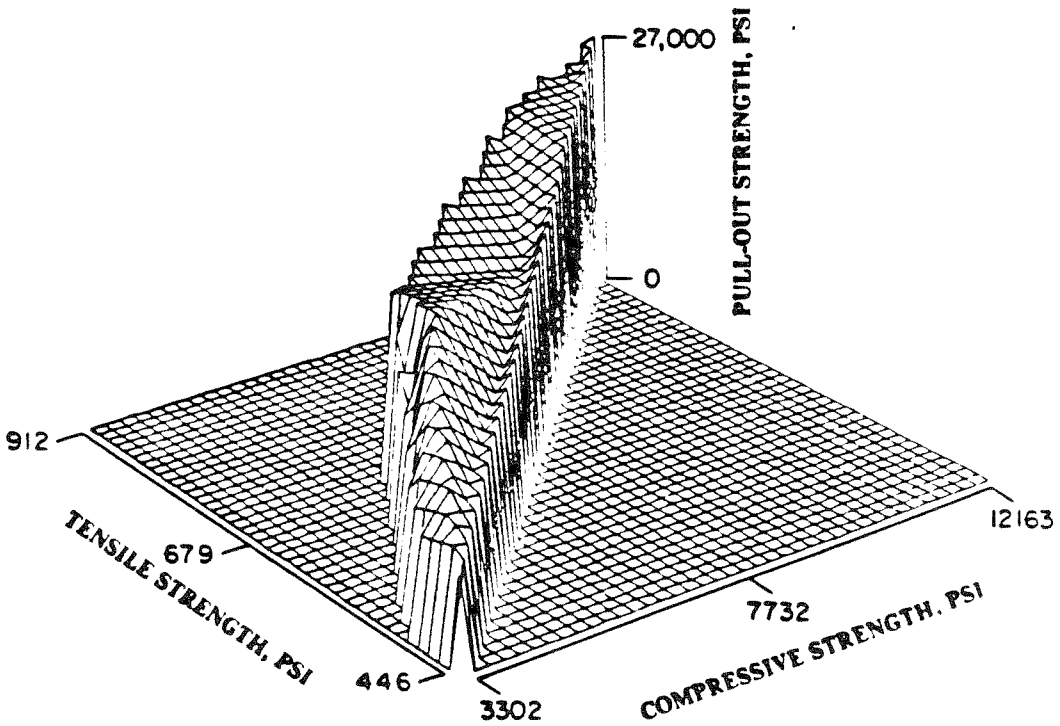
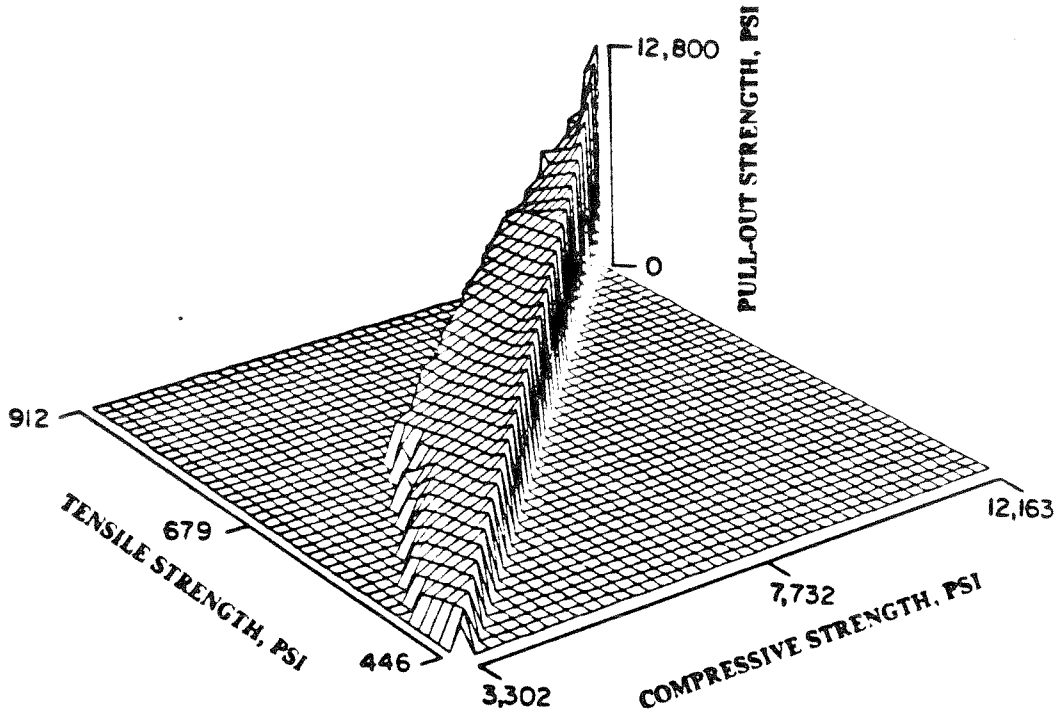
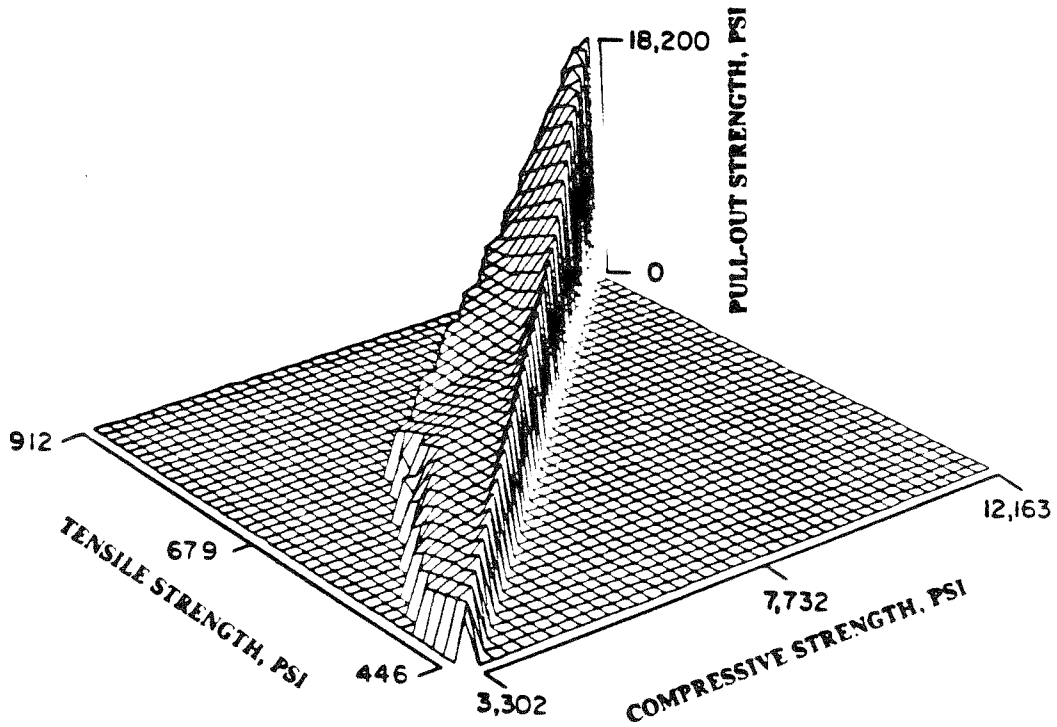


Fig. 79 A
Pull-Out Strength in Function of the Tensile and Compressive Strength of Concrete.

PLAIN BARS/Upper Position



PLAIN BARS/Lower Position



061 Pull-Out Strength in ^{Fig 29B} Extraction of the Tensile and Compressive Strength of Concrete.

TABLE 6.9
PULL-OUT STRENGTH (PSI)
8% SILICA FUME CONCRETE

MIX #	Criteria*	Plain Bar		Deformed Bar	
		Upper	Lower	Upper	Lower
8-3000	0.01	—	—	5880	9000
	Max	1000	2530	13680	15200
8-6000	0.01	—	—	14700	19200
	Max	2060	3050	18200	22300
8-9000	0.01	6430	8070	19000	22800
	Max	10350	9400	24300	25700
8-12000	0.01	9400	18200	25000	24843
	Max	10400	19000	33500	33000

6.5 References

- 6.1 Lutz L.A. and Gergely P., 'Mechanics of Bond and Slip of Deformed Bars in Concrete'. *Journal of the American Concrete Institute*, 64, 711, 1967.
- 6.2 Vos E. and Reinhardt H.W., 'Bond Stress-Slip Behavior of Deformed Bars, Plain Bars and Strands under Impact Loadings'. *Bond in Concrete*. Ed. P. Bartos, Applied Science Publishers, London, 1982.
- 6.3 Abrams D.A., 'Tests of Bond Between Concrete and Steel'. Bulletin 71, Engineering Experimental Station, University of Illinois, 1973.
- 6.4 Menzel, C.A., 'Some Factors Influencing Results of Pull-Out Bond Tests'. *Journal of the American Concrete Institute*, 43, No. 4, 1946.

TABLE 6.10
PULL-OUT STRENGTH (PSI)
16% SILICA FUME CONCRETE

MIX #	Criteria*	Plain Bar		Deformed Bar	
		Upper	Lower	Upper	Lower
16-3000	0.01	—	2540	9750	11400
	Max	1650	4200	14400	15850
16-6000	0.01	—	4430	15000	21000
	Max	2470	6110	17050	25500
16-9000	0.01	7600	11800	21615	23000
	Max	10680	12250	27700	29000
16-12000	0.01	12800	17825	25700	27000
	Max	17630	18200	30700	32500

- 6.5 Clark, A.P., 'Bond of Concrete Reinforcing Bars'. Journal of the American Concrete Institute, 46, No. 3, 1949.
- 6.6 Clark A.P., 'Comparative Bond Efficiency of Deformed Concrete Reinforcement Bars'. Journal of the American Concrete Institute, 43, No. 4, 1946.
- 6.7 Collier S.T., 'Bond Characteristics of Commercial and Prepared Reinforcing Bars'. Journal of the American Concrete Institute, 43, 1947.
- 6.8 Jirsa J.O., Breen J.E., Luke J.J. and Hammad, 'Effect of Casting Position on Bond'. *Bond in Concrete*. Ed. P. Bartos, Applied Science Publishers, London, 1982.

- 6.9 Mains R.M., 'Measurement of the Distribution of Tensile and Bond Stresses along Reinforcing Bars'. Journal of the American Concrete Institute, 48, 335, 1951.
- 6.10 Bresler B. and Bertero V.V., 'Behavior of Reinforced Concrete Under Repeated Load'. Trans. ASCE, J. Struct. Div., 94, 1567, June 1968.
- 6.11 Broms B. B., 'Stress Distribution in Reinforced Concrete Members with Tension Cracks'. Journal of the American Concrete Institute, 62, NO. 9, 1095, 1965.
- 6.12 Ngo D. and Scordelis A.C., 'Finite Element Analysis of Reinforced Concrete Beams'. Journal of the American Concrete Institute, 64, 711, 1967.
- 6.13 Cedolin L. and Bazant Z.P., 'Fracture Mechanics of Crack Bands in Concrete', *Fracture Mechanics Methods for Ceramics, Rocks, and Concrete*. ASTM STP 745, S.W. Freiman and E.R. Fuller, Eds., American Society for Testing and Materials, 221, 1981.
- 6.14 Chen W.F., *Plasticity in Reinforced Concrete*. McGraw-Hill Book Co. Inc. New York, NY., 1982.
- 6.15 Velasco F., Visalvanich K. and Shah S.P., 'Fracture Behavior and Analysis of Fibre Reinforced Concrete Beams'. Cement and Concrete Research, 10, 41, 1980.
- 6.16 Vesalvanich K. and Naaman A.E., 'Evaluation of Fracture Techniques in Cementitious Composites', Journal of the Engineering Mechanics Division, ASCE, 107, 1155, 1981.
- 6.17 Sek C., Baron J. and Francois D., 'M echanique de la Rupture Appliquee au Beton Hydraulic'. Cement and Concrete Research, 9, 641, 1979.
- 6.18 Wecharatana M. and Shah S.P., 'Resistance to Crack Growth in Portland Cement Composites'. *Fracture in Concrete*. edited by W.F. Chen and E.C. Ting, American Society of Civil Engineers, New York, 82, 1980.

- 6.19 Hillerborg A., Modees M. and Petersson P.E., 'A nalysis of Crack Formation and Crack Growth in Concrete by Means of Fracture Mechanics and Finite Elements'. Cement and Concrete Research, 6, 773, 1976.
- 6.20 Hillerborg A. 'A nalysis of Fracture by Means of the Fictitious Crack Model, Particularly for Fibre Reinforced Concrete'. International Journal of Cement Composites, 2, 177, 1980.
- 6.21 Petersson P.E., 'Crack Growth and Development of Fracture Zones in Plain Concrete and Similar M aterials', Ph.D. Thesis, Lund Institute of Technology, Sweden, 1981.
- 6.22 Bazant Z.P. and Cedolin L., 'Fracture Mechanics of Reinforced Concrete'. Journal of the Engineering M echanics Division, Proceedings, American Society of Concrete Engineers, 106, No. EM 6, paper 15917, 1287, 1980.
- 6.23 Cedolin L. and Bazant Z.P., 'Effect of Finite Element Choice in Blunt Crack Band A nalysis'. Computer Methods in A pplied M echanics and Engineering, 24, 305, 1980.
- 6.24 Bazant Z.P. in Journal of Engineering M echanics Division; Proceedings, A merican Society of Concrete Engineers, 102, No. EM 2, Proceedings, Paper 12042, , 331, 1976
- 6.25 Al Khalaf M.N., Page C.L., 'Steel/M ortar Interfaces: Microstructural Features and Mode of Failure'. Cement and Concrete Research, 9, 197, 1979.
- 6.27 Sakamoto N. and Iwasaki N., 'Influence of Sodium Chloride on the Concrete-Steel and Galvanized Steel Bond'. *Bond in Concrete*. Ed. P. Bartos, Applied Science Publishers, London, 1982.
- 6.28 Coleman D., Holland P., Kaden N., Klena V. and Peters S.C., 'A System Of Subroutines for Iteratively Reweighted Least Squares Computations'. ACM Transactions on M athematical Sofware, 6, No. 3, 327, 1980.

- 6.29 Barrodale I. and Roberts F.D.K., 'Solution of an Overdetermined System of Equations in the l_1 Norm'. Communications of the ACM, 17, No. 6, 1974.
- 6.30 Kurdowski W. and Nocun-W czelik, 'The Tricalcium Silicate Hydration in the Presence of Active Silica'. Cement and Concrete Research, 13, 341, 1983.
- 6.31 Slater J.E., 'Corrosion of Metals in Association with Concrete'. ASTM STP 818, 1983.
- 6.32 Nicol A., 'Behavior of Iron in Contact with Cement'. Revue Matér. Constr. Trav. publ. 537/9, 149 and 190, 1960.
- 6.33 Moreau M., 'Contribution a l'étude d'adhérence entre les Constituants Hydratés du ciment Portland Artificiel et l'Armature Enrobée'. Revue Matér. Constr. Trav. 678, 4 1973.
- 6.34 Page C.L., 'Mechanism of Corrosion Protection in Reinforced Concrete Marine Structures'. Nature, 258, 514, 1975.
- 6.35 Gjorv O.E., Monteiro P.J.M. and Mehta P.K., 'Effect of Microsilica on the Steel-Concrete Bond'. Department of Civil Engineering, SESM Division, University of California, Berkeley, 1985.
- 6.36 Page C.L. and Vennesland O., 'Pore Solution Composition and Chloride Binding Capacity of Silica Fume-Cement Pastes'. SINTEF STF A 82025, The Norwegian Institute of Technology, NTH, Trondheim, 1982.
- 6.37 Goto Y., 'Cracks Formed in Concrete around Deformed Tension Bars'. Journal of the American Concrete Institute, Proceedings, 68, No. 4, 244, 1971.
- 6.38 Goto Y. and Otsuka K., 'Experimental Studies on Cracks Formed in Concrete Around Deformed Tension Bars'. The Technology Reports of the Tohoku University, 44, No. 1, 49, 1979.
- 6.39 Tepfers R., 'Cracking of Concrete Cover Along Anchored Deformed Bars'. Magazine of Concrete Research, 31, No. 106, 3, 1977.

- 6.40 Tefpers R., 'Tensile Lap Splices with Confining Reinforcement'. *Bond in Concrete*. Ed. P. Bartos, Applied Science Publishers, London, 1982.
- 6.41 Neville A M., *Properties of Concrete*. Pitman, London, 1977.
- 6.42 Gambarova P. and Karakoc C. 'Shear-Confinement Interaction at the Bar-to-Concrete Interface'. *Bond in Concrete*. Ed. P. Bartos, Applied Science Publishers, London, 1982.